

# **Instability of two-phase co-axial jets at small Reynolds number**

THÈSE N° 6730 (2015)

PRÉSENTÉE LE 11 SEPTEMBRE 2015

À LA FACULTÉ DES SCIENCES ET TECHNIQUES DE L'INGÉNIEUR  
LABORATOIRE DE MÉCANIQUE DES FLUIDES ET INSTABILITÉS  
PROGRAMME DOCTORAL EN MÉCANIQUE

ÉCOLE POLYTECHNIQUE FÉDÉRALE DE LAUSANNE

POUR L'OBTENTION DU GRADE DE DOCTEUR ÈS SCIENCES

PAR

**Laura AUGELLO**

acceptée sur proposition du jury:

Prof. C. Ancey, président du jury  
Prof. F. Gallaire, directeur de thèse  
Prof. A. Colin, rapporteuse  
Dr B. Scheid, rapporteur  
Dr M. Farhat, rapporteur



ÉCOLE POLYTECHNIQUE  
FÉDÉRALE DE LAUSANNE

Suisse  
2015



# Acknowledgements

I would like to express my gratitude to all the people who have contributed to the realization of this project. François thank you for your availability and for guiding me in my work during these four years. Thank you especially for having supported me in the most difficult moments, encouraging me to go forward. I am grateful that I was part of the LFMI lab, an excellent group, with whom I shared both happy and funny moments but also stressed days. I would like to thank everyone in the LFMI team: my long-time office mate Vlado with whom I began this adventure, Andrea for his patience and availability, Francesco, Giacomo, Gioele, Edouard, Mathias, P.T., Yoan, Lailai, Nicolas and Isha for their friendship that made me feel like at home during these years, Petra without whom we will be lost. Special thanks goes to Cristobal so far and yet so close.

I am grateful to Mohamed Farhat, Annie Colin and Benoît Scheid for taking the time to read this manuscript and to attend the defense, and to Christophe Ancey for presiding over the jury.

Due acknowledgement also goes to the Swiss National Science Foundation which has funded and supported this project (grant no. 200021-132323 and 200020-152957 "*Instabilités de jets et sillages coaxiaux diphasiques*").

Un ringraziamento speciale va ai miei genitori, a mia cugina Alessandra che è stata con me nell'ultima settimana di scrittura di questa tesi, a Enrica, Elisa e Silvia tre persone differenti ma ugualmente uniche ed a Andrea per le risate, il supporto e i disegni.



Lausanne, 11 September 2015





# Abstract

A precise knowledge of co-axial flow dynamics and a better understanding of the mechanisms that act to destabilize the interface between the two fluids is of fundamental interest in many industrial applications like lubricated transport, injection devices, atomization and controlled microdroplet production. The flow is in general unstable, since at least two mechanisms act to destabilize the cylindrical interface: shear and capillary instabilities. While these two mechanisms are active in a jet issuing from a tap, their respective influence strongly depends on the Reynolds number, the Ohnesorge number, but also on the viscosity, density, and aspect ratios.

In this thesis, the global stability characteristics of two-phase co-axial flow are determined. The stability analysis follows two successive steps. First the steady base flow is determined, via the resolution of the nonlinear Navier-Stokes equations together with the location of the free interface. Second, these equations are linearized around the base flow and the dominant eigenmodes determined. The novelty lies in the formulation of models that can describe both the qualitative and quantitative characteristics of the two-phase flow configuration and the adaptation of the tools of global stability analysis for this configuration. We find that the dripping to jetting regime transition depends on the Capillary number, the degree of the confinement and the viscosity ratio, and we show that, surprisingly, the nozzle geometry does not affect the stability properties of the flow with subtle effects.

Finally, the influence of surface viscosity on these coaxial flows has been considered. The governing and constitutive equations describing the continuum mechanics of the surface in the axisymmetric case are derived. With the addition of surface viscosity at the interface, the base flow evolves over a lengthscale which is much larger than the entry length in the Stokes regimes and than the typical unstable wavelength. We show that while the flow becomes eventually more convectively unstable once it reaches the fully developed profile, the surface viscosity creates an absolute region at the inlet, that is expected to promote droplet formation.

**Key words:** co-axial flow, free interface, instabilities, drop formation, surface viscosity



# Résumé

Une description détaillée de la dynamique des écoulements coaxiaux ainsi qu'une meilleure compréhension des mécanismes qui déstabilisent l'interface cylindrique entre les deux fluides sont d'un grand intérêt dans de nombreuses applications industrielles telles que les systèmes d'injection, de transport lubrifié, d'atomisation ou encore pour la production contrôlée de micro-gouttes. L'écoulement est généralement instable en raison d'au moins deux mécanismes qui déstabilisent l'interface cylindrique : la contrainte de cisaillement et l'instabilité capillaire. Bien que les deux contraintes soient présentes dans tout jet, leur influence dépend considérablement des caractéristiques physiques des fluides telles que la viscosité, la densité, la tension de surface à travers du nombre de Reynolds, du nombre de Ohnesorge ainsi que du confinement géométrique et

Dans cette thèse, les caractéristiques de stabilité globale pour les écoulements coaxiaux à diphasiques sont investigués. L'analyse est développée en deux parties distinctes. En premier lieu, l'écoulement de base est déterminé par la résolution des équations non-linéaires de Navier-Stokes et l'interface entre les deux fluides est calculée. Ensuite, ces équations sont linéarisées autour de l'écoulement de base et les modes propres dominants sont déterminés. La nouveauté du travail présenté se situe dans la formulation de modèles capable de décrire lu même temps les caractéristiques qualitatives et quantitatives de la configuration des écoulements diphasiques. Les outils d'analyse de stabilité ont par conséquent du être adaptés à la nouvelle description du phénomène. L'application des modèles proposés a permis de mieux comprendre la dynamique en jeu. L'étude de la transition entre le régime de gouttes et celui de jet a montré que le processus est dominé par les propriétés intrinsèques des écoulements développés, mais a révélé des effets subtils. Finalement, l'influence des surfactants sur les écoulements coaxiaux a aussi été investiguée. La résistance mécanique à l'interface des deux fluides s'avère être de grande importance et la contrainte de cisaillement ne peut plus être négligée lors de la définition des conditions à l'interface. Dans cette thèse, une première évaluation quantitative des effets des surfactants sur la stabilité de l'écoulement est proposée. Il en ressort qu'une plus haute viscosité de surface stabilise l'écoulement développé, mais perturbe le jet dans la région d'injection.

**Mots clefs :** écoulements coaxiaux, interface, instabilité, formation de gouttes, viscosité de surface



# Riassunto

Una conoscenza precisa della dinamica dei flussi coassiali e una migliore comprensione dei meccanismi che agiscono per destabilizzare l'interfaccia tra due fluidi è di fondamentale interesse in molte applicazioni industriali come il trasporto lubrificato, dispositivi di iniezione, atomizzazione e la produzione controllata di micro gocce. Il flusso coassiale è generalmente instabile, poiché almeno due meccanismi agiscono per destabilizzare l'interfaccia: lo sforzo tangenziale e l'instabilità capillare. Mentre questi due meccanismi sono attivi in un getto emesso da un rubinetto, la rispettiva influenza dipende fortemente dal numero di Reynolds, dal numero di Ohnesorge, ma anche dai rapporti di viscosità, densità, e confinamento.

In questa tesi, le caratteristiche globali di stabilità di un flusso bifase coassiale sono determinate. L'analisi di stabilità è eseguita in due fasi. In primo luogo il flusso stazionario viene determinato mediante la risoluzione delle equazioni di Navier-Stokes, ottenendo la posizione dell'interfaccia. Successivamente, le equazioni costitutive vengono linearizzate intorno alla soluzione stazionaria e le autofunzioni vengono determinate. La novità consiste nella formulazione di modelli che possano descrivere sia qualitativamente che quantitativamente le caratteristiche del flusso stazionario e di quello perturbato. Studiando la stabilità globale di un getto bifase, scopriamo che la transizione da un getto continuo a un getto che si rompe in gocce dipende dal numero di capillarità, dal rapporto di viscosità tra le due fasi e dal grado di confinamento. Vedremo che, sorprendentemente, la geometria dell'iniettore non influenza la stabilità del flusso.

Infine, l'influenza della viscosità dell'interfaccia dei flussi coassiali è stata analizzata. Le equazioni di governo e quelle costitutive che descrivono la meccanica dei continui dell'interfaccia sono derivate. Con l'aggiunta di viscosità di interfaccia, il flusso stazionario evolve in una lunghezza d'onda che è molto maggiore rispetto alla lunghezza caratteristica dei flussi di Stokes e rispetto alla lunghezza d'onda tipica dell'instabilità. Mostriamo che mentre il sistema diventa più convettivamente instabile una volta raggiunto il profilo completamente sviluppato, la viscosità di superficie crea una regione di instabilità assoluta all'ingresso del tubo, che promuove la formazione di gocce.

**Parole chiave:** flussi coassiali, interfaccia, instabilità, formazione di gocce, viscosità di superficie



# Contents

<b>Abstract (English/Français/Italiano)</b>	<b>iii</b>
<b>Introduction</b>	<b>1</b>
<b>1 Liquid threads and jets</b>	<b>11</b>
1.1 Hydrodynamic description of jets . . . . .	11
1.2 Long-wavelength description . . . . .	13
1.3 Stability analysis . . . . .	15
1.4 Liquid thread . . . . .	16
1.4.1 Inviscid thread . . . . .	17
1.4.2 Viscous thread . . . . .	17
1.4.3 Viscous thread with inertia . . . . .	19
1.5 Liquid jets . . . . .	21
1.5.1 Inviscid jet . . . . .	24
1.5.2 Viscous jet . . . . .	25
1.5.3 Viscous jet with inertia . . . . .	26
1.6 Relationship between absolute/ convective and global stability . . . . .	28
1.6.1 System description and local stability analysis . . . . .	29
1.6.2 Global stability analysis . . . . .	30
<b>2 Threads and jets in a surrounding flow</b>	<b>33</b>
2.1 Hydrodynamic description of jets and surrounding flow . . . . .	33
2.2 Threads in a quiescent external medium . . . . .	34
2.2.1 Inviscid thread immersed in a quiescent inviscid medium . . . . .	34
2.2.2 Inviscid thread immersed in a quiescent viscous medium . . . . .	36
2.2.3 Viscous thread immersed in a quiescent viscous medium . . . . .	38
2.2.4 Viscous thread with inertia in a quiescent viscous medium . . . . .	40
2.3 Jet in a medium . . . . .	41
2.4 Co-axial parallel jets in circular capillaries . . . . .	44
2.4.1 Base flow . . . . .	44
2.4.2 Stability analysis . . . . .	45
2.4.3 Temporal stability analysis and dispersion relation . . . . .	49
2.4.4 Spatio-temporal stability analysis and convective/absolute regime . . . . .	49

## Contents

---

2.4.5	Exact dispersion relation . . . . .	51
<b>3</b>	<b>Global stability analysis of co-axial jets</b>	<b>55</b>
3.1	Introduction . . . . .	56
3.2	Problem description . . . . .	58
3.2.1	Steady solution . . . . .	58
3.2.2	Global stability analysis . . . . .	60
3.3	Validation: stability of a parallel flow . . . . .	64
3.4	Base flow of co-axial streams . . . . .	66
3.5	Stability of the spatially developing flow . . . . .	66
3.6	Conclusion . . . . .	76
3.7	Appendix 1: Sponge region at the outlet of the computational domain . .	76
3.8	Appendix 2: Toy model for the global stability analysis of coaxial jets . .	77
<b>4</b>	<b>Complex fluid-fluid interface: surface viscosity</b>	<b>79</b>
4.1	Dynamic description of a two-phase flow interface . . . . .	81
4.1.1	Governing equation . . . . .	81
4.1.2	Derivation of the constitutive equation . . . . .	82
4.2	Stability of a viscous thread immersed in an inert medium . . . . .	86
4.3	Stability of a two-phase co-axial jet . . . . .	90
4.3.1	Introduction . . . . .	91
4.3.2	Governing equations and boundary conditions . . . . .	93
4.3.3	Base flow . . . . .	95
4.3.4	Stability analysis . . . . .	98
4.3.4.1	Linearized lubrication analysis . . . . .	98
4.3.4.2	Dispersion relation . . . . .	100
4.3.5	Effect of surface rheology on the temporal and spatio-temporal stability of the fully developed flow . . . . .	101
4.3.5.1	Temporal stability . . . . .	101
4.3.5.2	Spatio-temporal stability . . . . .	104
4.3.6	Effect of surface viscosity on the stability of the overall flow . . . .	107
4.3.7	Discussion and conclusion . . . . .	110
4.3.8	Appendix 1: Normal mode expansion . . . . .	111
4.3.9	Appendix 2: Dispersion relation . . . . .	112
	<b>Conclusion</b>	<b>115</b>
	<b>A Numerical scheme for the spatio-temporal analysis</b>	<b>123</b>
	<b>B Level set</b>	<b>127</b>
	<b>Bibliography</b>	<b>131</b>
	<b>Curriculum Vitae</b>	<b>139</b>



# Introduction

Improving the understanding of dynamics of immiscible co-axial flows is of fundamental importance in widespread industrial applications, including lubricated transport, injection devices, atomization and controlled microdroplet production, to name a few (figure 1). The developing instabilities can be either detrimental or useful. In lubricated transport (figure 2), the addition of an outer layer of lubricating fluid for drag reduction depends on instabilities at the origin of the formation of an emulsion. In engines exhaust jets, the production of noise is directly related to the formation of axisymmetric toroidal ring vortices, as seen in figure 3. In contrast, in coaxial injection devices, these instabilities help to ensure a rapid and homogeneous mixing between the high velocity fuel injected by a central nozzle and the surrounding low velocity oxydizer injected by a concentric annular nozzle. A cascade of hydrodynamic and capillary instabilities is also responsible for spray formation in atomization devices (Lasheras & Hopfinger (2000)).



**Figure 1** – Examples of co-axial flow. On the left agricultural irrigation, reprinted from Eggers & Villermaux (2008). On the right lubricated pipeline for the oil transportation (INTEVEP, SA).

While the phenomenology of these flows is extremely rich, as illustrated by the abundant terminology coined for that purpose (see for instance figure 2 for a simplified flow map of immiscible core annular flows), it is striking that the frequency and pattern selection are yet exclusively addressed using the framework of the local instability theory of parallel flows. This approach considers a parallel flow profile  $U_z(r)$  independent of the streamwise

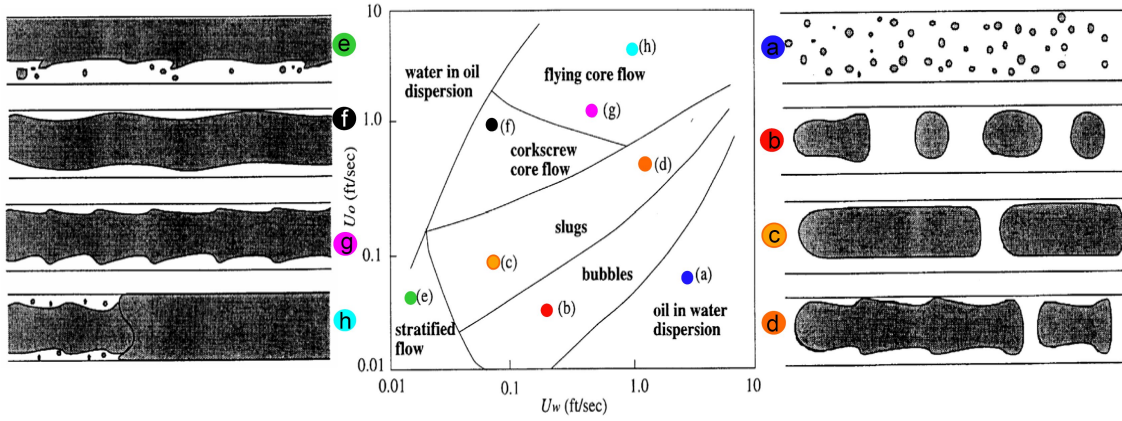


**Figure 2** – Example of instability patterns associated to viscosity contrast in immiscible core-annular flows for lubricated transport in horizontal pipe, when the oil is lighter than the water. Reprinted from Joseph *et al.* (1997).

direction  $z$ , in order to derive a so called dispersion relation, that links the temporal frequency  $\omega$  to the spatial and azimuthal wavenumbers  $k$  and  $m$ . This framework is the basis for a spatio-temporal description of the evolution of perturbations in open flows characterized by a mean advection, based on the distinction between absolute instabilities, that can withstand the mean advection and give birth to self-sustained oscillations and convective instabilities that are advected with the flow, and only amplify incoming perturbations (see Huerre & Monkewitz (1990) for a review).

It is for example well known that a light jet flowing in an heavier medium can be the place of self-sustained well tuned oscillations, characterized by the periodic emission of axisymmetric toroidal vortices (Monkewitz & Sohn (1988)), while iso-density jets are known to behave as noise amplifiers, characterized by a broad frequency response.

Building on this qualitative difference between oscillators (absolutely unstable flows) and noise amplifiers (convectively unstable flows), quantitative predictions were enabled by the development of the nonlinear global mode theory for weakly non parallel flows (see Chomaz (2005) for a review). In this approach, the base flow is chopped into slices, as it evolves downstream and the parallel spatio-temporal instability analysis is extensively repeated on a slice by slice basis. This has enabled to establish that the light jet oscillations indeed had all characteristics of self-sustained nonlinear global modes triggered by a wavemaker front located at the upstream absolute/convective (A/C) transition of the local flow profiles (Lesshafft & Huerre (2007)).

With these successes in mind, renewed interest in parallel flow instability for arbitrary profiles can be observed today, with the analysis of complex physical properties: Juniper & Candel (2003) analyzed the influence of confinement, Lesshafft, Huerre & Sagaut (2007) and Meliga, Sipp & Chomaz (2008) the influence of compressibility, Selvam, Talon, Lesshafft & Meiburg (2009) the instabilities triggered by viscosity contrast in

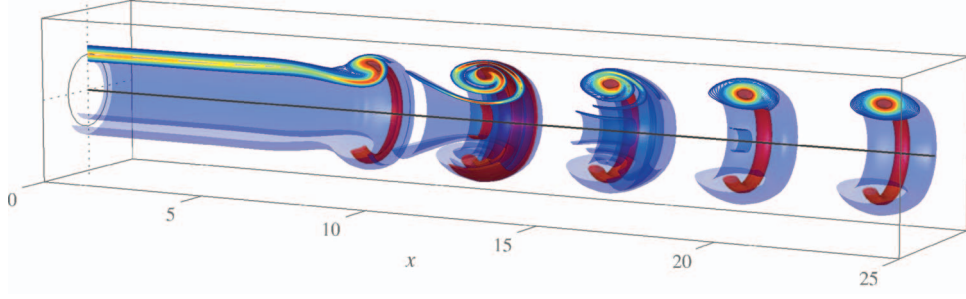


**Figure 3** – Strong sound emissions are the cause of instabilities on light jets, picture from Lesshafft *et al.* (2007).

miscible flows at low Reynolds number. Even immiscible flows (Guillot, Colin, Utada & Ajdari (2007)) were recently subjected to spatio-temporal parallel flow analysis so as to better understand the combined influence of viscosity ratio, velocity ratio, confinement and surface tension. Still, these analysis stopped at this level and the weakly non parallel analysis was not performed, precluding detailed comparisons with experimental measurements like dominant frequencies and wavelengths. Furthermore, in the region of the nozzle exit, the flow is expected to vary very rapidly as it evolves downstream (see figure 4), and global stability analysis is required, that allows one to relax the parallel flow assumption, to the price of computational expense (Theofilis (2003)).

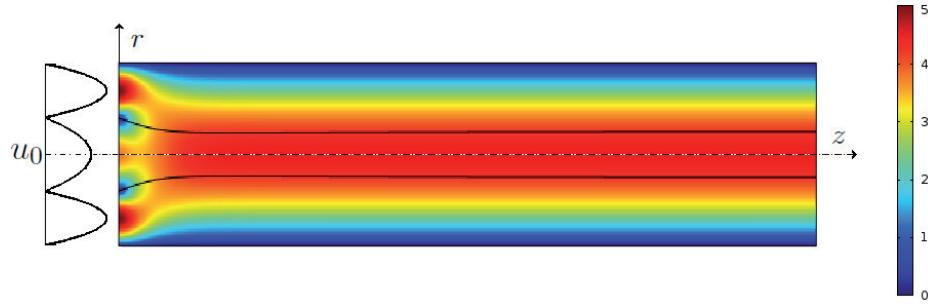


**Figure 4** – Steady base flow of a co-axial Poiseuille flows at Reynolds number  $Re = 0$ . Representation of the streamwise velocity (color map) and interface location (solid continuous line).

### Co-axial jets

The stability of jets and wakes when two immiscible fluids are co-injected is of fundamental importance in several applications. Among them are high Reynolds flows where an inner slow liquid jet is literally peeled by an outer fast gaseous stream. This configuration is an archetype for atomization, and the detailed understanding of its dynamics should open new opportunities for optimization of atomization devices. As reviewed for instance by Lasheras & Hopfinger (2000), the classical scenario proceeds through the following cascade. As far as jets are concerned, a primary axisymmetric instability first deforms the jet surface in the form of toroidal vortices which very soon are subjected to a violent secondary instability breaking the axisymmetry. The resulting ligaments are then accelerated and atomized in droplets by mechanisms which are yet only partially understood (Eggers & Villermaux (2008)).



**Figure 5** – Typical destabilization of a slow water jet  $u_{water} = 0.6m/s$  by a fast coaxial air stream  $u_{air} = 35m/s$ . The primary instability forms ligament which are subsequently broken into droplets. Experiment performed by from Marmottant & Villermaux (2004)

When the Reynolds number is small, the only remaining instability is the so-called Rayleigh-Plateau or capillary instability. This instability, which is also observed in similar but different geometries like a coated cylindrical fiber or inner coated tube (see 6), can be interpreted from an interfacial energy minimization when transitioning from a cylindrical fluid interface to a collection of droplets. This argument also predicts the typical size of the droplets to be formed. Besides this static interpretation, a well-known dynamic interpretation starts from a slightly distorted cylindrical interface. Because of the underpressure (respectively overpressure) resulting from a local crest (resp. trough) along the cylindrical interface resulting from the Laplace pressure jump across the interface, a flow is driven out the throughs into the crests by this pressure imbalance. This flow further enhances the interface distortion: an instability is born. This instability is mediated by the other component of the curvature (the streamwise curvature) intervening in the Laplace pressure jump in addition to the azimuthal curvature driving the instability.

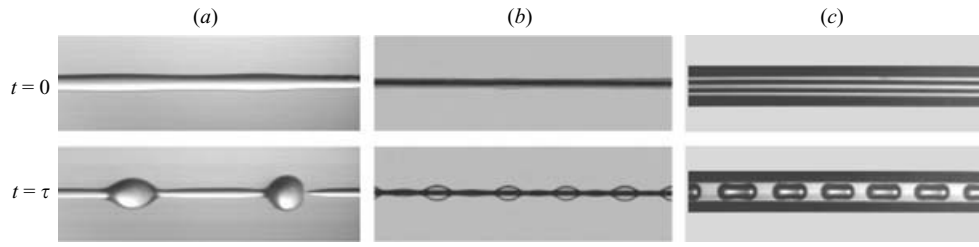


**Figure 6** – Capillary instability of a cylindrical interface for (a) a liquid jet, (b) a liquid film on a fibre, (c) a liquid film in a tube, from Duclaux *et al.* (2006).

Renewed interest in this classical instability has been triggered by the microfluidic coaxial injectors developed to produce microdroplets of prescribed size and rate of emission. This geometry, exemplified in figure 7 was first implemented for microfluidics applications by Cramer, Fischer & Windhab (2004), who inserted a microcapillary into a rectangular flow cell, and showed that the breaking-up of droplets from a capillary tip immersed in a continuous co-flowing liquid could be separated into two distinct regimes: dripping, in which droplets pinch off near the capillary tip, and jetting, in which droplets pinch off from an extended thread downstream of the capillary tip. The transition from dripping to jetting occurs as the continuous phase velocity increases above a critical value in close analogy with the classical jetting/dripping transition from a faucet, as seen in figure 7 (see Clanet & Lasheras (1999) for a more scientific account). They found that the critical velocity decreases as the dispersed phase flow rate increases. Since the interface velocity increases with both dispersed and continuous velocities, this phenomenon can be interpreted as an increased advection of the instability by an increased interface velocity. The critical velocity also decreases as the dispersed phase viscosity increases and as the interfacial tension is reduced.

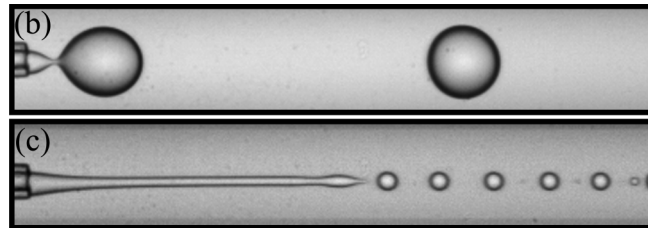


**Figure 7** – Coflowing liquid stream: dripping and jetting regime, experiments from Utada *et al.* (2007).

These trends were confirmed by a series of more recent, local stability analysis of parallel viscous threads confined within a viscous outer liquid in a microchannel, in the limit of vanishing Reynolds number (Utada, Fernandez-Nieves, Gordillo & Weitz (2008); Guillot & Colin (2008); Herrada, Gañán Calvo & Guillot (2008)). These authors interpreted the transition from dripping to jetting as a transition from an absolute to a convective

instability. Recall that this terminology refers to the ability of perturbations to grow and withstand the mean advection. Absolute instabilities grow in place, contaminate the whole domain and yield a self-sustained well-tuned oscillation while convective instabilities are characterized by an irremediable advection of perturbation and behave as noise amplifiers. In co-axial injection devices, an absolutely unstable configuration is expected to result in the self-sustained immediate formation of droplets close to the inlet where the two fluids are put in contact, in contrast, a convectively unstable flow is expected to result in droplets which form only after the instability has grown over a finite downstream distance. While this interpretation is appealing, the scaling laws resulting from the application of the absolute/convective instability theory regarding the frequency and wavelength selection have not been quantitatively verified.

Using a lubrication approximation, Guillot *et al.* (2007) carried out a detailed analysis of the transition as a function of the viscosity ratio, the capillary number and the equilibrium confinement parameter defined as the ratio of the equilibrium jet radius relative to the effective radius of the outer channel, the latter being itself a nonlinear function of both the viscosity and flow rate ratios. For a given confinement parameter, absolute instability holds below a critical capillary number above which the instability becomes convective. This critical capillary number, assumed to trigger the transition from dripping to jetting was found to decrease as the confinement parameter increases, the predicted transition thresholds being in good agreement with the experimental observations. While the whole theory was developed for co-axial cylindrical streams, these authors also considered the influence of the geometry of the outer capillary and showed that the instability was suppressed as soon as the inner jet radius reached the smallest side of rectangular channels.

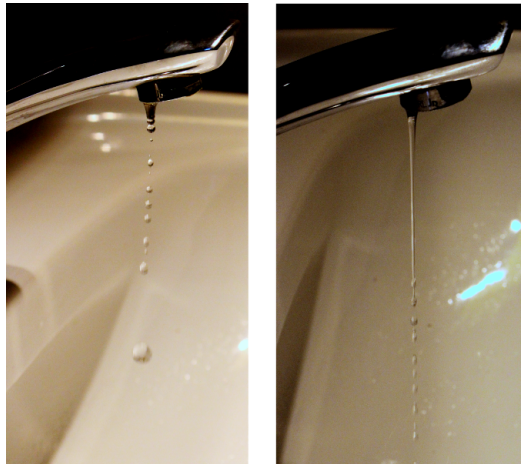


**Figure 8** – Example of home made of dripping and jetting regime.

Cordero, Gallaire & Baroud (2011) have recently conducted an experimental analysis of the base flow in the dripping and jetting regimes which further confirms the relation

of jetting with a convective instability. The authors have showed that convectively unstable flows are indeed suspected to display a broad frequency response, in contrast with absolutely unstable flows for which the response is likely to be overshadowed by the self-sustained mode (Chomaz (2005)).

The studies using global methods have until now been concentrated on wakes behind solid obstacles and detached flows (see Theofilis (2011)), but mainly of single phase flows. A global stability analysis of the two dimensional wake of immiscible flows has been carried out by Tammisola, Lundell & Söderberg (2012), where they have observed a counterintuitive destabilizing effect of the surface tension. Gordillo, Sevilla & Campo-Cortés (2013) studied the dripping to jetting transition of two coaxial streams in the so called tip-streaming regime, where the inner phase presents a cone-jet structure.

## Surface viscosity

The influence of surfactants on these coaxial flows has been much less considered, and the boundary condition on the tangential stress has generally been taken as a free-shear condition, thus neglecting any interfacial mechanical resistance. However, it is well known that surfactant adsorption layers at fluid-fluid interfaces can display a finite elasticity and viscosity (Sagis (2011); Fuller & Vermant (2012)), leading to a drastic modification of boundary conditions from free shear to no slip, or to tip streaming (Anna & Mayer (2006)). The influence of surfactants and of surface viscoelasticity has been studied on liquid threads (Palierne & Lequeux (1991); Hansen, Peters & Meijer (1999); Timmermans & Lister (2002)) or liquid jets with a quiescent surrounding phase, but not in co-axial flow. While the most unstable wavelength still scales like the jet radius (see figure 9 for a home-made illustration), the details of the dispersion relation and the prefactor are affected.

In the general case, coupling surfactant transport and flow is very complex, because it involves several different processes (Edwards, Brenner & Wasan (1991)). Interfacial stretching or compression induced by bulk flows alters the surface concentration of surfactants, hence the surface tension, which can lead to surface tension gradients (Marangoni effect). This is compensated by surface diffusion and, more importantly for soluble surfactants, by adsorption from the bulk, or desorption to the bulk. These exchanges between the bulk and the interface depend on the subphase bulk concentration, and can be limited either by diffusion or by sorption kinetics. The resulting interfacial stress results from this complex interplay, and only in highly simplified situations, such as in the absence of convection (Lucassen & van den Tempel (1972)), can surface elasticity and viscosity be predicted. In other cases, numerical simulations are required and have been used to study e.g. drop detachment (Jin, Gupta & Stebe (2006)).



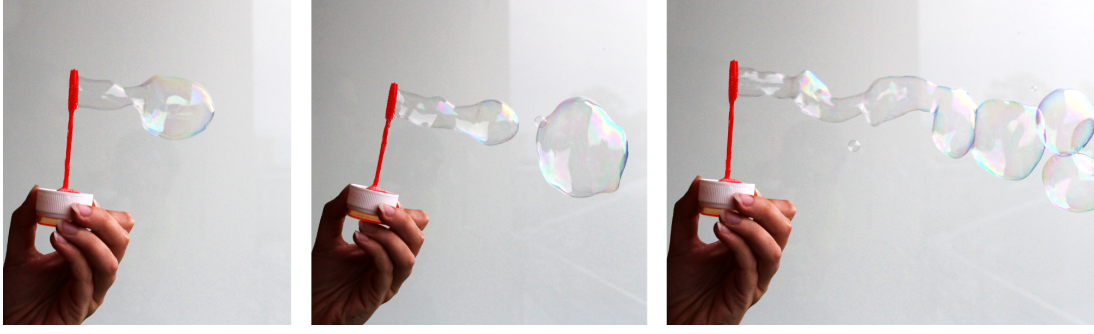


**Figure 9** – Example of free interface. Blowing on a soap bubbles toy, the soap film inflates and forms a hollow jet which destabilizes into a train of soap bubbles. The characteristic wavelength is consistently given by the blowing radius.

## Present work

The major aim of this thesis is to determine the global stability characteristics of spatial developing co-axial jets. This has required the development of new tools for the analysis of immiscible flows. The main task was to cope with two main features of immiscible flows: the existence of a sharp interface separating the fluids and the existence of localized stress discontinuity at the interface between these fluids. The difficulties associated to these features are likely to explain why only parallel flow analysis have been conducted so far. Indeed, in the parallel framework, the flow profile can be either computed from the parallel solution of the two-phase Navier-Stokes equations, or even chosen as an arbitrary velocity profile. Consequently, since no base flow has to be calculated, the nonlinearity introduced by the free interface is simply avoided.

In the present work, we have determined non-parallel base flow solutions from the steady equations themselves, which adds considerable numerical difficulties, as a consequence of the nonlinear free interface problem at hand. Hence, the interface needs to be accurately described by being captured by the numerical scheme. The two fluids are computed on the same fixed grid but the two phases are distinguished by the presence of a function, called level set. The global eigenvalue calculation has been assessed through a linear stability analysis by considering the time evolution of a small perturbation sought in term of normal mode expansion. The global problem is formulated in two different grids, one for each fluid, and the perturbed interface is described by a height function.

Finally, a first qualitative insight whether surfactants may affect co-axial flow instability is given. We have concentrated our analysis on surface viscosity as a source of mechanical resistance. The steady solution and the local stability is performed in the lubrication approximation framework.



The outline is the following. **Chapter 1** gives a general overview of the instabilities of liquid thread and jet in a dynamically inert medium. The principal tools to perform a linear stability are presented. A brief explanation of the link between absolute/convective and global stability is given. **Chapter 2** outlines the effects of a surrounding flow on the stability mechanism of threads and jets. **Chapter 3** tackles the problem of co-axial jets investigating the effect of viscosity ratio, confinement and interfacial tension for both the base flow and the perturbed flow. Finally, **chapter 4** is dedicated to the influence of surface viscosity on a viscous threads and co-axial jets.



# 1 Liquid threads and jets

This chapter modestly aims at giving a brief overview of the instabilities of liquid threads and jets. It is largely inspired by the review by Eggers & Villermaux (2008) but it also contains original material. The phenomenon of the jet breakup involves intricate competition among surface tension, interfacial shear, normal stress and inertial forces of the liquid jet and of the surrounding medium.

Section § 1.1 introduces the governing equations used throughout this chapter. Section § 1.2 presents a reduction of the problem to 1D simplified model based on long-wavelength assumption, while section § 1.3 describes the linear stability analysis and the linearized governing equations. Sections § 1.4 presents the physical mechanisms leading to breakup of a thread of fluid at rest immersed in a constant pressure medium remaining at rest, while section § 1.5 describes a infinite jet breakup.

## 1.1 Hydrodynamic description of jets

We consider an incompressible fluid injected into a dynamically inert medium. The jet has density  $\rho$ , viscosity  $\mu$ , surface tension  $\gamma$ , radius  $h$  and mean velocity  $u_0$  (as sketched in figure 1.1). The gravity effect as well as the effect of the surrounding environment are neglected.

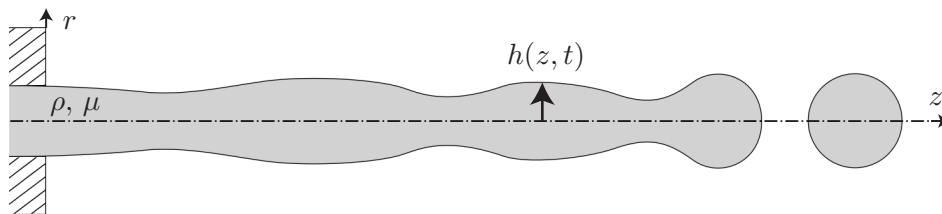


**Figure 1.1** – Flow domain and notations used in the chapter.

## Chapter 1. Liquid threads and jets

---

To outline the description of a thread or a jet, we need to investigate the relative importance of fluid inertia, viscosity force and surface tension. This description can be made introducing the following non dimensional numbers:

- the Reynolds number relates the inertial forces and the viscous forces

$$Re = \frac{\rho u_0 h}{\mu}, \quad (1.1)$$

- the Weber number measures the relative importance of the kinetic energy respect to the surface energy

$$We = \frac{\rho h u_0^2}{\gamma}, \quad (1.2)$$

- the Capillary number compares the viscous forces to the surface tension

$$Ca = \frac{\mu u_0}{\gamma}, \quad (1.3)$$

- the Ohnesorge number measures the relative importance of the viscous forces with respect to the inertial and surface tension forces

$$Oh = \frac{\mu}{\sqrt{\rho \gamma h}}. \quad (1.4)$$

This four dimensionless group are related through the relations  $Ca = We/Re$  and  $Oh = \sqrt{We}/Re$ .

The governing equations for the jet are the incompressible Navier-Stokes equations in axisymmetric coordinates  $(r, z)$ . The flow variable are the velocity  $\mathbf{u} = u\mathbf{e}_z + v\mathbf{e}_r$  and the pressure  $p$ .

$$\partial_t \mathbf{u} + (\mathbf{u} \cdot \nabla) \mathbf{u} = -\frac{1}{\rho} \nabla p + \nu \Delta \mathbf{u} \quad (1.5)$$

$$\nabla \cdot \mathbf{u} = 0 \quad (1.6)$$

where  $\nu = \mu/\rho$  is the kinematic viscosity.

The jet interface moves at the same speed of the fluid. If we introduce the height function  $h(z, t)$ , to describe the surface, then the motion of the interface is described by the kinematic equation

$$\partial_t h + u \partial_z h = v|_{r=h} \quad (1.7)$$

At the free interface the stress balance is given by

$$\boldsymbol{\sigma} \cdot \mathbf{n}|_{r=h} = -\gamma \mathcal{C} \mathbf{n} \quad (1.8)$$

where

$$\boldsymbol{\sigma} = -p\mathbb{I} + \mu \left( \nabla \mathbf{u} + (\nabla \mathbf{u})^T \right) \quad (1.9)$$

is the stress tensor. The unit normal vector  $\mathbf{n}$  to the interface pointing outward to the dynamically inert medium is defined as

$$\mathbf{n} = \frac{(-\partial_z h, 1)}{(1 + \partial_z h)^{1/2}}. \quad (1.10)$$

The mean curvature  $\mathcal{C}$  is define as  $\mathcal{C} = -\nabla \cdot \mathbf{n}$ , and in cylindrical coordinates can be written as

$$\mathcal{C} = \frac{1}{h(1 + h'^2)^{1/2}} - \frac{h''}{(1 + h'^2)^{3/2}}, \quad (1.11)$$

where the prime denotes the derivation with respect to  $z$ . Hence the shape of the interface  $h(z, t)$  is coupled to the flow equations throw the stress conditions and the interface kinematic equation.

The fully axisymmetric analysis of the free surface flows can become a significant challenge and a computationally intensive task. A reduction of the problem to one dimensional simplified model based on the long-wavelength description will give huge savings in computer time. We will show, that the main advantage of the long-wavelength assumption is that is simple and transparent. In the picture, additional ingredients can be easily incorporated. The long-wavelength approximation becomes a powerful tool to study different kinds of threads and jets.

## 1.2 Long-wavelength description

Since the works of Eggers & Dupont (1994) and Brenner, Shi & Nagel (1994), the long-wavelength approximation has been widely used. The Eggers & Dupont (1994) work provides a good comparison between the reduced model and the numerical results on the full equation. Eggers & Villiermaux (2008) give an exhaustive overview of the long-wavelength model comparing the results with the exact solution of the Navier-Stokes equation for few cases, while the work of van Hoeve, Gekle, Snoeijer, Versluis, Brenner & Lohse (2010) gives a good agreement between the theory and the experimental results obtained with the high speed imaging system.

The long-wavelength approximation can be extended to other configuration, as the hollow jet (Eggers & Villiermaux (2008)), or can be studied to a higher order including the

non-linear effects (Bechtel, Bolinger, Cao & Forest (1995), Eggers (1997)). We have applied the long-wavelength assumption to a viscous thread with surface dilation (see § 4.2).

In the following, the essential steps leading to the long-wavelength equations are explained. The main idea is that the typical radial length  $l_r$  of a liquid jet is much smaller than the its longitudinal scale  $l_z$ . In this case the velocity and pressure fields can be expand in Taylor series around  $r = 0$ :

$$u(z, r, t) = u_0(z, t) + u_2(z, t)r^2 + \dots \quad (1.12)$$

$$v(z, r, t) = -\frac{1}{2} \frac{\partial u_0}{\partial z} r - \frac{1}{4} \frac{\partial u_2}{\partial z} r^3 - \dots \quad (1.13)$$

$$p(z, r, t) = p_0(z, t) + p_2(z, t)r^2 + \dots \quad (1.14)$$

the longitudinal velocity  $u$  is described by a uniform flow  $u_0$  and a second order correction term  $u_2$ . The expanded fields are inserted into the Navier-Stokes equation and it is solved at the lowest order of  $r$ . The normal and the tangential stress conditions close the system giving a reduced form of the original equation:

$$\frac{\partial u_0}{\partial t} = -u_0 \frac{\partial u_0}{\partial z} - \frac{\gamma}{\rho} \frac{\partial \mathcal{C}}{\partial z} + 3\nu \left[ \frac{2}{h} \frac{\partial h}{\partial z} \frac{\partial u_0}{\partial z} + \frac{\partial^2 u_0}{\partial z^2} \right] \quad (1.15)$$

The prefactor of the viscous term  $3\nu$  is called the Trouton viscosity and it comes from the fact that the elongation viscosity, in an axisymmetric extensional flow, is three times the shear viscosity (Trouton (1906)).

The kinematic equation (1.7), at the leading order, gives:

$$\frac{\partial h}{\partial t} = -u_0 \frac{\partial h}{\partial z} - \frac{1}{2} \frac{\partial u_0}{\partial z} h \quad (1.16)$$

The set of linear equations (1.15)-(1.16) is a coupled system of equation for the uniform velocity  $u_0$  and the interface height  $h$ . In the following,  $u_0 \equiv u$  is replaced for a more fluid reading.

The full axisymmetric system is now reduced to one-dimensional model and the free surface motion is given in explicit form. The advantages of this reduced method is that allow to explore the parameter space in faster and more efficient way than the solve the full Navier-Stokes equations. Furthermore it allow a better understanding of the effect of the liquid viscosity, density, surface tension and jet velocity on the breakup mechanism and a more insight view of the competition between the characteristic inertia timescale and viscous timescale.

In the following we use the reduced model to describe the stability of some well know flow

cases (e.g. inviscid jet, viscous thread), comparing the results with the exact formula, if it exists, or with the numerical results.

### 1.3 Stability analysis

Since the pioneer work of Rayleigh (1879) the most basic and powerful tool to analyze the physical mechanism leading to breakup is the linear stability analysis. The stability analysis is made by assuming small disturbances, so that the governing equations can be linearized around the steady state. The flow variable  $\mathbf{Q} = (\mathbf{U}, P, H)$  is decomposed into one steady state  $\bar{\mathbf{q}} = (\bar{\mathbf{u}}, \bar{p}, h)$  and one small perturbation  $\mathbf{q}' = (\mathbf{u}', p', \eta)$ :

$$\begin{aligned} \mathbf{U}(r, z, t) &= \bar{\mathbf{u}}(r, z) + \varepsilon \mathbf{u}'(r, z, t) \\ P(r, z, t) &= \bar{p}(r, z) + \varepsilon p'(r, z, t) \\ H(z, t) &= h(z) + \varepsilon \eta(z, t) \end{aligned} \tag{1.17}$$

where  $\varepsilon \ll 1$ .

The Navier-Stokes equations (2.1)-(1.6), the kinematic equation (1.7) and the stress condition (1.8) for the linear evolution of the perturbations can be written as:

$$\partial_t \mathbf{u}' + (\bar{\mathbf{u}} \cdot \nabla) \mathbf{u}' + (\mathbf{u}' \cdot \nabla) \bar{\mathbf{u}} = -\frac{1}{\rho} \nabla p' + \nu \Delta \mathbf{u}' \tag{1.18}$$

$$\nabla \cdot \mathbf{u}' = 0 \tag{1.19}$$

$$\partial_t \eta + \bar{u} \partial_z \eta + u' \partial_z h + \eta \partial_r \bar{u} \partial_z h = v' + \eta \partial_r \bar{v} |_{\partial\Omega} \tag{1.20}$$

$$\bar{\sigma} \cdot \mathbf{n}' + \sigma' \cdot \bar{\mathbf{n}} + \eta \partial_r \bar{\sigma} \cdot \bar{\mathbf{n}} |_{\partial\Omega} = -\gamma (\bar{\mathcal{C}} \mathbf{n}' + \mathcal{C}' \bar{\mathbf{n}}) \tag{1.21}$$

where the perturbed stress tensor is

$$\sigma' = -p' \mathbb{I} + \mu (\nabla \mathbf{u}' + (\nabla \mathbf{u}')^T) \tag{1.22}$$

while the perturbed unit vector

$$\mathbf{n}' = \frac{(-\partial_z \eta, -\partial_z h \partial_z \eta)}{(1 + \partial_z h)^{3/2}} \tag{1.23}$$

and the perturbed curvature  $\mathcal{C}' = -\nabla \mathbf{n}'$ .

The stability of a liquid jet can be carried out with three different approaches. In the first approach (i) the perturbations  $\mathbf{q}'(r, z, t)$  can sought in normal modes form  $\hat{q}(r) e^{i(kz - \omega t)}$ , where  $k \in \mathbb{R}$  is the wavenumber and  $\omega \in \mathbb{C}$  is the complex wave frequency. Describing  $\hat{q}(r)$  with the Stokes current function, the solution of (1.18)-(1.21) can be written as

combination of Bessel functions. In few cases it is possible to determine an exact explicit analytical dispersion relation  $\omega = f(k)$ .

Or in alternative way (ii),  $\hat{q}(r)$  is discretized by Chebyshev polynomials in radial direction and a numerical dispersion relation is obtained where the wave frequency  $\omega$  is the eigenvalue of

$$A(k)q(r) = \omega B(k)q(r) \quad (1.24)$$

where is the the state vector discretized on the Gauss-Lobatto collection (GLC) nodes.  $A(k)$  and  $B(k)$  are respectively the stiffness and the mass matrices function of the wavenumber  $k$  (for details see Canuto, Hussaini, Quarteroni & Zang (1993)).

Another approach is linearize directly the long-wavelength description of the Navier-Stokes equations (1.15)-(1.16)

$$\frac{\partial u'}{\partial t} = -\bar{u} \frac{\partial u'}{\partial z} - u' \frac{\partial \bar{u}}{\partial z} + \frac{\gamma}{\rho} \frac{\partial}{\partial z} \left( \frac{\eta}{h^2} + \frac{\partial^2 \eta}{\partial z^2} \right) \quad (1.25)$$

$$+ 3\nu \left[ -\frac{2\eta}{h^3} \frac{\partial h}{\partial z} \frac{\partial \bar{u}}{\partial z} + \frac{2}{h} \frac{\partial \eta}{\partial z} \frac{\partial \bar{u}}{\partial z} + \frac{2}{h} \frac{\partial h}{\partial z} \frac{\partial u'}{\partial z} + \frac{\partial^2 u'}{\partial z^2} \right]$$

$$\frac{\partial \eta}{\partial t} = -u' \frac{\partial h}{\partial z} - \bar{u} \frac{\partial \eta}{\partial z} - \frac{1}{2} \frac{\partial u'}{\partial z} h - \frac{1}{2} \frac{\partial \bar{u}}{\partial z} \eta \quad (1.26)$$

The equations (1.25)-(1.26) are independent of the coordinate  $r$ , then is not necessary discretize  $\hat{q}(r)$ . The applied normal mode expansion is  $\mathbf{q}'(z, t) = e^{i(kz - \omega t)}$ . This last approach allows to obtain an explicit dispersion relation. The power of this method lies on its mathematical simplicity.

In the following, in progressive manner, the physical mechanisms leading to breakup are introduce. The dispersion relation obtained with the linearization of the long-wavelength approximation is compared with the exact solution of the linearized Navier-Stokes equations. If an explicit form of the linearized governing equations does not exist, the comparison is made with the numerical results of the Chebyshev discretization.

### 1.4 Liquid thread

The stability analysis is initially applied to the study of an infinitely long liquid thread  $\bar{\mathbf{u}} = 0$  with a constant height  $h(z) = h_0$ . Two limit case are introduced (inviscid and purely viscous thread) and a general dispersion relation is given. In the next section § 1.5, the velocity is introduced, and the stability of jets is discussed.



### 1.4.1 Inviscid thread

We initially consider an inviscid thread  $\nu = 0$ . The linearized governing equations (1.25)-(1.26) are:

$$\frac{\partial u'}{\partial t} = \frac{\gamma}{\rho} \frac{\partial}{\partial z} \left( \frac{\eta}{h_0^2} + \frac{\partial^2 \eta}{\partial z^2} \right) \quad (1.27)$$

$$\frac{\partial \eta}{\partial t} = -\frac{1}{2} h_0 \frac{\partial u'}{\partial z} \quad (1.28)$$

injecting the normal mode expansion the following dispersion relation is yielded:

$$\omega^2 = -\frac{1}{2} \frac{\gamma}{\rho h_0^3} \left( (kh_0)^2 - (kh_0)^4 \right) \quad (1.29)$$

The characteristic inertial timescale of (1.29) is determined by

$$\tau_i = \sqrt{\frac{\rho h_0^3}{\gamma}} \quad (1.30)$$

and it describes the competition between inertia and surface tension, therefore the time  $\tau_i$  gives an estimation of the total time for the breakup. The instability, called Rayleigh-Plateau instability, is caused by the action of the surface tension, which tends to destabilize a fluid system to create another one with the same volume but smaller surface area.

The above dispersion relation can be compared with the Rayleigh (1879) exact solution:

$$\omega^2 = -\frac{1}{\tau_i^2} (kh_0) \left[ 1 - (kh_0)^2 \right] \frac{I_1(kh_0)}{I_0(kh_0)} \quad (1.31)$$

The long-wavelength dispersion relation (1.29) not only has a good agreement with the exact equation (1.31), as shown in figure 1.2, but also catches the cut-off  $k_c h_0 = 1$  and the most amplified wavenumber  $k_m h_0 = \sqrt{2}/2$ .

### 1.4.2 Viscous thread

For a viscous thread the inertial terms can be consider negligible compare to the viscous terms. The linearized governing equations (1.25)-(1.26) are:

$$0 = \frac{\gamma}{\rho} \frac{\partial}{\partial z} \left( \frac{\eta}{h_0^2} + \frac{\partial^2 \eta}{\partial z^2} \right) + 3\nu \frac{\partial^2 u'}{\partial z^2} \quad (1.32)$$

$$\frac{\partial \eta}{\partial t} = -\frac{1}{2} h_0 \frac{\partial u'}{\partial z} \quad (1.33)$$

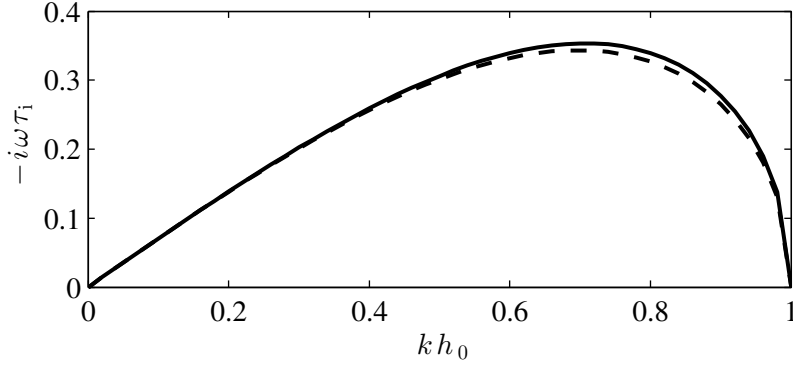


**Figure 1.2** – Dimensionless growth rate  $-i\omega\tau_1$  as function of the dimensionless wavenumber  $kh_0$  for an inviscid thread. The long-wavelength approximation (continuous line) fits well the Rayleigh exact solution (dashed line).

injecting the normal mode expansion  $\mathbf{q}'(r, z, t) = \hat{q}(r)e^{i(kz - \omega t)}$ , the following dispersion relation is yielded:

$$-i\omega = \frac{1}{6} \frac{\gamma}{\mu h_0} (1 - (kh_0)^2) \quad (1.34)$$

As for the inviscid thread, in the equation (1.36) it is possible recognize a characteristic timescale

$$\tau_v = \frac{\mu h_0}{\gamma} \quad (1.35)$$

it is called characteristic viscous timescale and it describes the competition between viscous force and surface tension.

The comparison with the Rayleigh (1892) exact solution

$$-i\omega = \frac{1}{2\tau_v} \frac{1 - (kh_0)^2}{1 + (kh_0)^2 \left[ 1 - (I_0(kh_0)/I_1(kh_0))^2 \right]} \quad (1.36)$$

gives a perfect agreement, as shown in figure 1.3, and the cut-off is still  $k_c h_0 = 1$ . Both dispersion relations, long-wavelength description (1.34) and exact solution (1.36), involve  $\omega$  and not  $\omega^2$ , since the  $\partial_t u$  term drops out in the viscous limit. The system predicts the most amplified wavenumber a zero wavelength  $k_m h_0 = 0$  and therefore the inertia-less limit is ill-posed.

The inertia effect can be neglected if  $\tau_v \gg \tau_1$ , in other words if

$$\frac{\mu}{\sqrt{\gamma \rho} h_0} \gg 1 \quad (1.37)$$

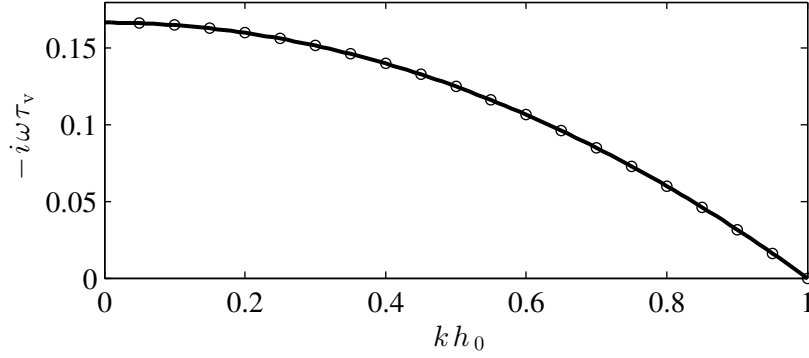


**Figure 1.3** – Dimensionless growth rate  $-i\omega\tau_v$  as function of the dimensionless wavenumber  $kh_0$  for a viscous thread. The long-wavelength description (continuous line) fits perfectly the exact solution (circles).

that is exactly the Ohnesorge number (1.4). Hence the Ohnesorge number can be expressed as the ratio of the viscous timescale  $\tau_v$  and its inertial counterpart  $\tau_i$

$$Oh = \frac{\tau_v}{\tau_i} \quad (1.38)$$

The Ohnesorge number, therefore, describes the relative importance of the viscous terms over the inertial effects for a thread.

### 1.4.3 Viscous thread with inertia

In order to have a well-posed problem in the viscous thread, the inertial term  $\partial_t u$  has to be taken into account. In this case the linearized governing equations are:

$$\frac{\partial u'}{\partial t} = \frac{\gamma}{\rho} \frac{\partial}{\partial z} \left( \frac{\eta}{h_0^2} + \frac{\partial^2 \eta}{\partial z^2} \right) + 3\nu \frac{\partial^2 u'}{\partial z^2} \quad (1.39)$$

$$\frac{\partial \eta}{\partial t} = -\frac{1}{2} h_0 \frac{\partial u'}{\partial z} \quad (1.40)$$

the associated dispersion relation is:

$$\omega^2 = -\frac{1}{2} \frac{\gamma}{\rho} \frac{1}{h_0^3} \left( (kh_0)^2 - (kh_0)^4 \right) - i\omega \frac{3\nu}{h_0^2} (kh_0)^2 \quad (1.41)$$

the thread is not anymore prone to instability at zero wavelength. The growth rate is then determined by a balance of surface tension, viscous force and inertia effect and the breakup is determined by the competition of the inertial and viscous time scales.

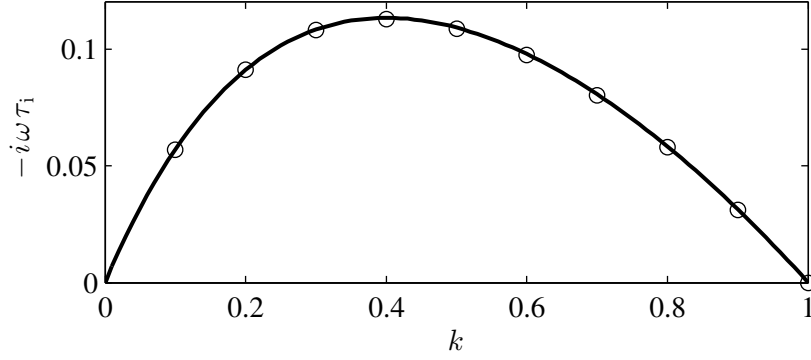


**Figure 1.4** – Growth rate  $-i\omega\tau_i$  as function of the wavenumber  $k$  for a viscous thread where the inertial term  $\partial_t u$  is taken into account. Comparison between long-wavelength approximation (line) and numerical results of the Chebyshev discretization of the Navier-Stokes equation (circle) for a thread with  $Oh = 1$ .

The most amplified wavenumber is

$$k_m h_0 = \frac{\sqrt[4]{\rho\gamma h_0}}{\sqrt{2\sqrt{\rho\gamma h_0} + 3\sqrt{2}\mu}} \quad (1.42)$$

and the cut-off remains unvaried  $k_c h_0 = 1$ . For this case, there is not an explicit form for the exact dispersion relation (for the details see Chandrasekhar (1961) and Timmermans & Lister (2002)) and the equations are solved numerically with Chebyshev. The comparison between the long-wavelength approximation and the numerical results gives a perfect agreement (figure 1.4).

In order to study the stability of a viscous thread both inertial and viscous timescale are to be taken into account. Hence, the dispersion relation (1.41) can be rewritten in dimensionless form using both the inertial timescale or the viscous timescale:

$$-i\omega\tau_i = \sqrt{\frac{1}{2}(x^2 - x^4) + \frac{9}{4}Oh^2 x^4} - \frac{3}{2}Ohx^2 \quad (1.43)$$

$$-i\omega\tau_v = Oh\sqrt{\frac{1}{2}(x^2 - x^4) + \frac{9}{4}Oh^2 x^4} - \frac{3}{2}Oh^2 x^2 \quad (1.44)$$

Figure 1.5 shows the deformation of the growth rate as the Ohnesorge number is increased. If  $Oh \rightarrow 0$  the inviscid limit is retrieved with  $k_m h_0 = \sqrt{(2)}/2$ , while if  $Oh \rightarrow \infty$  the purely viscous limit is found with  $k_m h_0 = 0$ .

Also the most amplified wavenumber (1.42) can be rewritten as function of the Ohnesorge

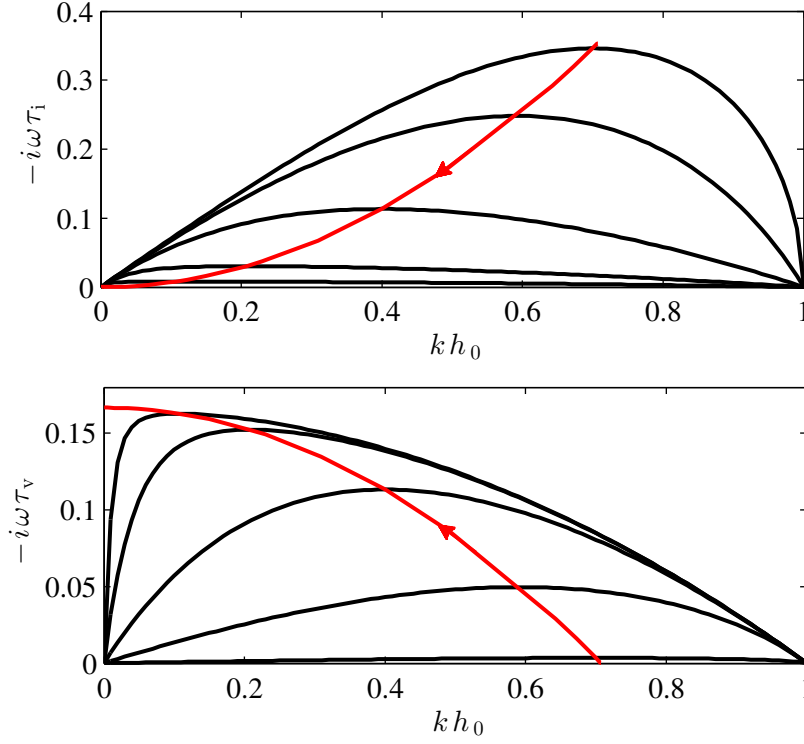


**Figure 1.5** – Dispersion relation  $-i\omega\tau_i$  (above) and  $-i\omega\tau_v$  (below) for increasing Ohnesorge number  $Oh^{-1} = \tau_i/\tau_v = \{100, 5, 1, 0.2, 0.05\}$ . The red lines are the locus of points where the most amplified wavenumber occurs.

number:

$$k_m h_0 = \frac{1}{\sqrt{2 + 3\sqrt{2}Oh}} \quad (1.45)$$

Figure (1.6) shows a growth rate  $-i\omega\tau_i$  for  $Oh = 1/2$ . The inviscid and purely viscous limit curves are the two asymptotical behavior of the dimensional curve. The growth rate is well described from the inviscid theory ( $Oh \rightarrow 0$ ) for small value of the wavenumber, while the purely viscous limit ( $Oh \rightarrow \infty$ ) have a perfect agreement for large value of  $k$ .

## 1.5 Liquid jets

So far situations where the disturbances are spatially uniform have been analyzed. A liquid thread always breaks into droplets (fig. 1.7). As the velocity of the jet  $\bar{\mathbf{u}} = u_0 \mathbf{e}_z$  is increased a transition from dripping to jetting regime occurs. Now the perturbations which grow in time are simultaneously convected downstream and a continuous jet can persist in the system.

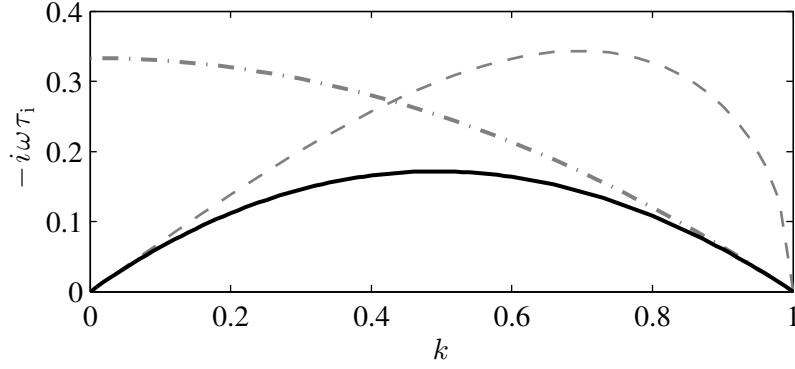


**Figure 1.6** – Growth rate  $-i\omega\tau_1$  for a liquid thread with  $\tau_1 = 1$  and  $Oh = 1/2$ . Comparison with the inviscid limit  $Oh \rightarrow 0$  (dashed line) and the viscous limit  $Oh \rightarrow \infty$  (dash-dot line).

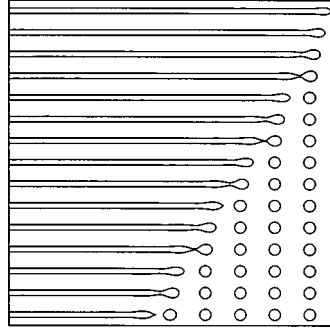


**Figure 1.7** – Front propagation of the Rayleigh instability of a viscous thread with viscosity ratio  $\lambda = \mu/\mu_{medium} = 0.05$  at  $t_n = 6.67n\mu_{medium}h_0/\gamma$  with  $n = 1, 2, \dots, 5$  from top to bottom. Figure reprinted from Powers *et al.* (1998).

Historically the distinction between absolute and convective instability come from the literature on plasma (Briggs (1964) and Bers (1983)). Since the pioneer work of Huerre & Monkewitz (1990) the absolute/convective (A/C) theory has widely applied to fluid instabilities. The flow is convectively unstable if the perturbations are amplified while moving away from the disturbance source, on the other hand, the flow is absolutely unstable when the amplified perturbations grow on the entire flow. While in the temporal stability analysis the wavenumber  $k$  is supposed real and the wave frequency  $\omega$  complex, conversely, in the A/C analysis the nature of the instability is determined by applying the Briggs-Bers zero-group velocity criterion to the dispersion relation for both wavenumber and wave frequency complex. In order to determine the transition from absolute to convective regime it is sufficient to identify the saddle point of the associated spatio-temporal analysis, i.e. determine the complex value of the complex wave number  $k_0$  such

that

$$\frac{\partial \omega_r}{\partial k_r} = \frac{\partial \omega_i}{\partial k_r} = 0. \quad (1.46)$$

The discrimination between absolutely and convectively unstable flow explains the transition from jetting to dripping in two-phase immiscible microfluidic co-axial flow Guillot *et al.* (2007), as well different regimes occurring in the pearl forming instability of a film flowing down a fiber Duprat, Ruyer-Quil & Giorgiutti-Dauphiné (2009).

An unstable perturbation travel with the complex group velocity

$$v_g = \frac{\partial \omega}{\partial k} \quad (1.47)$$

and if we denote  $k_0$  and  $\omega_0$  the absolute wavenumber and frequency respectively, the pair  $(k_0, \omega_0)$  is given by the zero group velocity condition

$$v_g^\pm(k_0) = 0 \quad \text{s.t.} \quad \omega_0 = \omega(k_0) \quad (1.48)$$

When the absolute wave frequency  $\text{Im}(\omega_0) < 0$  the flow is convectively unstable, while when  $\text{Im}(\omega_0) > 0$  the flow is absolutely unstable. In both case the flow is linearly unstable, however the absolutely or convectively instabilities lead to different scenario, how will see in the following.

When the flow is convectively unstable ( $\text{Im}(\omega_0) < 0$ ), the waves packet increases with time but it is convected downstream faster than it spread across the flow, and the receding front is positive  $v_g^- > 0$ , as shown in figure 1.8. On the other hand, when the flow is absolutely unstable ( $\text{Im}(\omega_0) > 0$ ), the perturbation grows exponentially and withstands the mean advection. In this case the receding front is negative  $v_g^- < 0$  and the perturbation travel upstream.

In fact, a sister theory of the absolute/convective instability concept is due to Van Saarloos (1989) and is sometimes referred to as marginal stability criterion (Powers *et al.* (1998)) It consists of identifying the edge velocities by the following three conditions

$$\frac{\partial \omega_i}{\partial k_r} = 0, \quad v_g^\pm = \frac{\omega_i}{k_i}, \quad v_g^\pm = \frac{\partial \omega_i}{\partial k_i} \quad (1.49)$$

The relevance of these linear edge velocities extends in fact far beyond the intrinsic limitations expected from a linear analysis. The nonlinear front separating the base state from the invading unstable nonlinearly saturated state can be shown in many cases to inherit the linear edge velocity, as exemplified in figure 1.7 where the nonlinear saturated state is played by the droplets. This linear criterion for the nonlinear front propagation

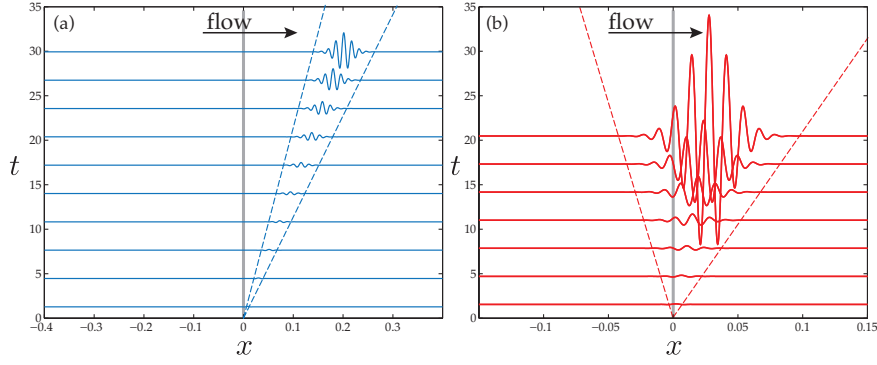


**Figure 1.8** – Spatio-temporal evolution of two perturbation packets. The packet (a) is convectively unstable, while (b) is absolutely unstable. Reprinted from Brun *et al.* (2015).

is one of the cornerstones of modern nonlinear global mode theories (see Chomaz (2005) for a review).

In systems affected by uniform advection  $U > 0$  as the jets considered in this section, there is a natural link between the absolute/convective properties and the receding edge velocity. The flow is convective if  $U > |v^-|$  and absolute otherwise.

### 1.5.1 Inviscid jet

For an inviscid jet  $\mu = 0$ , with constant longitudinal velocity  $u_0$  and radius  $h_0$ , the linearized governing equations (1.25)-(1.26) are:

$$\frac{\partial u'}{\partial t} = -u_0 \frac{\partial u'}{\partial z} + \frac{\gamma}{\rho} \frac{\partial}{\partial z} \left( \frac{\eta}{h_0^2} + \frac{\partial^2 \eta}{\partial z^2} \right) \quad (1.50)$$

$$\frac{\partial \eta}{\partial t} = -u_0 \frac{\partial \eta}{\partial z} - \frac{1}{2} h_0 \frac{\partial u'}{\partial z} \quad (1.51)$$

the associated dispersion relation is

$$\omega = u_0 k + i \frac{\sqrt{2}}{2\tau_i} \sqrt{(kh_0)^2 - (kh_0)^4} \quad (1.52)$$

Respect to the inviscid thread, in the linearized equations for an inviscid jet, there are two more terms  $u_0 \partial_z u'$  in the momentum and  $u_0 \partial_z \eta$  in the kinematic equations. The contribution of the jet velocity does not change the growth rate  $w_i$  only the frequency  $w_r$ . The frequency is not anymore zero but is a linear function of the wavenumber:

$$\omega_r = u_0 k. \quad (1.53)$$



If we define the dimensionless wave frequency and wavenumber as

$$\tilde{\omega} = \omega \tau_1, \quad \tilde{k} = kh_0 \quad (1.54)$$

the dispersion relation (1.52) can be written as

$$\tilde{\omega} = \sqrt{We} \tilde{k} + i \sqrt{\frac{1}{2} (\tilde{k}^2 - \tilde{k}^4)} \quad (1.55)$$

Hence, the Weber number  $We$  is sufficient to describe the stability of an inviscid jet. The calculation of the jetting/dripping transition with the long-wavelength description shows that the an inviscid jet has enough kinetic energy to overcome the surface energy, when

$$We > 4. \quad (1.56)$$

Below this critical Weber number the inviscid jet is absolutely unstable, otherwise it is convectively unstable. Conversely, the determination of the A/C transition performed by Leib & Goldstein (1986)-Le Dizès (1997) on the exact dispersion relation gives the transition at  $We \sim 3.15$ . The discretize of the two critical Weber number is due to the long-wavelength approximation.

### 1.5.2 Viscous jet

For a viscous jet the inertial terms can be consider negligible compare to the viscous terms. The linearized governing equations (1.25)-(1.26) are:

$$0 = \frac{\gamma}{\rho} \frac{\partial}{\partial z} \left( \frac{\eta}{h_0^2} + \frac{\partial^2 \eta}{\partial z^2} \right) + 3\nu \frac{\partial^2 u'}{\partial z^2} \quad (1.57)$$

$$\frac{\partial \eta}{\partial t} = -u_0 \frac{\partial \eta}{\partial z} - \frac{1}{2} h_0 \frac{\partial u'}{\partial z} \quad (1.58)$$

injecting the normal mode expansion  $\mathbf{q}'(r, z, t) = \hat{q}(r) e^{i(kz - \omega t)}$ , the following dispersion relation is yielded:

$$\omega = u_0 k + \frac{1}{6\tau_v} i \left( 1 - (kh_0)^2 \right) \quad (1.59)$$

as for the viscous thread, the viscous jet is ill-posed problem since it predicts the most amplified wavenumber at zero wavelength.

In this case, we define the dimensionless wave frequency as:

$$\tilde{\omega} = \omega \tau_v \quad (1.60)$$

## Chapter 1. Liquid threads and jets

---

and the dimensionless dispersion relation becomes:

$$\tilde{\omega} = Ca\tilde{k} + \frac{1}{6}i(1 - \tilde{k}^2). \quad (1.61)$$

For a purely viscous effect, the Capillary number  $Ca$  is sufficient to describe the linear stability. The calculation of the absolute/convective transition shows that the absolute wavenumber and frequency are respectively

$$k_0 = -3iCa \quad (1.62)$$

$$\omega_0 = -\frac{3}{2}iCa^2 + i\frac{1}{6}. \quad (1.63)$$

A viscous thread has enough energy to overcome the surface tension and then maintain the jetting regime when

$$Ca > \frac{1}{3} \quad (1.64)$$

Below this critical value of the Capillary number the jet is absolutely unstable and therefore the liquid jet breaks up.

### 1.5.3 Viscous jet with inertia

The translation invariance is not anymore broken ( $\omega(k=0) = 0$ ) if also the inertial term are taken into account in the stability analysis. In this case the associated dispersion relation can be written as:

$$\omega = u_0k - \frac{3i}{2}\frac{Oh}{\tau_1}(kh_0)^2 + \frac{i}{\tau_1}\sqrt{\frac{1}{2}((kh_0)^2 - (kh_0)^4) + \frac{9}{4}Oh^2(kh_0)^4} \quad (1.65)$$

where the growth rate is same found for the thread and the frequency is linear respect to the wavenumber. Also for this case, the long-wavelength approximation gives a very perfect agreement with the numerical discretization of the Navier-Stokes equations with Chebyshev polynomials (figure 1.9).

The Ohnesorge number is independent on the velocity and therefore it is not anymore sufficient to describe the behavior of a liquid jet. If we define the dimensionless wave frequency and wave number as

$$\tilde{\omega} = \omega \frac{\mu h_0}{\gamma}, \quad \tilde{k} = kh_0 \quad (1.66)$$

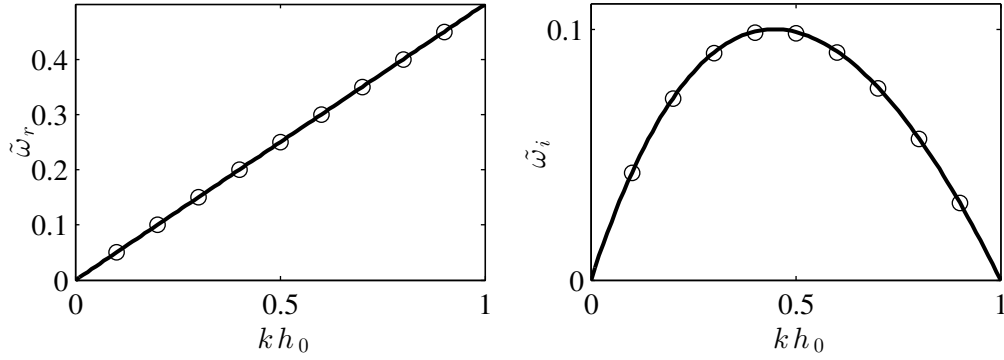


**Figure 1.9** – Frequency  $\tilde{\omega}_r$  and growth rate  $\tilde{\omega}_i$  as function of  $kh_0$  for a viscous jet with inertia contribution. Comparison between long-wavelength approximation (line) and numerical results (circle) for a jet with  $Oh = 0.7$  and  $Ca = 1$ .

the dispersion relation (1.65) can be rewritten as:

$$\tilde{\omega} = Ca\tilde{k} - \frac{3}{2}iOh^2\tilde{k}^2 + iOh\sqrt{\frac{9}{4}Oh^2\tilde{k}^4 + \frac{1}{2}(\tilde{k}^2 - \tilde{k}^4)} \quad (1.67)$$

where  $Ca$  is the Capillary number. To describe the stability of a liquid jet only two adimensional number are necessary: Ohnesorge  $Oh$  and Capillary  $Ca$  number.

Ohnesorge (1936) in his work developed an operative diagram in  $(Re, Ca)$ -plane to distinguish dripping and jetting regime (figure 1.10). The transition appears to be a power law relationship between the Reynolds and Ohnesorge number. More recently Derby (2010) proposed an operating diagram for drop-on-demand inkjet printing as power law of Reynolds and Weber number (figure 1.11).

In conclusion, we have analyzed, in progressive manner, the physical mechanism leading to breakup of a liquid jet immersed in a dynamically inert medium. We have seen that the stability of the jet can be studied with the long-wavelength description, and that it can always be described by one or two adimensional numbers. We have also observed, that while for a liquid thread the instability is always an absolute instability, for a jet the transition from absolute to convective instability occurs. In the last case, criteria that allows to distinguish from the two regimes are given in function of the adimensional numbers.

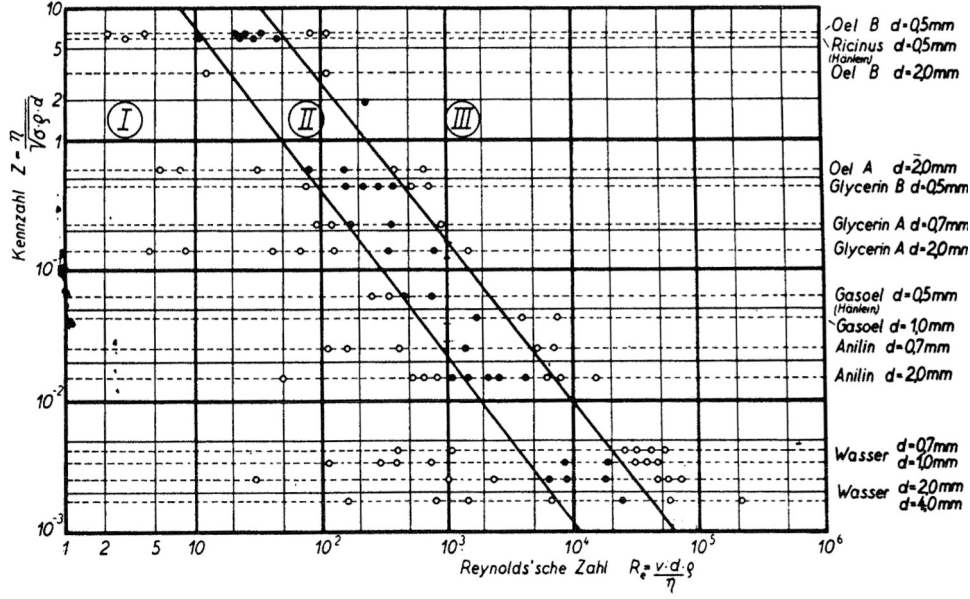


**Figure 1.10** – Ohnesorge operative diagram. The power law allows to distinguish the dripping (i), the jetting (ii) and the wind induced regime (iii). The Kennzahl number  $Z$  in this work is referred as the Ohnesorge number. Reprinted from Ohnesorge, ZAMN, 16, 1936.

## 1.6 Relationship between absolute/ convective and global stability

The stability properties of weakly non-parallel flows, that are slowly developing in space, are conveniently described by local stability analysis and the associated absolute/convective instability theory (Huerre & Monkewitz, 1990). In contrast, strongly spatially developing flows are better analyzed in a global stability framework (Chomaz, 2005). Trying to understand the links between the two approaches, Heaton, Nichols & Schmid (2009) found that the global instability modes of an  $x$ -independent parallel base flow are equivalent to its absolute instability modes. These global modes include appropriate boundary conditions at the upstream and downstream locations, while the absolute modes are given by the dispersion relation of the system. However, their analysis was based on a two-dimensional flow that required numerical calculations for the obtention of both the global and absolute modes. By contrast, we present here a similar analysis on a simpler one-dimensional system, which allows for the analytical retrieval of these modes and their direct comparison.

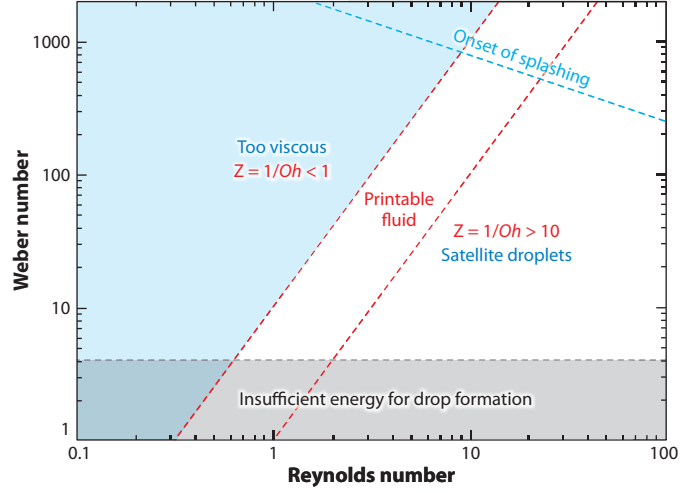


**Figure 1.11** – Derby operative diagram for drop-on-demand injecting printing. According to Derby’s criterion, a drop has sufficient kinetic energy to be ejected from the nozzle if  $We > 4$  and  $Re < 2/Oh$ . Instead, the onset of splashing is given by the criterion  $OhRe^{5/4} > 50$ . Reprinted from Derby (2010).

### 1.6.1 System description and local stability analysis

We consider an axisymmetric viscous jet flowing along the  $z$ -direction in a dynamically inert medium. The base flow is formed by the jet of viscosity  $\mu$  moving downstream at constant velocity  $u_0$  and having constant radius  $h_0$ . Inertial terms are neglected, and all quantities are made nondimensional using the length scale  $h_0$  and the viscous time scale  $\tau_v = \mu h_0 / \gamma$ , where  $\gamma$  is the surface tension of the jet. In order to perform a local stability analysis, the extent of the flow in the  $z$ -direction is supposed infinite, so that small perturbations of the interface position around its equilibrium value may be expanded into normal modes  $\eta(z, t) \sim e^{i(kz - \omega t)}$ . Inserting this expansion in the linearized governing equations leads to the following dispersion relation

$$\omega = Ca k + \frac{i}{6}(1 - k^2), \quad (1.68)$$

where  $Ca = \mu u_0 / \gamma$  is the capillary number (for details see § 1.5.2). This dispersion relation exhibits a range of unstable wavenumbers  $0 \leq k < 1$  and the maximum growth rate is attained at  $k = 0$ . The absolute wavenumber  $k_0$  observed on the ray  $z/t = 0$  in the laboratory frame is given by the following zero group velocity condition

$$\frac{d\omega}{dk}(k_0) = 0 \quad \Rightarrow \quad k_0 = -3iCa, \quad (1.69)$$

and the corresponding absolute frequency  $\omega_0$  follows as

$$\omega_0 = \omega(k_0) = -\frac{3}{2}i\text{Ca}^2 + \frac{i}{6}. \quad (1.70)$$

An absolute to convective instability transition therefore occurs when the absolute growth rate  $\omega_{0,i}$  changes sign

$$\omega_{0,i} = \text{Im } \omega_0 = 0 \quad \Rightarrow \quad \text{Ca} = \frac{1}{3}. \quad (1.71)$$

### 1.6.2 Global stability analysis

In reality, the system is bounded and the flow enters and exits the domain at streamwise locations  $z = 0$  and  $z = l$ , respectively. The perturbations thus need to be zero at these locations, resulting in the following boundary conditions

$$\eta(0, t) = \eta(l, t) = 0. \quad (1.72)$$

Hence, the Fourier expansion used in the local analysis is no longer applicable. Instead, note that a linearized differential equation for the time evolution of the perturbations can be recovered from the dispersion relation (1.68)

$$\frac{\partial \eta}{\partial t} = -\text{Ca} \frac{\partial \eta}{\partial z} + \frac{1}{6} \eta(z, t) + \frac{1}{6} \frac{\partial^2 \eta}{\partial z^2}, \quad (1.73)$$

which, interestingly, turns out to be a specific case of the linearized Ginzburg-Landau model equation. The perturbation may then be expanded in global modes

$$\eta(x, t) = \bar{\eta}(z) e^{\lambda t}. \quad (1.74)$$

that can be inserted in (1.73) to give the following boundary value problem

$$\left( \lambda - \frac{1}{6} \right) \bar{\eta}(z) = -\text{Ca} \frac{d\bar{\eta}}{dz} + \frac{1}{6} \frac{d^2 \bar{\eta}}{dz^2}, \quad (1.75)$$

with the boundary conditions  $\bar{\eta}(0) = \bar{\eta}(l) = 0$ . This can be seen as an eigenvalue problem where  $\lambda$  are the eigenvalues and  $\bar{\eta}(z)$  the eigenvectors. Expanding the eigenvectors as  $\bar{\eta}(z) = \hat{\eta} e^{\alpha z}$  leads to the following quadratic equation for  $\alpha$

$$\alpha^2 - 6\text{Ca}\alpha + 1 - 6\lambda = 0, \quad (1.76)$$

the roots of which are given by

$$\alpha_{1,2} = 3\text{Ca} \pm \frac{1}{2} \sqrt{36\text{Ca}^2 + 24\lambda - 4}. \quad (1.77)$$

## 1.6. Relationship between absolute/ convective and global stability

The eigenvectors are thus expressed as the linear combination  $\bar{\eta}(z) = \hat{\eta}_1 e^{\alpha_1 z} + \hat{\eta}_2 e^{\alpha_2 z}$ . To find admissible values for  $\lambda$ , we make use of the boundary conditions to write

$$\begin{bmatrix} 1 & 1 \\ e^{\alpha_1 l} & e^{\alpha_2 l} \end{bmatrix} \begin{bmatrix} \hat{h}_1 \\ \hat{h}_2 \end{bmatrix} = \begin{bmatrix} 0 \\ 0 \end{bmatrix}. \quad (1.78)$$

Setting the determinant of the above matrix to zero yields the condition

$$e^{\alpha_2 l} - e^{\alpha_1 l} = 0 \quad \Rightarrow \quad \alpha_1 - \alpha_2 = i \frac{2\pi m}{l} \quad \Rightarrow \quad \sqrt{36\text{Ca}^2 + 24\lambda_m - 4} = i \frac{2\pi m}{l}, \quad (1.79)$$

where  $m$  is an integer. The admissible values for the global frequencies  $\lambda_m$  then follow as

$$\lambda_m = -\frac{3}{2}\text{Ca}^2 + \frac{1}{6} - \frac{m^2 \pi^2}{6l^2} = -i\omega_0 - \frac{m^2 \pi^2}{6l^2}, \quad (1.80)$$

where  $\omega_0$  is the absolute frequency given in (1.70) by local stability analysis. One therefore observes that the most amplified global frequency  $\lambda_0$  corresponds to the absolute frequency, i.e.  $\lambda_0 = -i\omega_0$ ! Thus it is not surprising that the flow becomes globally unstable, meaning  $\lambda_{0,r} > 0$ , at the same capillary number  $\text{Ca} = 1/3$  for which the instability becomes convective in the local analysis. Also, the sequence of global frequencies for  $m = 1, 2, \dots$  form a branch that emanates out of the absolute frequency and in which consecutive modes have spacing that scales with  $1/l^2$ . Finally, from the values of the frequencies  $\lambda_m$ , we can recover the shape of the corresponding global eigenmodes

$$\bar{\eta}_m(z) = \hat{\eta}_1 (e^{\alpha_1 z} - e^{\alpha_2 z}) = 2i\hat{\eta}_1 e^{3\text{Ca}z} \sin \frac{m\pi z}{l}. \quad (1.81)$$

It is seen that the global mode  $\bar{\eta}_0$  associated with the most amplified global frequency does not oscillate. As a final remark, we note that the strong exponential growth of the eigenmodes in the axial direction observed by Heaton *et al.* (2009) appears explicitly here in the term  $e^{3\text{Ca}x}$ . Our expression also confirms that eigenmodes still exist for large domain sizes  $l$ , and the convergence issues encountered by Heaton *et al.* (2009) were indeed of numerical nature.





## 2 Threads and jets in a surrounding flow

In this chapter, we outline the effect of a surrounding flow on the stability mechanism of threads and jets. Initially the analysis is focused on the effect quiescent external medium. In a second moment the dynamic of the jet and the external flow is added.

### 2.1 Hydrodynamic description of jets and surrounding flow

We consider an incompressible fluid injected throw a nozzle in a surrounding medium. The jet has density  $\rho_1$ , viscosity  $\mu_1$ , surface tension  $\gamma$ , radius  $h$  and mean velocity  $u_0$ . Let  $\rho_2$  and  $\mu_2$  the density and the viscosity of an incompressible medium surrounding the jet. The external medium is initially unbounded (as sketched in figure 2.1).

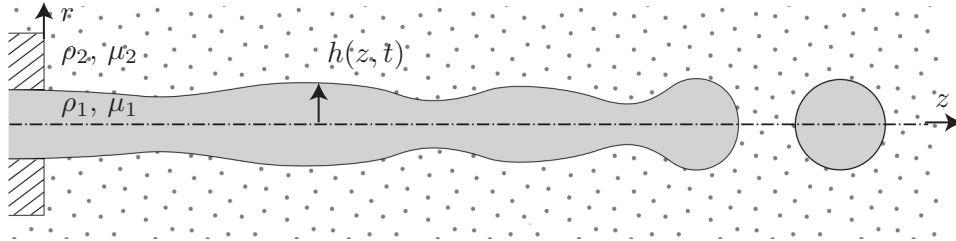


**Figure 2.1** – Flow domain and notations used in the chapter

The governing equations for the jet and for the external matrix are the incompressible Navier-Stokes equations in axisymmetric coordinates  $(r, z)$ :

$$\partial_t \mathbf{u}_i + (\mathbf{u}_i \cdot \nabla) \mathbf{u}_i = -\frac{1}{\rho_i} \nabla p_i + \nu_i \Delta \mathbf{u}_i \quad (2.1)$$

$$\nabla \cdot \mathbf{u}_i = 0 \quad (2.2)$$

where the subscripts  $i = \{1, 2\}$  denote respectively the jet and outer medium.

The jet interface has to move at the same velocity of the near jet. Like in the first chapter the interface motion can be describe by the kinematic equation

$$\partial_t h + u_i \partial_z h = v_i|_{r=h} \quad (2.3)$$

Along the interface the continuity of the velocity has to be respected

$$\mathbf{u}_1 = \mathbf{u}_2|_{r=h} \quad (2.4)$$

as well the stress condition

$$(\sigma_1 - \sigma_2) \cdot \mathbf{n}|_{r=h} = -\gamma \mathcal{C} \mathbf{n} \quad (2.5)$$

The definition of the unit normal vector  $\mathbf{n}$  and the mean curvature  $\mathcal{C}$  is the same given the for the jets in the void

$$\mathbf{n} = \frac{(-\partial_z h, 1)}{(1 + \partial_z h)^{1/2}} \quad (2.6)$$

$$\mathcal{C} = \frac{1}{h(1 + h'^2)^{1/2}} - \frac{h''}{(1 + h'^2)^{3/2}} \quad (2.7)$$

The tools necessary to describe the stability of the system are already described in § 1.3.

Initially the stability analysis is applied to the study of a liquid thread with constant height  $h(z, t) = h_0$  surrounding by a quiescent external matrix. Two limit case are introduced (inviscid thread in an inviscid surrounding and purely viscous thread in viscous surrounding) and a general relation between the wavenumber and growth rate is given. In a second step, the velocity is introduced, both for the jet and the medium, and we will show that the linear stability analysis can not be used unless we compute the dynamics of the base flow. Finally the case of two confined parallel co-axial jets at low Reynolds number is presented.

## 2.2 Threads in a quiescent external medium

### 2.2.1 Inviscid thread immersed in a quiescent inviscid medium

Let  $\rho_2$  the density of the quiescent inviscid medium surrounding an inviscid thread of constant height  $h(z) = h_0$  and density  $\rho_1$ . The effect of an inviscid surrounding matrix on the instability of an inviscid thread can be approached, also for this case, with the long-wavelength description. The strategy is coupled the response of the thread and of the external medium throw two one-dimensional equations. For the thread, the contribution

## 2.2. Threads in a quiescent external medium

---

of the outer pressure enter in the  $z$ -momentum

$$\frac{\partial u_1}{\partial t} = -\frac{1}{\rho_1} \frac{\partial p_1}{\partial z} \quad (2.8)$$

where the normal stress condition gives

$$p_1 = p_2(r = h_0) + \gamma \mathcal{C} \quad (2.9)$$

Instead the outer medium responds to the interface deformation, contracting and expanding radially:

$$\frac{\partial v_2}{\partial t} = -\frac{1}{\rho_2} \frac{\partial p_2}{\partial r} \quad (2.10)$$

$$\frac{1}{r} \frac{\partial(rv_2)}{\partial r} = 0 \quad (2.11)$$

using the kinematic equation  $v_2(r = h_0) = \partial_t h$  and the continuity of the velocity at the interface  $v_1(r = h_0) = v_2(r = h_0)$ , from the continuity equation (2.11) one finds the external radial velocity as function of the interface position

$$v_2 = \frac{h \partial_t h}{r} \quad (2.12)$$

which, inserted into (2.10), gives

$$\frac{1}{r} \left( \frac{\partial h}{\partial t} \right)^2 + \frac{h}{r} \frac{\partial^2 h}{\partial t^2} = -\frac{1}{\rho_2} \frac{\partial p_2}{\partial r} \quad (2.13)$$

and keeping only the linear term in the perturbation:

$$\frac{h}{r} \frac{\partial^2 h}{\partial t^2} = -\frac{1}{\rho_2} \frac{\partial p_2}{\partial r} \quad (2.14)$$

Integrating (2.14) and using (2.9), an expression of the inner pressure is obtained

$$p_1 = \rho_2 h \frac{\partial^2 h}{\partial t^2} \log \left( \frac{1 + kh}{kh_0} \right) + \gamma \mathcal{C} \quad (2.15)$$

and therefore the dispersion relation can be written as:

$$\left[ 1 + \frac{1}{2} \frac{\rho_2}{\rho_1} (kh_0)^2 \log \left( 1 + \frac{1}{kh_0} \right) \right] \omega^2 = -\frac{1}{2\tau_1^2} \left( (kh_0)^2 - (kh_0)^4 \right) \quad (2.16)$$

The dispersion relation is characterized by two dimensional group, the inertial time scale  $\tau_i = \sqrt{\rho_1 h_0^3 / \gamma}$  and the density ratio  $\rho = \rho_1 / \rho_2$ . The above equation (2.16) can be

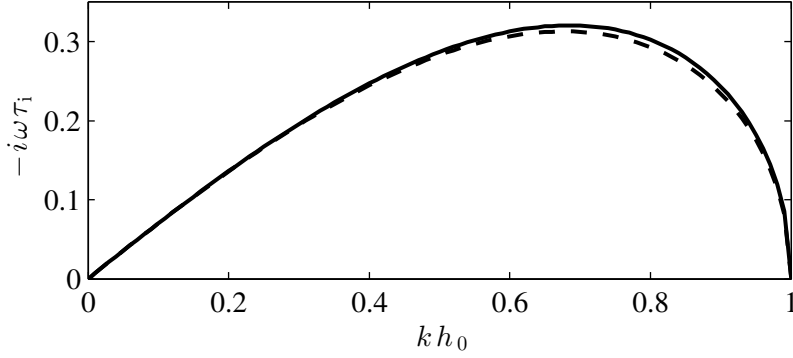


**Figure 2.2** – Dimensionless growth rate  $-i\omega\tau_i$  as function of the dimensionless wavenumber  $kh_0$  for an inviscid thread of density in a quiescent external inviscid medium with  $\rho_1/\rho_2 = 1$ . The long-wavelength approximation (continuous line) fits well the Rayleigh exact solution (dashed line).

compared with Rayleigh's exact solution

$$\left[1 + \frac{\rho_2}{\rho_1} \frac{K_0(kh_0)I_1(kh_0)}{K_1(kh_0)I_0(kh_0)}\right] \omega^2 = -\frac{1}{\tau_i^2}(kh_0) \left[1 - (kh_0)^2\right] \frac{I_1(kh_0)}{I_0(kh_0)} \quad (2.17)$$

and they have a good agreement as shown in figure 2.2. The small overestimation of the long-wavelength approximation, found in the inviscid thread without external medium, remains if the effect of the external inertia is take into account.

The presence of an inviscid external medium reduces the instability and shifts the most amplified wavenumber toward smaller  $k$  compare to the inviscid thread immersed in a dynamically inert medium, as shown in figure 2.3. However the cut-off remain unchanged  $k_ch_0 = 1$ . The original dispersion relation (1.29) is recovered if  $\rho_2/\rho_1 \rightarrow 0$ , while the opposite limit  $\rho_2/\rho_1 \rightarrow \infty$  gives the dispersion equation for the hollow jet:

$$\omega^2 = -\frac{\gamma}{\rho_2 h_0^3} \frac{1 - (kh_0)^2}{\log\left(1 + \frac{1}{kh_0}\right)} \quad (2.18)$$

### 2.2.2 Inviscid thread immersed in a quiescent viscous medium

The limit case of an inviscid thread immersed in an inviscid medium can be easily extended to the case of inviscid thread immersed in a viscous medium  $\mu_2 \neq 0$ . The inner thread and outer medium are connected to each other throw the continuity of the velocity at the free interface and the normal stress condition. To compute the inner pressure  $p_1$  a

## 2.2. Threads in a quiescent external medium

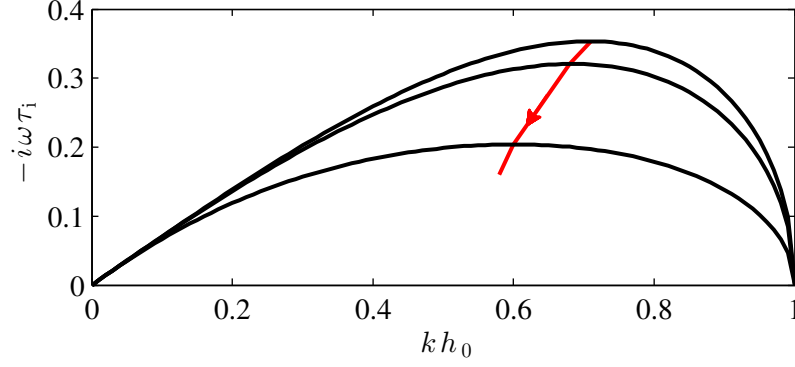


**Figure 2.3** – Dimensionless growth rate  $-i\omega\tau_i$  as function of the dimensionless wavenumber  $kh_0$  for an inviscid thread of density  $\rho$  in a quiescent external medium of density  $\rho_a$ , for decreasing value of  $\rho_1/\rho_2 = \{10^5, 1, 0.1\}$

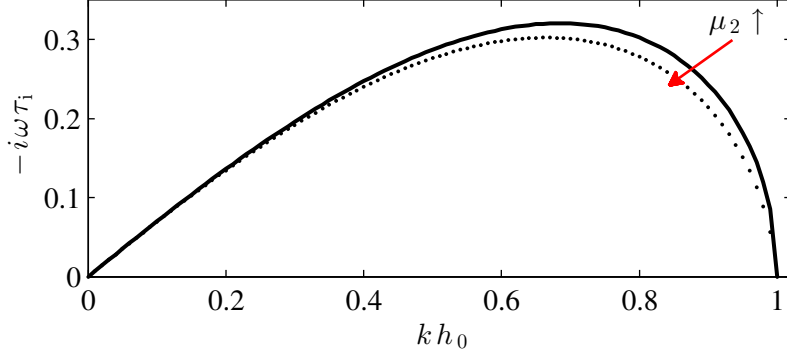


**Figure 2.4** – Dimensionless growth rate  $-i\omega\tau$  as function of the dimensionless wavenumber  $kh_0$  for an inviscid thread in a quiescent external medium with  $\rho_1/\rho_2 = 1$ , for increasing viscosity of the outer medium  $\mu_2 = \{0, 0.1\}$

contribution of the viscous stress has to be added to (2.9)

$$p_1 = p_2(r = h_0) + \gamma\mathcal{C} - 2\mu_2 \frac{\partial v_2}{\partial r} \quad (2.19)$$

with similar calculations discussed above, the new dispersion relation can be written as

$$\left[1 + \frac{1}{2} \frac{\rho_2}{\rho_1} (kh_0)^2 \log \left(1 + \frac{1}{kh_0}\right)\right] \omega^2 = -\frac{1}{2\tau_i^2} \left((kh_0)^2 - (kh_0)^4\right) + (-i\omega) \frac{\mu_2}{\rho_1 h_0^2} (kh_0)^2 \quad (2.20)$$

The presence of an external viscous medium slows down the instability and shift the most amplified wavenumber towards a smaller value of  $k$  compared with the thread in an inviscid surrounding. Also, in this case also the cut-off remains unchanged  $k_c h_0 = 1$ .

### 2.2.3 Viscous thread immersed in a quiescent viscous medium

For the case of a viscous thread immersed in a quiescent viscous medium is not any longer possible use the long-wavelength approximation. If also the inner thread is viscous, in the dispersion relation the shear has to be taken into account, and in the long-wavelength approximation also the second order correction term  $v_2$  of the streamwise velocity (1.12) has to be included in the equation.

In the case of viscous thread and viscous matrix, Tomotika (1935) generalized the Rayleigh equation (1.36) for an arbitrary viscosity ratio  $\lambda = \mu_1/\mu_2$  giving an explicit expression of the growth rate

$$-i\omega = \frac{\gamma}{2\mu_1 h} \frac{(1 - (kh_0)^2) \left( \frac{K_1}{K_0} V_1 \mu_2 + \frac{I_1}{I_0} V_2 \mu_1 \right)}{\left( \frac{\mu_2}{\mu_1} - 1 \right) \left( \frac{K_1}{K_0} V_1 V_3 \mu_2 - \frac{I_1}{I_0} V_2 V_4 \mu_2 \right) + (kh_0) \left( 2 + \frac{I_0 K_1}{I_1 K_0} + \frac{I_1 K_0}{I_0 K_1} \right) \mu_1} \quad (2.21)$$

where the following abbreviations hold

$$\begin{aligned} V_1 &= (kh_0) \left( \frac{I_1}{I_0} - \frac{I_0}{I_1} \right) + 2 \\ V_2 &= (kh_0) \left( -\frac{K_1}{K_0} + \frac{K_0}{K_1} \right) + 2 \\ V_3 &= (kh_0)^2 \left( 1 - \frac{K_0^2}{K_1^2} \right) + 1 \\ V_4 &= (kh_0)^2 \left( \frac{I_0^2}{I_1^2} - 1 \right) - 1 \end{aligned} \quad (2.22)$$

and all the Bessel functions are function of  $kh_0$ . In the dispersion relation we can recognize the characteristic viscous timescale  $\tau_v = \frac{\gamma}{\mu_1 h_0}$ .

Stone & Brenner (1996) obtained a direct and elegant derivation for the case of iso-viscosity  $\lambda = 1$  and found

$$-i\omega = \frac{\gamma}{\mu h_0} \left( I_1 K_1 + \frac{kh_0}{2} (I_1 K_0 - I_0 K_1) \right) \quad (2.23)$$

As shown on figure 2.5, the presence of an external viscous matrix slows down the instability, the thread becomes more stable as the viscosity ratio increase, maintaining the cut-off unvaried  $k_c h_0 = 1$ . The most amplified wavenumber is reached for non-zero wavenumber, unless for the limit case  $\lambda = \infty$  or  $\lambda = 0$ . In these two limit cases (viscous thread in the void and hollow jet) the most amplified wave number is  $k_m h_0 = 0$ . Translation invariance  $\omega(k=0) = 0$  is not broken for finite viscosity ratio. From the figure 2.5, we can easily observe that the value of the most amplified wavenumber varies with the value of the viscosity ratio. The variation of  $k_m h_0$  is not a monotonous function of  $\lambda$  and reaches the maximum at  $\lambda \sim 0.28$ , as shown on figure 2.6.

## 2.2. Threads in a quiescent external medium

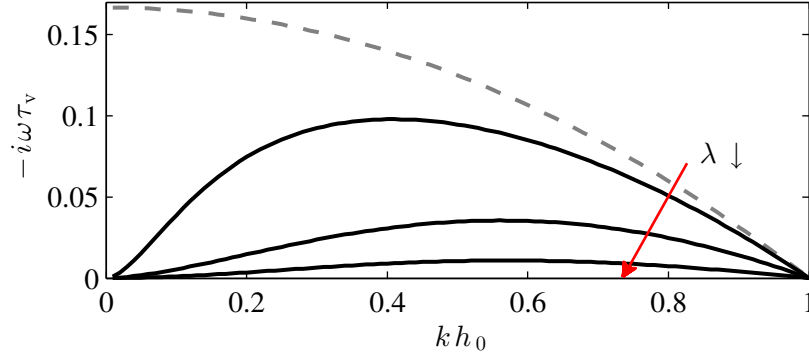


**Figure 2.5** – Dimensionless growth rate  $-i\omega\tau_v$  as function of the dimensionless wavenumber  $kh_0$  for a viscous thread in a viscous matrix. Dispersion relation plotted for decreasing value of viscosity ratio  $\lambda = \{\infty, 10, 1, 0.1\}$ .

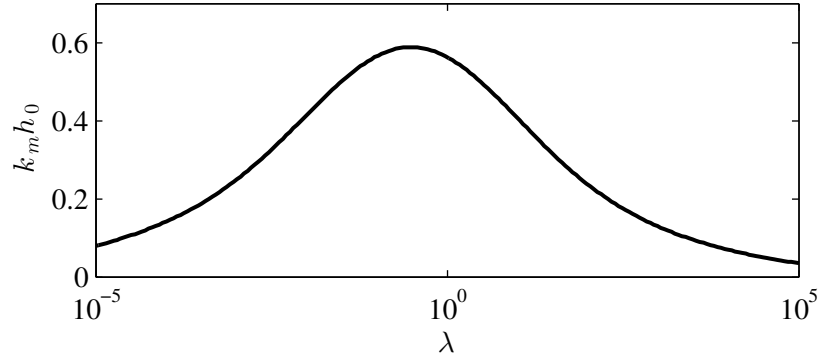


**Figure 2.6** – Most amplified wavenumber  $k_m h_0$  as function of the viscosity ratio  $\lambda$  for a viscous thread in a viscous matrix.

Tomotika (1935) derived also an explicit dispersion relation for the hollow jet  $\lambda = 0$

$$-i\omega = \frac{\gamma}{2h_0\mu_2} \frac{1 - (kh_0)^2}{(kh_0)^2 + 1 - (kh_0)^2 \frac{K_0^2}{K_1^2}}. \quad (2.24)$$

### 2.2.4 Viscous thread with inertia in a quiescent viscous medium

As final step the analysis of the most general case of a thread with density  $\mu_1$  and viscosity  $\rho_1$  surrounding by a quiescent medium with density  $\rho_2$  and  $\mu_2$  is provided. Like for the viscous thread, the long-wavelength assumption is not anymore applicable, and in addition an explicit analytical dispersion relation does not exist. Hence the dispersion relation is obtain numerically.

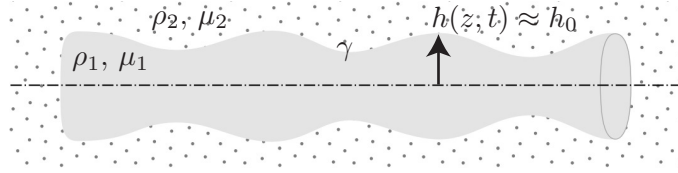


**Figure 2.7** – Sketch liquid thread in a surrounding medium and notations.

The linearized Navier-Stokes equations can be made dimensionless with two different timescale: the inertial  $\tau_i$  or the viscous  $\tau_v$  timescale. In the first case (i) if the time scale is  $\tau_i$ , the length scale  $h_0$ , and remembering that the pressure is related to the curvature through the Laplace law  $\Delta p = p_1 - p_2 = \gamma \mathcal{C}$ , we can set:

$$t = \tau_i \tilde{t}, \quad \mathbf{u}' = \frac{h_0}{\tau_i} \tilde{\mathbf{u}}, \quad p' = \frac{\gamma}{h_0} \tilde{p}, \quad r = h_0 \tilde{r}, \quad z = h_0 \tilde{z}, \quad \eta = h_0 \tilde{\eta} \quad (2.25)$$

and the adimensional linearized Navier-Stokes equations and boundary conditions can be written as

$$\frac{1}{Oh} \partial_{\tilde{t}} \tilde{\mathbf{u}}_1 = -\frac{1}{Oh} \nabla \tilde{p}_1 + \Delta \tilde{\mathbf{u}}_1 \quad (2.26)$$

$$\frac{1}{\rho} \frac{1}{Oh} \partial_{\tilde{t}} \tilde{\mathbf{u}}_2 = -\frac{1}{Oh} \nabla \tilde{p}_2 + \frac{1}{\lambda} \Delta \tilde{\mathbf{u}}_2 \quad (2.27)$$

$$\nabla \tilde{\mathbf{u}} = 0 \quad (2.28)$$

$$\partial_{\tilde{t}} \tilde{\eta} = \tilde{v}_1 \quad (2.29)$$

$$\tilde{\mathbf{u}}_1 = \tilde{\mathbf{u}}_2|_{r=h} \quad (2.30)$$

$$\left( -\tilde{p}_1 \mathbb{I} + Oh \left( \nabla \tilde{\mathbf{u}}_1 + (\nabla \tilde{\mathbf{u}}_1)^T \right) + \tilde{p}_2 \mathbb{I} - \frac{Oh}{\lambda} \left( \nabla \tilde{\mathbf{u}}_2 + (\nabla \tilde{\mathbf{u}}_2)^T \right) \right) \tilde{\mathbf{n}} = \tilde{\mathcal{C}} \tilde{\mathbf{n}} \quad (2.31)$$

In contrast (ii) if for the timescale  $\tau_v$  is introduced and we set

$$t = \tau_v \tilde{t}, \quad \mathbf{u}' = \frac{h_0}{\tau_v} \tilde{\mathbf{u}}, \quad p' = \frac{\gamma}{h_0} \tilde{p}, \quad r = h_0 \tilde{r}, \quad z = h_0 \tilde{z}, \quad \eta = h_0 \tilde{\eta} \quad (2.32)$$

The dimensionless linearized Navier-Stokes equation and boundary conditions can be



read as

$$\frac{1}{Oh^2} \partial_t \tilde{\mathbf{u}} = -\nabla \tilde{p} + \Delta \tilde{\mathbf{u}} \quad (2.33)$$

$$\frac{1}{\rho} \frac{1}{Oh^2} \partial_t \tilde{\mathbf{u}} = -\nabla \tilde{p} + \frac{1}{\lambda} \Delta \tilde{\mathbf{u}} \quad (2.34)$$

$$\nabla \tilde{\mathbf{u}} = 0 \quad (2.35)$$

$$\partial_t \tilde{\eta} = \tilde{v}_1 \quad (2.36)$$

$$\tilde{\mathbf{u}}_1 = \tilde{\mathbf{u}}_2|_{r=h} \quad (2.37)$$

$$\left( -\tilde{p}_1 \mathbb{I} + \left( \nabla \tilde{\mathbf{u}}_1 + (\nabla \tilde{\mathbf{u}}_1)^T \right) + \tilde{p}_2 \mathbb{I} - \frac{1}{\lambda} \left( \nabla \tilde{\mathbf{u}}_2 + (\nabla \tilde{\mathbf{u}}_2)^T \right) \right) \tilde{\mathbf{n}} = \tilde{\mathcal{C}} \tilde{\mathbf{n}} \quad (2.38)$$

We have obtained two set the of equations and boundary conditions described with three dimensional group: the Ohnesorge number  $Oh = \mu_1 / \sqrt{\rho_1 h_0 \gamma}$ , density ratio  $\rho = \rho_1 / \rho_2$  and the viscosity ratio  $\lambda = \mu_1 / \mu_2$ .

The numerical dispersion relation  $f(\omega, k, Oh, \rho \lambda) = 0$  obtained with the Chebyshev discretization incorporates all the limits and behaviors discussed above (see Appendix A for mathematical details). The presence of an external quiescent flow always slows down the instability. Increasing the outer viscosity or the outer density the instability is reduced (as shown in figure 2.8). If both viscosity of the thread and medium are take into account the cut-off wavenumber  $k_c h_0 = 1$  remains unvaried. The most amplified wavenumber  $k_m h_0$  is not a monotonous function of viscosity and density ratio and Ohnesorge number varying from  $k_m h_0 = 0$  and  $k_m h_0 = \sqrt{(2)}/2$ . In the limit case of a viscous thread in the void  $\lambda \rightarrow \infty$  and  $Oh \rightarrow \infty$  the most amplified wavenumber is  $k_m h_0 = 0$ , while in the opposite case of an inviscid thread in the void  $\rho \rightarrow \infty$  and  $Oh \rightarrow 0$  the most amplified wavenumber is  $k_m h_0 = \sqrt{2}/2$ .

The sketch 2.9 describes how the instability is effected by the variation of the dimensional group. Increasing the Ohnesorge number  $Oh$  of the liquid thread, namely increasing the viscous force with respect to the inertial and surface tension forces, the instability growth. While increasing the influence of the external flow, in other words decreasing the density ratio or the viscosity ratio, the instability is reduced.

## 2.3 Jet in a medium

If the aim is to analyze the dynamics and breakup of fluid jet into another immiscible fluid, considered to be unbounded, a significant difficulty arises. There is no parallel flow solution of a jet penetrating and entraining fluid around it. Even in the case of liquid jet in air, where both the viscosity and the density of the gas are usually negligible, the plug flow solution does not constitute a good approximation of the real flow. Two important factors have to be considered: (i) the continuity between the fluid velocity between inner

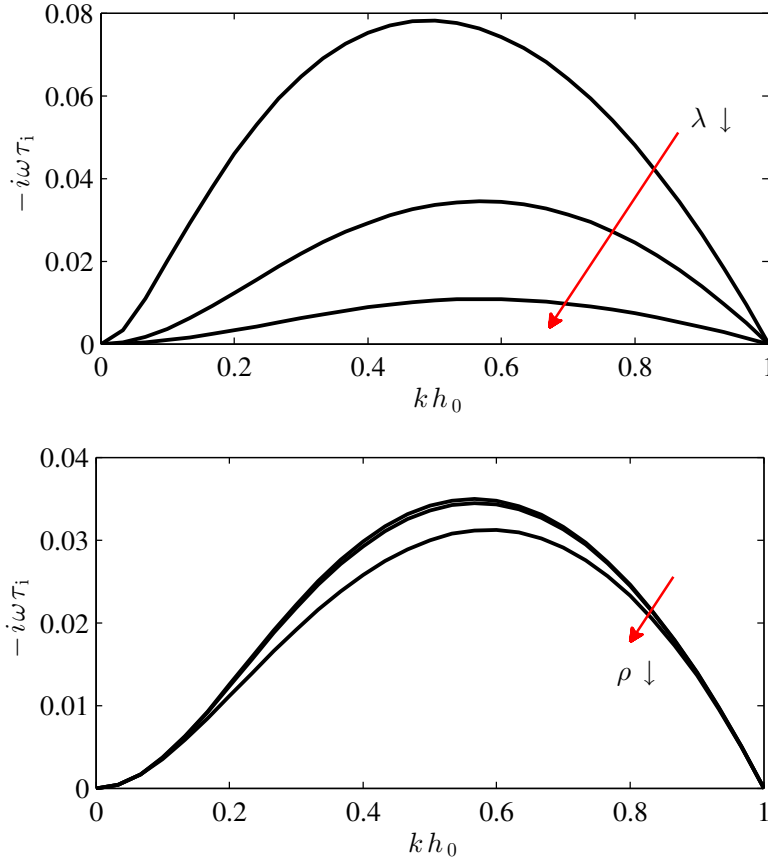


**Figure 2.8** – Dimensionless growth rate  $-i\omega\tau_i$  as function of the wavenumber  $kh_0$  for a liquid thread with  $Oh = 1$  immersed in a quiescent fluid. In the first picture  $\rho = 1$  and  $\lambda = \{0.1, 1, 10\}$ , in the second  $\lambda = 1$  and  $\rho = \{0.1, 1, 10\}$ .

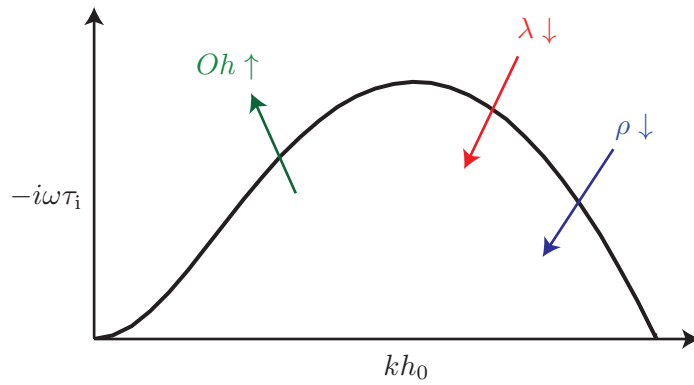


**Figure 2.9** – Sketch of how the instability of a liquid thread in a quiescent medium can grow or reduce varying the dimensional group  $Oh$ ,  $\rho$  and  $\lambda$ .

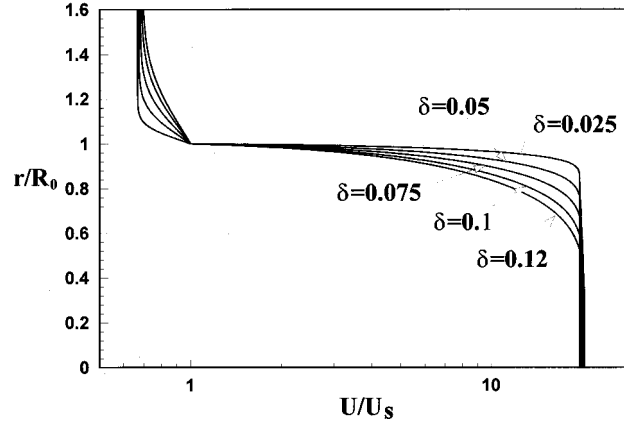


**Figure 2.10** – Family of velocity profile  $U/U_s$  for different value of the boundary layer thickness  $\delta$ , from Gordillo *et al.* (2001).

jet and outer fluid at the interface should be ensured, and (ii) the inner fluid exerts a force on the outer one through the shear stress and the continuity of stress that has to be ensured at the interface. The situation is even more complicated if the outer flow is also driven: it then acts as an external forcing that further deforms the jet.

In all these situations, the base flow solution evolves downstream and there are little analytical approaches to describe the flow. The accurate representation of the free interface as well as the steady solution of the governing equations become a significative challenge. Besides numerical simulation techniques for two-phase flows (see for instance the level-set approach described in dome detail in Appendix B), some attempts have been done to solve boundary layer like equations so as to identify a self-similar solution of the coaxial jets (Gordillo *et al.* (2001)), as shown in figure 2.10. In a situation of a viscous thread falling under gravity, an analytical solution can be obtained neglecting surface tension and a weakly non parallel stability analysis has revealed that the flow was globally stable, while it was locally unstable (Javadi, Eggers, Bonn, Habibi & Ribe (2013)). The physical reason lies in the kinematic gathering phenomenon (Eggers & Villermaux (2008)): as the filament thins down and accelerates, there is a permanent mismatch between the “grown-up” wavelengths and associated frequencies and the “coming up” stability properties of the flow.

There is one exception to this difficulty to analytically solve for the base flow, which is when the two streams are bounded by a pipe wall. In the latter case, a parallel flow solution with a cylindrical interface can be obtained, as discussed in detail in the next section.

## 2.4 Co-axial parallel jets in circular capillaries

The stability of viscous threads confined within a viscous outer liquid in a circular capillary has been exhaustively studied from Guillot *et al.* (2007), Guillot & Colin (2008) and Herrada *et al.* (2008) with the hypothesis of negligible inertia. The authors carried out a local stability analysis on the fully developed profile and they predict the transition from an absolute to a convective instability ruled by the capillary number and the degree of confinement. While Guillot *et al.* (2007) solves the problem using the lubrication approximation, Herrada *et al.* (2008) finds the dripping/jetting transition analytically. Although the lubrication approximation is expected to be less accurate, both methods present similar results, and once again the lubrication approximation presents the main advantage that the dispersion relation is explicit with respect to  $\omega$  and can be written in polynomial form.

In the following, the essential steps leading to the base flow and stability analysis with the lubrication approximation are explained.

### 2.4.1 Base flow

We consider a cylindrical capillary liquid jet of two incompressible and immiscible fluids in a pipe of radius  $R_2$ , as sketched in figure 2.11. The two fluids have different viscosity:  $\mu_1$  for the inner flow and  $\mu_2$  for the outer flow, different flow rate  $Q_1$  and  $Q_2$ . The two streams are chosen to be neutrally buoyant  $\rho_1 = \rho_2$ . The radius of the inner flow is assumed constant  $R_1$ . The gravity effect is neglected and the stability analysis is made in the limit of vanishing Reynolds number.

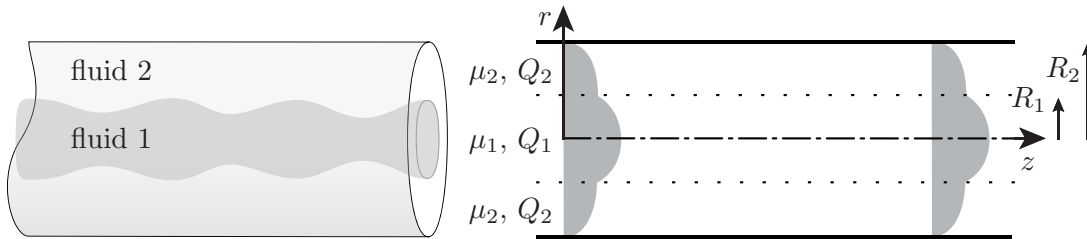


**Figure 2.11** – Sketch of the co-axial jet and notations used in this section.

The base flow is assumed steady, unidirectional and fully developed. The governing equations are the Stokes equations in axisymmetric coordinate. The boundary conditions

## 2.4. Co-axial parallel jets in circular capillaries

---

together with the interfacial conditions (2.3)-(2.5) allow to determine the velocity field:

$$\bar{u}_1(r) = -\frac{1}{4\mu_1}\partial_z\bar{p}(R_1^2 - r^2) - \frac{1}{4\mu_2}\partial_z\bar{p}(R_2^2 - h^2) \quad (2.39)$$

$$\bar{u}_2(r) = -\frac{1}{4\mu_2}\partial_z\bar{p}(R_2^2 - r^2) \quad (2.40)$$

and deduce the flow rates

$$Q_1 = -\frac{\pi}{8\mu_1}\partial_z\bar{p}R_1^4 - \frac{\pi}{4\mu_2}\partial_z\bar{p}R_1^2(R_2^2 - R_1^2) \quad (2.41)$$

$$Q_2 = -\frac{\pi}{8\mu_2}\partial_z\bar{p}(R_2^2 - R_1^2)^2 \quad (2.42)$$

Imposing the continuity of the velocity at the interface (2.39)-(2.40), the velocity interface  $U_{int}$  and the degree of confinement  $h = R_1/R_2$  are obtained:

$$U_{int} = \frac{2Q_2}{\pi R_2^2(1 - h^2)} \quad (2.43)$$

$$h = \frac{R_1}{R_2} = \sqrt{\frac{\lambda(1 + Q) - \sqrt{\lambda(\lambda + Q)}}{\lambda(2 + Q) - 1}} \quad (2.44)$$

where  $\lambda = \mu_1/\mu_2$  is the viscosity ratio and  $Q = Q_1/Q_2$  is the flow rate ratio.

In figure 2.12 we can observe the dependency of velocity profile  $\bar{U}_z(r)$  and interface position respect to the flow rates and viscosity ratio. For a fixed value of the flow rate ratio, increasing the viscosity ratio, the interface accelerates while the velocity of the central axis slows down. The interface position is shifted toward bigger value of  $h$ . Instead for a fixed value of the viscosity ratio, increasing the flow rate ratio, both the interface and centerline velocities accelerate and the interface position is shifted toward bigger value of  $h$ . This behavior is also observable in figure 2.13. Increasing the flow rate or the viscosity ratio the free interface moves toward the pipe wall.

### 2.4.2 Stability analysis

The stability analysis is performed using the lubrication approximation hypothesis (i.e. consider perturbation whose wavelength is large compared to the capillary radius  $R_2$ , which implies  $\partial_z \ll \partial_r$ ). Powers & Goldstein (1997) and Powers *et al.* (1998) demonstrated that the lubrication assumption captures qualitative and semi-quantative properties of non confined cylinders instabilities.

If we introduce small axisymmetric perturbations, the linearization of the governing

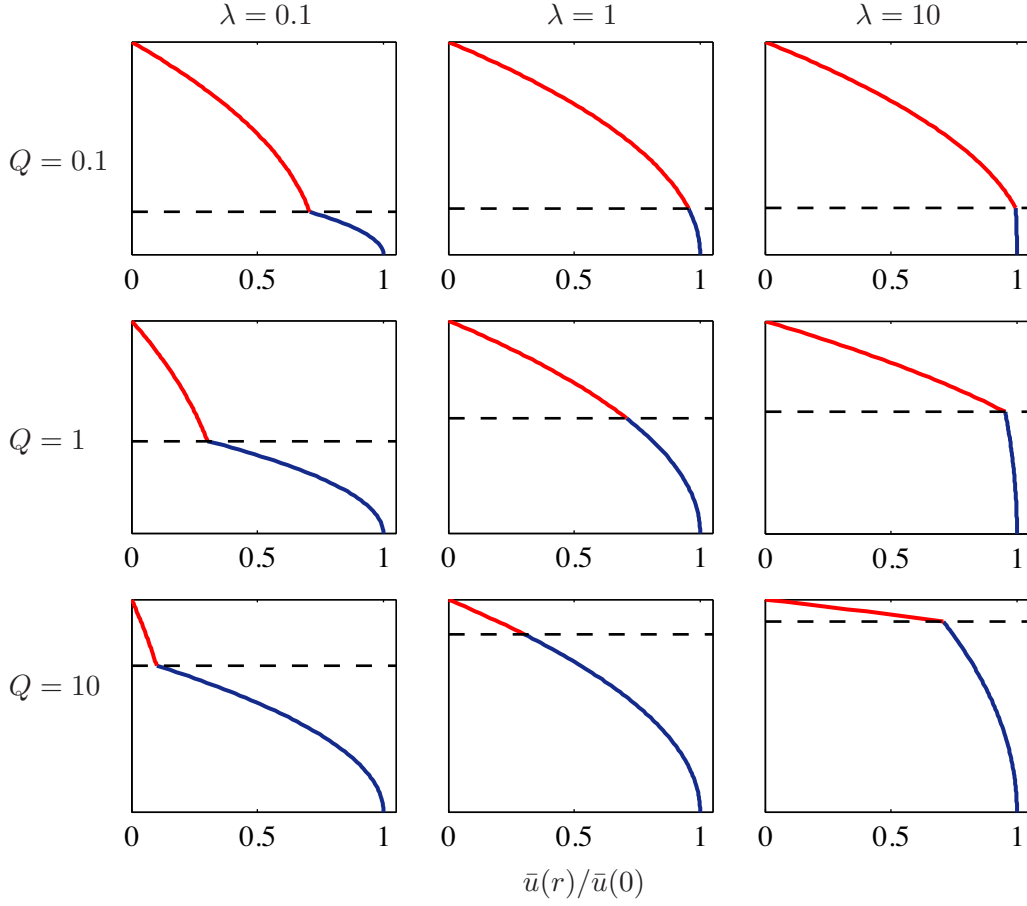


**Figure 2.12** – Velocity profile  $\bar{u}(r)$  normalized by the velocity on the axis  $\bar{u}(r = 0)$ . From left to right  $\lambda = \{0.1, 1, 10\}$  and from top to bottom  $Q = \{0.1, 1, 10\}$ . The red lines correspond to the velocity of the outer flow, while the blue lines to velocity of the inner flow

equation, using the lubrication approximation, gives:

$$\frac{1}{r} \partial_r (r v'_i) + \partial_z u'_i = 0 \quad (2.45)$$

$$0 = -\partial_r p'_i \quad (2.46)$$

$$0 = -\partial_z p'_i + \mu_i \frac{1}{r} \partial_r (r \partial_r u'_i). \quad (2.47)$$

Besides the no-slip conditions at the wall

$$\mathbf{u}'_2(r = R_2) = 0 \quad (2.48)$$

and the symmetry condition

$$\partial_r u'_1(r = 0) = 0, \quad v'_1(r = 0) = 0 \quad (2.49)$$

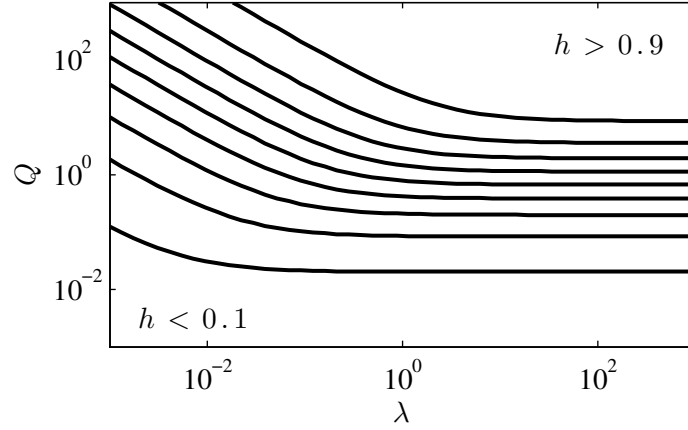


**Figure 2.13** – Contour of the interface position  $h$  as function of the viscosity ratio  $\lambda$  and flow rate ratio  $Q$ .

the flow has to satisfy also the interface boundary conditions: continuity of the velocity, stress balance and kinematic equation.

The continuity of the velocity at the interface gives:

$$\mathbf{u}'_1 \Big|_{r=\eta} = \mathbf{u}'_2 \Big|_{r=\eta} \quad (2.50)$$

Since, a priori, we don't know the position of the perturbed interface, we can expand the interfacial condition in Taylor's series around  $r = R_1$ , the unperturbed interface, to extract the quantities in the unperturbed location

$$\mathbf{u}'_i \Big|_{r=\eta} = \mathbf{u}'_i \Big|_{r=R_1} + \eta \frac{\partial \bar{\mathbf{u}}_i}{\partial r} \Big|_{r=R_1} \quad (2.51)$$

With the flattening, we can rewrite the continuity of the velocity on the unperturbed interface as

$$\mathbf{u}'_1 + \eta \partial_r \bar{\mathbf{u}}_1 \Big|_{r=R_1} = \mathbf{u}'_2 + \eta \partial_r \bar{\mathbf{u}}_2 \Big|_{r=R_1} \quad (2.52)$$

The continuity of the tangential stress at the interface gives:

$$(\mu_1 \partial_r u_1 - \mu_2 \partial_r u_2) \Big|_{r=R_1} = 0 \quad (2.53)$$

while the jump of the normal stress can be written as

$$(-p_1 + p_2) \Big|_{r=R_1} = \gamma \left( \frac{\eta}{R_1^2} + \partial_{zz} \eta \right). \quad (2.54)$$

The last interfacial condition to set is the perturbed kinematic equation

$$\partial_t \eta = v_i(R_1) - U_{int} \partial_z \eta \quad (2.55)$$

In order to carry out the stability of the co-axial flow, the perturbations are sought in normal mode decomposition:

$$\mathbf{u}'_i(r, z, t) = \hat{\mathbf{u}}_i(r) e^{i(kz - \omega t)} \quad (2.56)$$

$$p'_i(r, z, t) = \hat{p}_i(r) e^{i(kz - \omega t)} \quad (2.57)$$

$$\eta(z, t) = \hat{\eta} e^{i(kz - \omega t)} \quad (2.58)$$

From the  $r$ -momentum (2.46), it is possible to deduce that  $\hat{p}_i(r) = \hat{p}_i$  is a constant function with respect to  $r$ , while, integrating the continuity equation (2.45) and the  $z$ -momentum (2.47) it is possible to find an expression for  $\hat{\mathbf{u}}_i(r)$ :

$$\hat{u}_i(r) = \frac{ik}{4\mu_i} (\hat{p}_i r^2 + C_i \log r + D_i) \quad (2.59)$$

$$\hat{v}_i(r) = \frac{k^2}{4\mu_i} \left( \frac{\hat{p}_i r^3}{4} + \frac{C_i}{2} \left( r \log r - \frac{r}{2} \right) + \frac{D_i r}{2} + \frac{E_i}{r} \right) \quad (2.60)$$

where  $C_i, D_i, E_i$  are constant of integrations (for the symmetry condition  $C_1 = E_1 = 0$ ).

The boundary conditions can be written in matrix form:

$$A\phi = 0 \quad (2.61)$$

where  $\phi = (\hat{p}_1, D_1, \hat{p}_2, C_2, D_2, E_2, \hat{\eta})$  and the matrix  $A$  is

$$A = \begin{pmatrix} 0 & 0 & R_2^2 & \log R_2 & 1 & 0 & 0 \\ 0 & 0 & \frac{R_2^3}{4} & \frac{2R_2 \log R_2 - R_2}{4} & \frac{R_2}{2} & \frac{1}{R_2} & 0 \\ R_1^2 & 1 & -\lambda R_1^2 & -\lambda \log R_1 & -\lambda & 0 & 2i(\lambda - 1) \frac{R_1}{k} \partial_z \bar{p} \\ R_1^3 & 2R_1 & -\lambda R_1^3 & -\lambda R_1(2 \log R_1 - 1) & -2\lambda R_1 & -\frac{4\lambda}{R_1} & 0 \\ -\frac{k^2}{16\mu_1} R_1^3 & -\frac{k^2 R_1}{8\mu_1} & 0 & 0 & 0 & 0 & i(kU_{int} - \omega) \\ 2R_1 & 0 & -2R_1 & -\frac{1}{R_1} & 0 & 0 & 0 \\ -1 & 0 & 1 & 0 & 0 & 0 & -\gamma \left( \frac{1}{R_1^2} - k^2 \right) \end{pmatrix} \quad (2.62)$$



### 2.4.3 Temporal stability analysis and dispersion relation

The system has non-trivial solution if  $\det A = 0$ , and the following dispersion relation is founded:

$$\omega = U_{int} Jk + i \frac{\gamma}{\mu_2 R_2} G(R_2^2 k^2 - R_1^4 k^4) \quad (2.63)$$

where the terms  $J = J(h, \lambda)$  and  $G = G(h, \lambda)$  are positive function of the viscosity ratio and interface position

$$\begin{aligned} J(h, \lambda) &= \frac{\lambda h^2 - h^2 - \lambda}{\lambda h^4 - \lambda - h^4} \\ G(h, \lambda) &= \frac{(-4 \log h + 4 \lambda \log h - 4 \lambda + 3) h^5 + 4(2 \lambda - 1) h^3 + (1 - 4 \lambda \log h - 4 \lambda) h}{16(h^4(1 - \lambda) + \lambda)} \end{aligned} \quad (2.64)$$

If we adimensionalize the wave frequency with the characteristic viscous timescale  $\tilde{\omega} = \omega \frac{\mu_2 R_2}{\gamma} = \omega \tau_v$  and the wavenumber with the capillary radius  $\tilde{k} = k R_2$ , the above dispersion relation (2.63) becomes:

$$\tilde{\omega} = Ca J \tilde{k} + i G (\tilde{k}^2 - h^2 \tilde{k}^4) \quad (2.65)$$

where the Capillary number is defined as  $Ca = \mu_2 U_{int} / \gamma$ .

For a co-axial jet, in the limit of vanishing Reynolds number, the stability is described by three dimensionless group: the Capillary number  $Ca$ , the interface position  $h$  and the viscosity ratio  $\lambda$ . The comparison of the lubricated dispersion relation with the exact solution found by Herrada *et al.* (2008) gives a good agreement, as shown in figure 2.14. With the dimensionless group proposed, the cut-off is always  $\tilde{k}_c = \frac{1}{h}$  and it gives an information about the confinement. The frequency  $\tilde{\omega}_r = Ca J \tilde{k}$  has a linear dependency on the wavenumber, while the growth rate  $\tilde{\omega}_i = G(\tilde{k}^2 - h^2 \tilde{k}^4)$  describes the surface tension effects. More precisely  $\tilde{k}^2$  is related to the curvature in the cross section, and  $\tilde{k}^4$  is related to the curvature in the flow direction. While the curvature in the axial curvature promotes the jet regime, the radial curvature drives the breakup.

### 2.4.4 Spatio-temporal stability analysis and convective/absolute regime

The determination of the saddle point of the spatio-temporal analysis (2.65) lead to the absolute wavenumber

$$k_0 = \left( \pm \sqrt{\frac{9 + 3\sqrt{7}}{24}} - i \sqrt{\frac{-1 + \sqrt{7}}{24}} \right) \frac{1}{k_c} \quad (2.66)$$

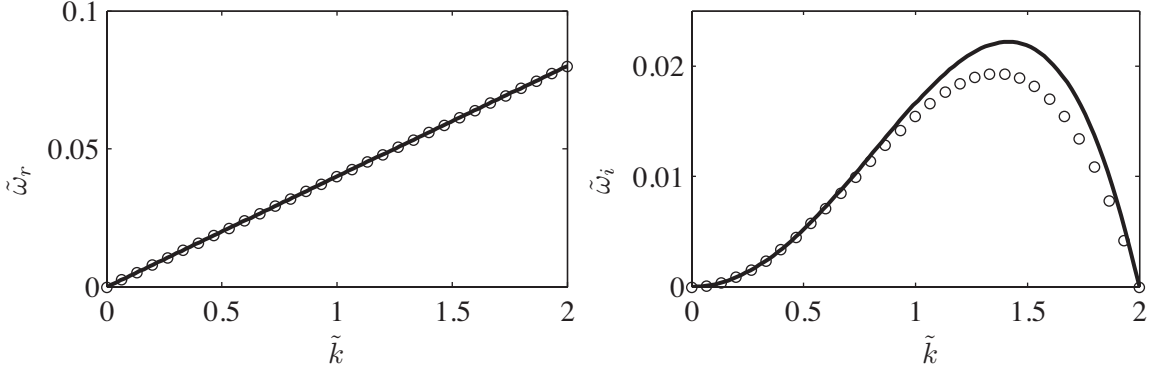


**Figure 2.14** – Dimensionless dispersion relation for a co-axial jet with  $h = 0.5$ ,  $\lambda = 1$  and  $Ca = 1/25$ . Comparison between lubrication approximation (lines) (Guillot *et al.* (2007)) and exact solution (circles) (Herrada *et al.* (2008)).

with absolute wave frequency

$$\begin{aligned} \omega_0 = & -\frac{hJCa}{12} \left( -3\sqrt{6+2\sqrt{7}} + i\sqrt{-6+6\sqrt{7}} \right) \\ & -\frac{h^2G}{36} \left( \frac{\sqrt{6+2\sqrt{7}}}{4} \left( -6+5h^4+\sqrt{7}h^4 \right) \sqrt{-6+6\sqrt{7}} + i(-3+h^4)(5+\sqrt{7}) \right) \end{aligned}$$

We can find the group velocity  $v_g^\pm$  of the perturbation imposing

$$\frac{\partial \omega_i}{\partial k_r} = 0, \quad v_g^\pm = \frac{\omega_i}{k_i}, \quad v_g^\pm = \frac{\partial \omega_i}{\partial k_i} \quad (2.67)$$

this criterion leads to

$$v_g^\pm = CaJ \pm \frac{G}{h^2} \left( \frac{\sqrt{7}+5}{12k_c(z)^2} - \frac{\sqrt{7}+5}{36k_c(z)^4} \right) \sqrt{\frac{24k_c(z)^2}{\sqrt{7}-1}} \quad (2.68)$$

The determination of the dripping/jetting regime transition shows that a co-axial jet has enough energy to overcome the surface energy and maintain the jetting regime when

$$Ca > \frac{G(h, \lambda)}{hJ(h, \lambda)} \left( 3 - h^2 \right) \frac{5 + \sqrt{7}}{36} \sqrt{\frac{24}{\sqrt{7} - 1}} \quad (2.69)$$

Below the critical value of the Capillary number the jet is absolutely unstable, above convectively unstable. The function  $v_g^-(Ca, h, \lambda) = 0$  is plotted in the  $(h, Ca)$ -plane for different values of viscosity ratio, as shown in figure 2.15. If the viscosity ratio is increased, the convective region increases at expense of the absolute region. Instead, for

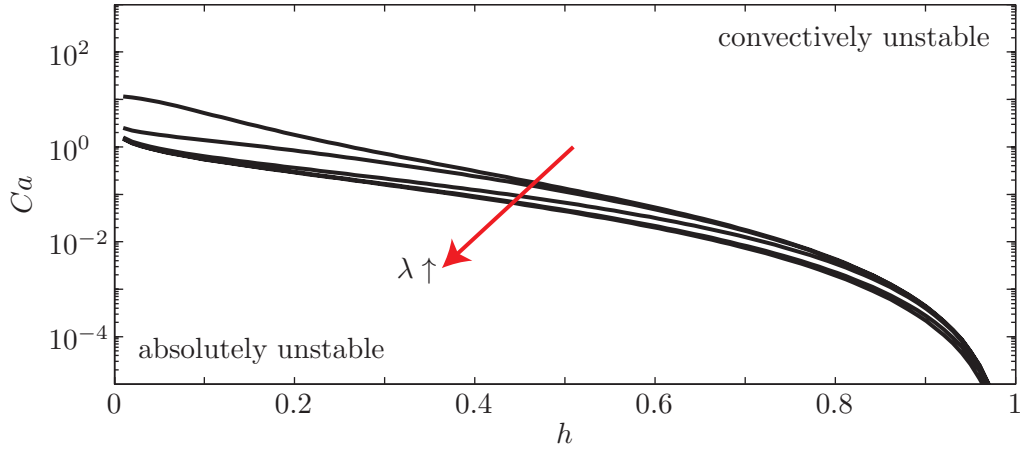


**Figure 2.15** – Phase diagram of the instability in the  $(h, Ca)$ -plane for different value of viscosity ratio  $\lambda = \{0.01, 0.1, 1, 10, 100\}$ , as previously found by Guillot *et al.* (2007).

the same value of the viscosity ratio, the absolute regime is promoted if the confinement or the Capillary number are decreased.

The link between the A/C properties and global modes of a model finite length parallel jet with boundary conditions and the real spatial developing flow will be explored in chapter 3.

### 2.4.5 Exact dispersion relation

The exact and explicit dispersion relation can be found analytically (for details Herrada *et al.* (2008)). In the following, the essential steps leading to the exact solution are explained.

The perturbed continuity equation and the perturbed Stokes equation are sought in normal mode form

$$ik\hat{u}_i + \frac{1}{r} \frac{\partial}{\partial r} (r\hat{v}_i) = 0 \quad (2.70)$$

$$0 = -ik\hat{p}_i + \mu_i \left( \frac{1}{r} \frac{\partial}{\partial r} \left( r \frac{\partial \hat{u}_i}{\partial r} \right) - k^2 \hat{u}_i \right) \quad (2.71)$$

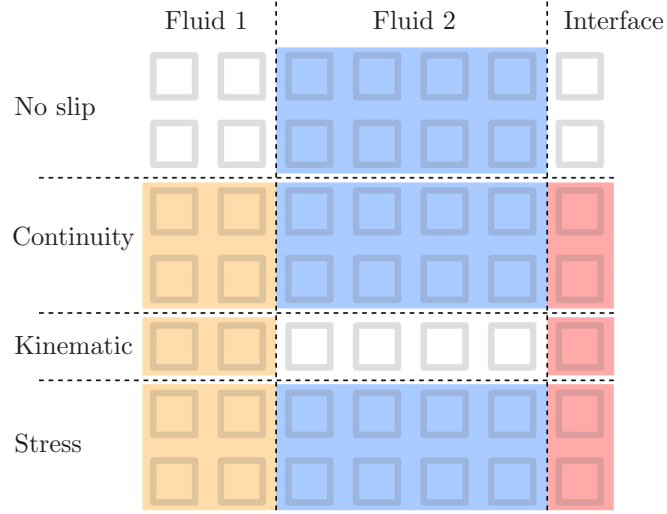
$$0 = -\frac{\partial \hat{p}_i}{\partial r} + \mu_i \left( \frac{\partial}{\partial r} \left( \frac{1}{r} \frac{\partial}{\partial r} (r\hat{v}_i) \right) - k^2 \hat{v}_i \right) \quad (2.72)$$

The system equations (2.70)-(2.72) can be solved introducing the modified stream-functions  $\Psi_i$

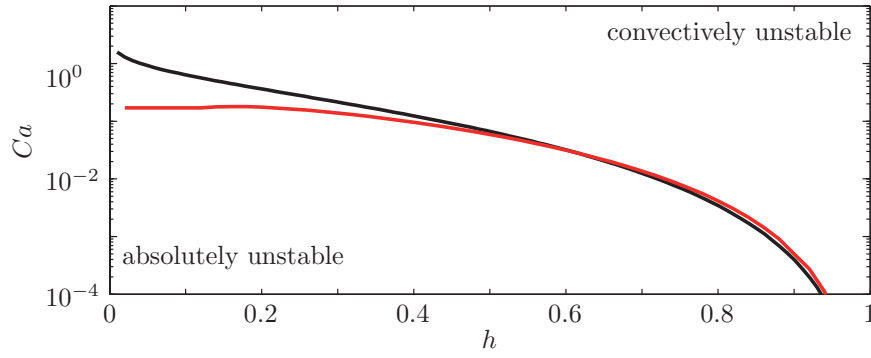
$$\hat{u}_i = \frac{1}{r} \frac{d}{dr} (r^2 \Psi_i), \quad \hat{v}_i = -ikr \Psi_i \quad (2.73)$$



## 2.4. Co-axial parallel jets in circular capillaries






**Figure 2.16** – Structure of matrix  $A$  for local stability analysis.



**Figure 2.17** – Phase diagram of the instability in the  $(h, Ca)$ -plane for  $\lambda = 1$ . Comparison between the lubrication approximation (black line) and exact solution (red line).

latter case, we have identified the A/C transition as function of the operating parameters: degree of confinement, viscosity ratio and Capillary number.

	Inert external medium	Unbounded external medium	Bounded external medium
			
Threads	$\mu_1 = 0$ $\rho_1 \neq 0$ (1.4.1)	$\mu_1 = 0, \mu_2 = 0$ $\rho_1 \neq 0, \rho_2 \neq 0$ (2.2.1)	
		$\mu_1 = 0, \mu_2 \neq 0$ $\rho_1 \neq 0, \rho_2 \neq 0$ (2.2.2)	
	$\mu_1 \neq 0$ $\rho_1 = 0$ (1.4.2)	$\mu_1 \neq 0, \mu_2 \neq 0$ $\rho_1 = 0, \rho_2 = 0$ (2.2.3)*	
	$\mu_1 \neq 0$ $\rho_1 \neq 0$ (1.4.3)	$\mu_1 \neq 0, \mu_2 \neq 0$ $\rho_1 \neq 0, \rho_2 \neq 0$ (2.2.4)**	
Jets	$\mu_1 = 0$ $\rho_1 \neq 0$ (1.5.1)	Case-dependent spatially developing flow	$\mu_1 \neq 0, \mu_2 \neq 0$ $\rho_1 = 0, \rho_2 = 0$ (2.4.2) <sup>†</sup>
	$\mu_1 \neq 0$ $\rho_1 = 0$ (1.5.2)		$\mu_1 \neq 0, \mu_2 \neq 0$ $\rho_1 = 0, \rho_2 = 0$ (2.4.4) <sup>‡</sup>
	$\mu_1 \neq 0$ $\rho_1 \neq 0$ (1.5.3)		$\mu_1 \neq 0, \mu_2 \neq 0$ $\rho_1 \neq 0, \rho_2 \neq 0$ (Appendix A)

**Table 2.1** – Different jets and threads and their viscous and inviscid limits discussed in sections 1 and 2. In all but the cases labelled by an \*, a long-wave approximation can be proposed. In addition, no explicit analytical expression can be obtained in case labelled by a \*\*. In the case labelled by <sup>†</sup>, a lubrication approximation is proposed, while in the case labelled by <sup>‡</sup>, the full Stokes equations are solved in each domain.

## 3 Global stability analysis of co-axial jets

In this chapter we consider the flow in a co-axial injector and we investigate the effect of the entry region by means of a global stability analysis. The chapter is organized as follows. Sec. § 3.1 introduces the problem and the state of art, Sec. § 3.2 describes the geometry, the governing equations and the numerical methods. In Sec. § 3.3 we validate our mathematical tools in special case of a parallel flow. In Sec. § 3.4 we investigate the effect of fluids viscosities, flow rates and surface tension on the flow spatial evolution of the inner phase jet. The stability proprieties of the base flow is then investigated by a global stability analysis of the two dimensional axisymmetric flow in Sec. § 3.5.

**Paper:** *On the influence of the entry region in a coflowing injector device*

## On the influence of the entry region in a coflowing injector device

L. Augello and A. Fani and F. Gallaire

LFMI, École Polytechnique Fédérale de Lausanne, CH-1015 Lausanne, Switzerland

Under consideration for publication in J. Fluid Mech.

**Key words:** instabilities, co-axial flow, drop formation

### 3.1 Introduction

The production of droplets is of fundamental importance in industrial liquid-liquid contact processes, such as solvent extraction, ink jet printing, spray atomization, emulsification process, and polymer extrusion, to name a few (see Stone (1994) and Eggers & Villermaux (2008)). In microfluidic applications with two immiscible fluids, droplets are usually produced through passive techniques, where the flow field deform the interface in order to promote interfacial instabilities which leads to drop formation (see for instance Baroud, Gallaire & Dangla (2010) and the references therein).

One of the simplest possible device consists in a co-axial injector, where the disperse phase is injected in a outer carrier fluid which flows in a cylindrical tube. Cramer *et al.* (2004) carried out experiments on a co-flowing device with a needle placed inside a rectangular flow cell. They showed that the breakup of the liquid stream into droplets can be classified in two regimes: dripping, in which droplets pinch off near the capillary tube's tip, and jetting in which droplets pinch off from an extended thread downstream of the needle tip. The first regime is observed for small values of the inner phase flow rate  $Q_1$ , where the capillary force dominates. As  $Q_1$  is increased (keeping the external phase flow rate  $Q_2$  constant), viscous and inertial forces becomes comparable to the capillary one and a transition to the jetting regime occurs. The transition depends also on the two fluids viscosities and on the interfacial tension.

Guillot and coworkers (Guillot *et al.* (2007); Guillot & Colin (2008)) studied the stability of viscous jet confined within a viscous outer liquid in a microchannel by carrying out a local stability analysis of the developed flow profile (see 3.1(b)), using a lubrication approximation and neglecting the inertial terms. They interpreted the transition from dripping to jetting as a transition from an absolute to a convective instability, a concept widely applied in instabilities of shear flows and wakes (see Huerre & Monkewitz (1990) for details). In an absolutely unstable system perturbations can grow and withstand the



mean advection, leading to self-sustained oscillations. In contrast, convectively unstable systems do not display intrinsic dynamics and essentially behave as amplifiers: external perturbations are amplified while propagating through the system. In co-axial devices an absolutely unstable configuration is related to a self-sustained production of droplets (dripping), while a convectively unstable flow is expected to result in droplets which form at a finite distance downstream (jetting), only after the instability could grow. The authors could identify a critical value of the capillary number  $Ca$  as a function of the flow parameters such as the phases viscosities and the interface position ( $H_{out}$  in figure 3.1(b)). A good agreement was found between the theoretical critical value and the capillary number at which transition from dripping to jetting is observed in experiments, confirming that the two transitions are related. The lubrication approach fails for low values of the jet radius  $H_{out}$ , in that case the complete set of equations must be considered in order to have a good agreement with experiments, as shown in Herrada *et al.* (2008).

The local analysis carried out in the previous works can be applied to parallel or slowly spatially evolving flows. Nonetheless, the flow is expected to vary rapidly from a bi-Poiseuille velocity profile close to the nozzle to the fully developed one. In analogy with single phase pipe flow, the entry length is expected to scale like the pipe radius in the low Reynolds limit. In addition, the nozzle radius  $H_{in}$  can be significantly different from the developed jet radius  $H_{out}$ , leading to an interface that varies along the stream-wise direction. To take into account non-parallel effects, a global stability analysis must be carried out. The studies using global methods have until now been concentrated on wakes behind solid obstacles and detached flows (see Theofilis (2011)), but mainly of single phase flows. A global stability analysis of the two dimensional wake of immiscible flows has been carried out by Tammisola *et al.* (2012), where they have observed a counterintuitive destabilizing effect of the surface tension. Gordillo *et al.* (2013) studied the dripping to jetting transition of two coaxial streams in the so called tip-streaming regime, where the inner phase presents a cone-jet structure. They carried out a global stability analysis of the cone-jet, by using a slender body approximation, and they have observed that regime where uniformly sized droplets are produced is associated to a globally unstable flow.

In this study we consider the flow in a co-axial injector and we investigate the effect of the entry region by means of a global stability analysis. The paper is organized as follows. Sec. 3.2 describes the geometry, the governing equations and the numerical methods. In Sec. 3.4 we investigate the effect of fluids viscosities, flow rates and surface tension on the flow spatial evolution of the inner phase jet. In addition we varied the nozzle diameter, in order to assess how the geometry influence the drop formation. The stability properties of the base flow is then investigated by a global stability analysis of the two dimensional axisymmetric flow in Sec. 3.5.

### 3.2 Problem description

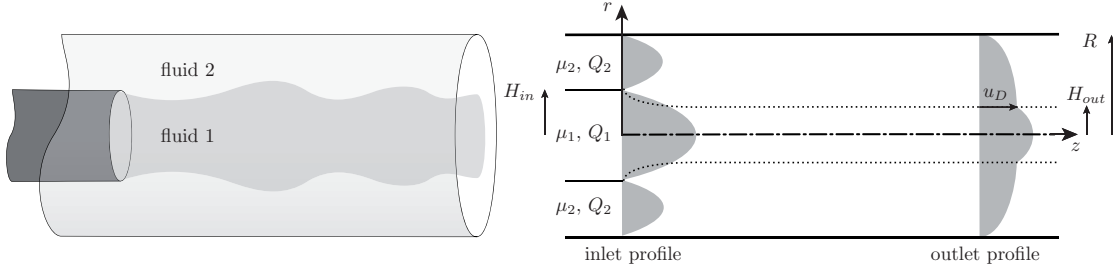


**Figure 3.1** – Flow domain and notations used in the text. On the left a 3D sketch of the core-annular flow, on the right a 2D view of the geometry. The dash-dot ( $- \cdot$ ) line is the axisymmetric axis, the dotted line ( $\cdot \cdot$ ) is the interface, while the continuous line is the pipe wall at  $r = R$ . The inner fluid, with viscosity  $\mu_1$  and flow rate  $Q_1$ , flows in an immiscible fluid with viscosity  $\mu_2$  and flow rate  $Q_2$ .

We consider the flow of two incompressible and immiscible fluids in a pipe of radius  $R$ . One of the fluids is injected by using a nozzle of radius  $H_{in}$  as sketched in figure 3.1. The two fluids have the same density  $\rho$  but different viscosity:  $\mu_1$  for the inner flow and  $\mu_2$  for the outer. The inlet velocity of respective stream has a Poiseuille profile with flow rate  $Q_1$  for the inner flow, and  $Q_2$  for the outer. The interface evolves downstream until it reaches the fully developed position  $H_{out}$  and velocity  $u_D$ . In the following, we neglect the inertial effects, as well as gravity, compared to the capillary forces  $\rho u_D^2 \ll \gamma/R$ , where  $\gamma$  is the surface tension.

The governing equations for the fluids are the incompressible Stokes equations in axisymmetric coordinates  $(r, z)$ , made dimensionless with the external pipe radius  $R$ , the fully developed velocity  $u_D$  and the outer viscosity  $\mu_2$ . The problem is characterized by the three dimensionless parameters:

$$Ca = \frac{\mu_2 u_D}{\gamma}, \quad \lambda = \frac{\mu_1}{\mu_2}, \quad Q = \frac{Q_1}{Q_2} \quad (3.1)$$

where  $Ca$  is the capillary number,  $\lambda$  the viscosity ratio and  $Q$  is the flow rate ratio.

#### 3.2.1 Steady solution

In order to carry out a stability analysis, we first need to compute the steady solution. The base flow is computed by solving a single Stokes equation in the full domain coupled with the level set function that allow to distinguish the two fluid (see Olsson & Kreiss (2005)-Olsson, Kreiss & Zahedi (2007) for details on the method). The varying fluid properties, as viscosity, can be expressed as function of the level-set. The advantage of this method is that we can perform numerical simulation with low capillary number  $Ca$

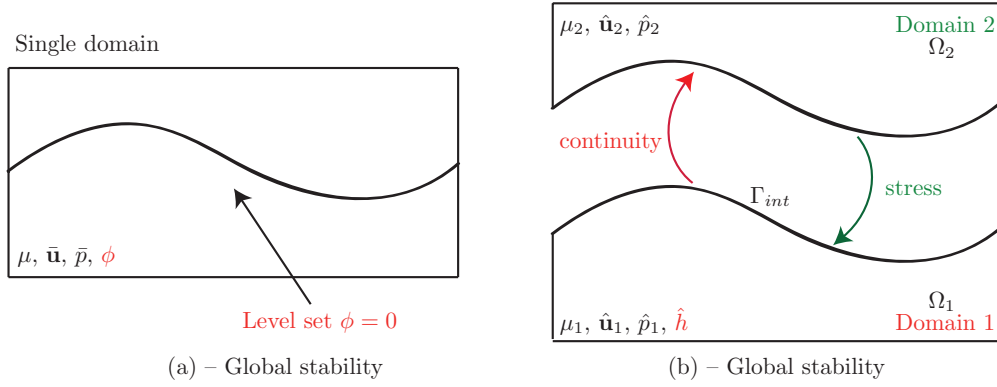


**Figure 3.2** – Base flow (a): the two fluid are computed in the same fixed grid by implementing the Stokes equation of a single velocity field in the full domain and the two layers are distinguished by a presence of the level-set function. Perturbed flow (b): the two fluid are computed in two different grid by implementing the Stokes equations of two velocity fields with the addition of the linearized boundary conditions at the interface.

without having to parametrize the surface curvature (fig 3.2a). The governing equations become:

$$0 = \nabla \cdot \left[ -\bar{p}\mathbb{I} + \mu \left( \nabla \bar{\mathbf{u}} + (\nabla \bar{\mathbf{u}})^T \right) \right] + \frac{1}{C_a} \bar{\mathcal{C}} \bar{\mathbf{n}} \delta \quad (3.2)$$

$$\bar{\mathbf{u}} \cdot \nabla \phi = \nabla \cdot (D \nabla \phi) \quad (3.3)$$

$$\nabla \cdot \bar{\mathbf{u}} = 0 \quad (3.4)$$

where  $\mu = \mu(\phi)$  denotes the viscosity, which is a function of the level set function  $\phi$ :

$$\mu = 1 + (\lambda - 1) \mathcal{H}_e(\phi) \quad (3.5)$$

where  $\mathcal{H}_e(\phi)$  is the Heaviside function with continuous second derivative and transition thickness  $e$  which depends on the mesh size. The capillary effects are modelled by the last term on the right-hand side of equation (3.2)  $\frac{1}{C_a} \bar{\mathcal{C}} \bar{\mathbf{n}} \delta$ . The geometric properties of the interface are easily determined from the level-set function. The unit normal vector  $\bar{\mathbf{n}}$  and the surface curvature  $\bar{\mathcal{C}}$  are respectively given by

$$\bar{\mathbf{n}} = \frac{\nabla \phi}{|\nabla \phi|} \quad (3.6)$$

$$\bar{\mathcal{C}} = -\nabla \cdot \bar{\mathbf{n}} \quad (3.7)$$

The capillary force is localized at the interface by the Dirac delta function  $\delta$ , such that the level set variable  $\phi = 0$ .

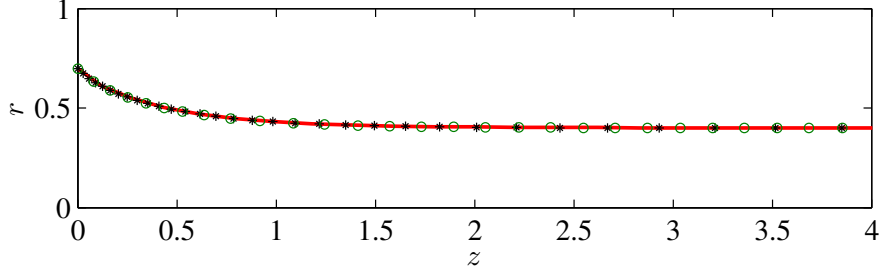


**Figure 3.3** – Comparison of the interface position found with the level-set method (red line), boundary element method (\* marker) and VOF description (o marker) for a co-axial flow. Simulations done for  $H_{in} = 0.7$ ,  $H_{out} = 0.4$ ,  $\lambda = 5$  and  $Ca = \infty$ . Flow rate  $Q_1 = 0.5122$  and  $Q_2 = 1.3195$ .

An important aspect of the level-set method is the treatment of the artificial diffusion  $D$  required for numerical stability. In our model we used a streamline diffusion (Streamline Upwind Petrov-Galerkin method with tuning parameter  $\delta_{sd} = 0.25$  Hughes & Mallet (1986)).

The base flow simulations were carried out with COMSOL *Multiphysics* 4.2 a with P2-P1 discretization for the fluid and a cubic discretization for  $\phi$ . The non linear base state is obtained with a Newton method where the linear systems are solved with the direct solver PARDISO (Schenk, Bollhöfer & Römer (2008)).

The base flow computation, based on the level set method, is validated against data obtained with two other different numerical approaches. The first method used is the boundary element method (BEM), a so-called meshless interface tracking method where only the boundaries are discretized. Details on the method can be found in Pozrikidis (1992). In addition, the base flow is also obtained by using a Volume Of Fluid (VOF), along with a finite volume spatial discretization, implemented in the open source code *Gerris Flow Solver* (Popinet (2003)). Fig. 3.3 shows the interface location obtained with the three methods for a flow with the following parameters: inner pipe radius  $H_{in} = 0.7$ , viscosity ratio  $\lambda = 5$ , inner flow rate  $Q_1 = 0.5122$ , outer flow rate  $Q_2 = 1.3195$ , fully developed interface radius  $H_{out} = 0.4$  and a capillary number  $Ca = \infty$ . We can see that the level set method is in remarkable agreement with the other two. For the base flow calculation, the level set approach is preferred because the Newton method allows to find the steady unstable solutions.

### 3.2.2 Global stability analysis

The stability proprieties of a steady base-flow can be assessed though a linear stability analysis by considering the time evolution of a small perturbation sought in term of normal mode. Nonetheless the linearization of the level set formulation can be tricky,

due to the presence of the Dirac delta function.

In this study we preferred to use an alternative approach for the stability problem formulation. The problem is formulated in two different grids (one for each fluids) that can interact through the boundary conditions at the interface, i.e. continuity of the velocity and stress jump (figure 3.2b). The flow variables are the velocity  $\mathbf{U}_i = u_i \mathbf{e}_z + v_i \mathbf{e}_r$ , the pressure  $P_i$  and the interface position  $H$ , where the index  $i = \{1, 2\}$  denotes respectively the inner and the outer flow. The nonlinear governing equations for the two fluids are:

$$0 = \nabla \cdot \sigma_i \quad (3.8)$$

$$\nabla \cdot \mathbf{U}_i = 0 \quad (3.9)$$

$$\partial_t H = -\mathbf{U}_1 \nabla H \quad (3.10)$$

where  $\sigma_i = -P_i \mathbb{I} + \mu_i (\nabla \mathbf{U}_i + \nabla \mathbf{U}_i^T)$  is the stress tensor. Note that  $\mu_i$  here is  $\lambda$  for  $i = 1$  and 1 for  $i = 2$ . Equation (3.10) is the kinematic equation, defined only on the interface boundary, which describe the motion of the interface (see Prosperetti & Tryggvason (2007)). The unit vector  $\mathbf{n}$  normal to the interface pointing towards the outer fluid, the tangential vector  $\mathbf{t}$  and the mean curvature  $\mathcal{C}$  can be written as:

$$\mathbf{n} = \frac{(1, -\partial_z H)}{(1 + (\partial_z H)^2)^{1/2}} \quad (3.11)$$

$$\mathbf{t} = \frac{(\partial_z H, 1)}{(1 + (\partial_z H)^2)^{1/2}} \quad (3.12)$$

$$\mathcal{C} = -\nabla \cdot \mathbf{n} \quad (3.13)$$

In order to carry out a global stability analysis we divide the flow variables  $\mathbf{Q} = (\mathbf{U}, P, H)$  into one steady state  $\bar{\mathbf{q}} = (\bar{\mathbf{u}}, \bar{p}, \bar{h})$  and one small amplitude time-varying perturbation  $\hat{\mathbf{q}} = (\hat{\mathbf{u}}, \hat{p}, \hat{h})$ :

$$\mathbf{U}(r, z, t) = \bar{\mathbf{u}}(r, z) + \varepsilon \hat{\mathbf{u}}(r, z) \exp(-i\omega t) \quad (3.14)$$

$$P(r, z, t) = \bar{p}(r, z) + \varepsilon \hat{p}(r, z) \exp(-i\omega t) \quad (3.15)$$

$$H(z, t) = \bar{h}(z) + \varepsilon \hat{h}(z) \exp(-i\omega t) \quad (3.16)$$

where  $\omega \in \mathbb{C}$  is the complex wave frequency.

By injecting the flow decomposition into the governing equations and linearizing, we

obtain a set of equations which describe the linear evolution of the perturbations. Note that the base flow and the linear stability computations are carried out through two different methods (see Fig. 3.2 for a sketch of the two different approaches), thus some preliminary steps need to be performed to do the stability analysis.

The computational domains are built using the level set interface position. Nonetheless, the obtained interface is characterized by small numerical oscillation caused by the interpolation of the isoline  $\Phi = 0$ . Therefore a fitting procedure was devised where an optimal fitting spline is computed by minimising an error indicator. Once the interface is discretized, the base flow can be easily computed in the two separated domains and the error due to the interface spline can be computed as  $\int_{\Gamma_i} \bar{\mathbf{u}} \cdot \bar{\mathbf{n}} d\Gamma / \int_{\Gamma_i} d\Gamma$ . The baseflow in the separated domains is computed by using a finite-element method, with cubic elements  $P3$  for the velocities and quadratic elements  $P2$  for the pressure, which is an higher order version of the standard Taylor-Hood elements (see Brezzi & Falk (1991) for details).

The governing equations for the linear evolution of the perturbations can be written as:

$$0 = \nabla \cdot \hat{\sigma}_i \quad (3.17)$$

$$\nabla \cdot \hat{\mathbf{u}}_i = 0 \quad (3.18)$$

$$-i\omega \hat{h} = -\bar{u}_1 \frac{\partial \hat{h}}{\partial z} - \left( \hat{u}_1 + \hat{h} \frac{\partial \bar{u}_1}{\partial r} \right) \frac{\partial \bar{h}}{\partial z} + \hat{v}_1 + \hat{h} \frac{\partial \bar{v}_1}{\partial r} \quad (3.19)$$

where  $\hat{\sigma}_i = -\hat{p}_i \mathbb{I} + \mu_i \left( \nabla \hat{\mathbf{u}}_i + (\nabla \hat{\mathbf{u}}_i)^T \right)$  is the perturbed viscous stress tensor. Equation 3.19 is the linearized kinematic equation. Besides the no-slip conditions at the wall ( $\hat{u}_2|_{r=R} = \hat{v}_2|_{r=R} = 0$ ) and the symmetry condition ( $\partial_r \hat{u}_1|_{r=0} = \hat{v}_1|_{r=0}$ ), the flow has to satisfy also the interface boundary conditions at the unperturbed interface  $r = \bar{h}(z)$ . We impose in the outer layer the continuity of the velocity

$$\hat{\mathbf{u}}_1 + \hat{h} \partial_r \bar{\mathbf{u}}_1 = \hat{\mathbf{u}}_2 + \hat{h} \partial_r \bar{\mathbf{u}}_2 \quad (3.20)$$

while in the inner layer we impose the tangential and normal stress conditions

$$\left[ \left[ \bar{\mathbf{t}}^T \bar{\sigma}_i \hat{\mathbf{n}} + \bar{\mathbf{t}}^T \hat{\sigma}_i \bar{\mathbf{n}} + \hat{\mathbf{t}}^T \bar{\sigma}_i \hat{\mathbf{n}} + \hat{h} \bar{\mathbf{n}}^T \frac{\partial \bar{\sigma}_i}{\partial r} \bar{\mathbf{n}} \right] \right]_{r=\bar{h}(z), i=1 \rightarrow 2} = 0 \quad (3.21)$$

$$\left[ \left[ \bar{\mathbf{n}}^T \hat{\sigma}_i \bar{\mathbf{n}} + 2\hat{\mathbf{n}}^T \bar{\sigma}_i \hat{\mathbf{n}} + \hat{h} \bar{\mathbf{n}}^T \cdot \frac{\partial \bar{\sigma}_i}{\partial r} \cdot \bar{\mathbf{n}} \right] \right]_{r=\bar{h}(z), i=1 \rightarrow 2} = \gamma (\bar{\mathbf{n}}^T \hat{\mathcal{C}} \bar{\mathbf{n}} + 2\hat{\mathbf{n}}^T \cdot \bar{\mathcal{C}} \bar{\mathbf{n}}) \quad (3.22)$$

where the notation  $[[\cdot]]_{i=1 \rightarrow 2}$  denotes the jump from the inner to the outer flow. The geometric properties of the perturbed interface are obtained by introducing the flow

decomposition (3.16) into the relations (3.11-3.13) and linearising. In particular, the perturbed normal vector  $\hat{\mathbf{n}}$  and curvature  $\hat{\mathcal{C}}$  are written as:

$$\hat{\mathbf{n}} = -\frac{\partial_z \hat{h} (\partial_z \bar{h}, 1)}{\left(1 + (\partial_z \bar{h})^2\right)^{3/2}} \quad (3.23)$$

$$\begin{aligned} \hat{\mathcal{C}} = & -\frac{\hat{h}}{\bar{h}^2 \left((\partial_z \bar{h})^2 + 1\right)^{1/2}} + \left( \frac{3\partial_{zz}\bar{h}\partial_z\bar{h}}{\left((\partial_z \bar{h})^2 + 1\right)^{5/2}} - \frac{\partial_z \bar{h}}{\bar{h} \left((\partial_z \bar{h})^2 + 1\right)^{3/2}} \right) \partial_z \hat{h} \\ & - \frac{1}{\left((\partial_z \bar{h})^2 + 1\right)^{3/2}} \partial_{zz} \hat{h} \end{aligned} \quad (3.24)$$

At the inlet boundary we impose an homogeneous Dirichlet conditions on the radial velocity  $\hat{v}$  and interface displacement  $\hat{h}$ . Finally at the outlet we add a sponge region where the velocities and the height function are forced smoothly towards zero (see details § 3.7).

The equations (3.17)-(3.19), together with the boundary conditions are discretized in space similarly to the base-flow ( $P3 - P2$  elements). The interface perturbation  $\hat{h}$  has been discretized with a  $P2$  element defined on the interface boundary. The meshes as well as the discrete matrices resulting from Galerkin finite-element method are generated with the software FreeFem++ (Hecht (2012)), leading to a generalized eigenvalue problem

$$\mathbf{A}\mathbf{x} = -i\omega\mathbf{B}\mathbf{x} \quad (3.25)$$

where  $\mathbf{x}$  is a vector containing all the discrete unknowns of the problem, i.e. velocities and pressure for the two fluids and the interface perturbation  $\hat{h}$ . The matrix  $\mathbf{A}$  contains the discretization of the differential operators and includes the boundary conditions. To build the matrix, the following steps have to be performed: (i) we build the matrices  $\mathbf{A}_1$  and  $\mathbf{A}_2$  for the separated domains, (ii) we build the linking matrices  $\mathbf{U}_c$  and  $\mathbf{St}$  and (iii) finally we assembly the four matrices into the global one. A sketch of the matrices structure is shown in figure 3.4. The matrix  $\mathbf{A}_1$  contains the discretization of the stokes equations for the inner fluid and the kinematic equation with a stress condition on the interface. The matrix  $\mathbf{A}_2$  contains the discretization of the stokes equations for the outer fluid, where we have a Dirichlet boundary condition on interface velocity. The two sub-problems are coupled together by imposing at discrete level the stress exerted by fluid 2 on fluid 1 with a matrix  $\mathbf{St}$  and the continuity of velocity at the interface with the matrix  $\mathbf{U}_c$ . The matrix  $\mathbf{B}$  is in principle equal to a mass matrix on the degree of freedom related to the interface position and null anywhere else. Nonetheless, for numerical stability reasons, at the left-hand side of the perturbed Stokes equation (3.17), a small term  $-i\epsilon\omega\hat{\mathbf{u}}_i$  is added. The value  $\epsilon = 10^{-5}$  has been chosen in such way that the

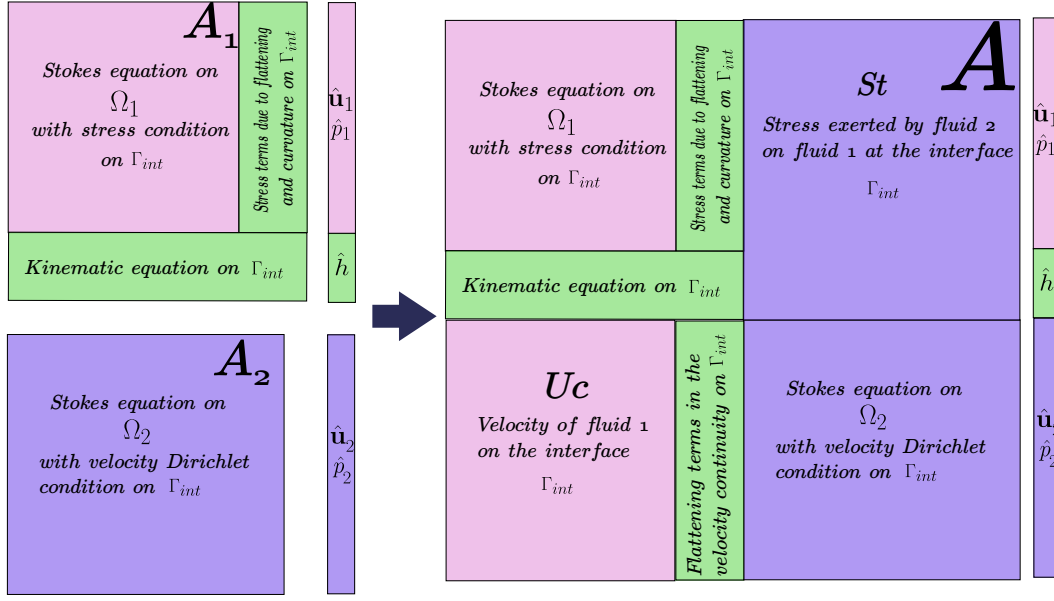


**Figure 3.4** – Structure of matrix  $A$  for the global stability analysis

first four digits of the most unstable eigenvalue did not change with the addition of this term. The eigenvalue problem (3.25) is solved with a Krilov-Shur method along with a shift-invert strategy by using the numerical library SLEPc (Hernandez, Roman & Vidal (2005)).

### 3.3 Validation: stability of a parallel flow

In the following we will take into account a parallel flow. We took as computational domain a part of an infinitely long pipe where the two phase flow is fully developed. Therefore the interface height is constant ( $\bar{h}(z) = H_{in} = H_{out}$ ), the base flow velocity field depends only on the  $r$ -coordinate  $\bar{\mathbf{u}} = \bar{\mathbf{u}}(0, \bar{u}_z(r))$  and the pressure field  $\bar{p}$  respects both the pressure jump at the interface  $\bar{p}_1 - \bar{p}_2 = \gamma\mathcal{C} = \gamma/H_{out}$  and the pressure gradient  $\partial_z \bar{p} = -4\mu_2 u_D / (R^2 - H_{out}^2)$ . The parallel flow case allows us to validate the global stability tools against the results of a local stability analysis. As reference we consider the lubricated local analysis performed by Guillot *et al.* (2007) and the exact local analysis performed by Herrada *et al.* (2008) for the creeping flow limit.

Figure 3.5 shows the stability for a parallel flow case with interface height  $H_{out} = 0.5$ , viscosity ratio  $\lambda = 1$ , Capillary number  $Ca = 1/20$ . As a first validation we impose periodic boundary conditions at the right and left boundaries. As expected the global analysis spectrum recover the local analysis dispersion relation. In figure 3.5a we see that the global analysis is in excellent agreement with the exact analysis by Herrada *et al.* (2008), while under the lubrication hypothesis (Guillot *et al.* (2007)) we have an



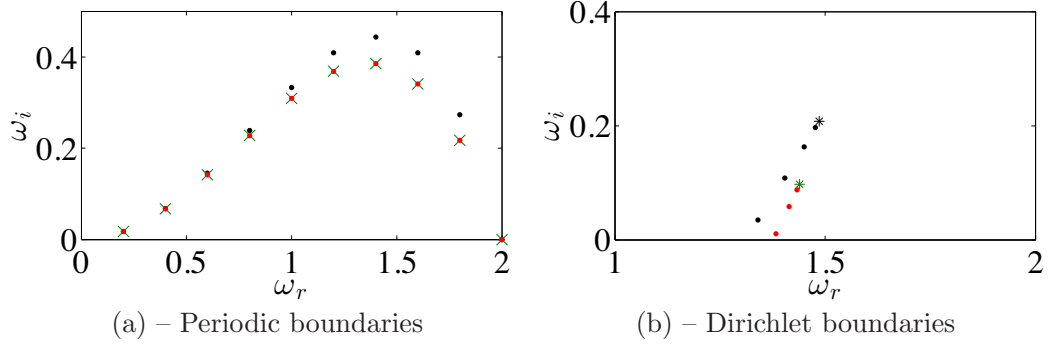


**Figure 3.5** – Comparison of the global and local stability results for a parallel flow case with  $H_{out} = 0.5$ ,  $\lambda = 1$  and  $Ca = 1/20$ . The computational domain has height  $R = 1$  and width  $L = 10\pi$ . At inlet and outlet we impose different boundary conditions (a) periodic boundary (b) Dirichlet boundary  $u_r' = 0$  and  $\eta = 0$ . The black dots ( $\bullet$ ) are the solution of the local lubrication stability analysis performed by Guillot *et al.* (2007), with periodic boundary conditions on the left, and dirichlet conditions on the right. While the green crosses ( $\times$ ) are the exact solution of the local analysis performed by Herrada *et al.* (2008). The red dots ( $\bullet$ ) are the solution of the global stability analysis. While the stars are the saddle points of Guillot ( $*$ ) and Herrada ( $*$ ) dispersion relation.

overestimation of the growth rate.

Successively we consider a finite computational domain, where we impose the Dirichlet boundary conditions  $\hat{v} = \hat{h} = 0$  both at the inlet and the outlet. The global modes for an  $z$ -independent system, such as the one studied in this section, are known to be precisely the absolute modes of the system. The global mode spectrum therefore comprises a set of points at the absolute frequencies  $(\omega_0, k_0)$  and the global mode will be  $\hat{q}(z, r) = q'(r) \exp(ik_0 z)$ . Additionally, a continuous branch of the spectrum emanates from each saddle points (see, for example, Huerre & Rossi (1998), Heaton *et al.* (2009)). This holds exactly in the limit of an infinite domain. In contrast, when we consider a computational box of finite size a discrete spectrum of global modes which satisfy the boundary conditions is expected. In figure 3.5b we see that the absolute mode does indeed mark a point at which a sequence of global modes begins. The global modes behaviour is also confirmed in the lubrication hypothesis case, where we perform a global analysis by using a simplified model derived by taking advantage of the lubricated polynomial dispersion relation (see Sec. 3.8 for details). Figure 3.5b shows that in the lubricated case both the frequency and growth rate of the global modes are overestimated.

### 3.4 Base flow of co-axial streams

The set of possible parameters to describe the base flow is a very large parameter space. Therefore, we will concentrate on present few sets of interesting parameters and then we will concentrate on present the results of the stability.

The base flow is obtained as described in § 3.2.1. We use a rectangular computation domain with height  $R$  and width  $10R$ . The domain is long enough to allow the flow to reach the fully developed state. The inlet profile, assumed parabolic in the inner layer and parabolic-logarithmic in the outer layer, introduces a region of local deficit which gradually recedes as a parabolic channel flow profile developed downstream.

The base flow changes rapidly as it evolves downstream. In figures 3.6 -3.7 we plot the streamwise and radial velocity for different location along  $z$ . In the region close to the nozzle we notice that a region with negative radial velocity appears, which quickly diminishes. The bi-Poiseuille flow develops in about a radius  $R$ . The necessary space to obtain a completely developed flow does not depend on the initial confinement  $H_{in}/R$  of the co-axial flow, as also confirmed by figure 3.8.

The base flow and the interface location depend on the Capillary number  $Ca$ , the viscosity ratio  $\lambda = \mu_1/\mu_2$ , flow rate ratio  $Q = Q_1/Q_2$  and aspect ratio  $H_{in}/R$ . Figure 3.9 underlines how the streamwise velocity in the entry region and the height of the interface depends on the aspect ratio. Changing the viscosity ratio, the monotonicity of the interface position changes. If the outer flow is more viscous the interface reaches the fully developed state always in non-monotonous way. Moreover, for the same imposed inlet flow rate  $Q_1$  and  $Q_2$ , if  $\lambda < 1$  the flow evolves faster, reaching the fully developed state before than the opposite case when the inner flow is more viscous.

Surprisingly, the surface tension play a minor role on the base flow. Increasing the surface tension, for the same operating parameters, the interface position does not change. As consequence also, the velocity field is not effected by the increasing of the surface tension. Some small different can be noticed only when the inner flow is more viscous than the outer (see Fig. 3.10). Only the pressure jump, according to the Laplace law, increases if the surface tension increases.

### 3.5 Stability of the spatially developing flow

We now investigate the stability of the steady spatially developing flow described in the section above.

Fig. 3.11 shows how the surface tension on the interface can affect the stability of the flow. We consider a co-axial flow with  $H_{in} = 0.5$ ,  $H_{out} = 0.4$ ,  $\lambda = 5$  and we decrease the Capillary number. In  $(\omega_r, \omega_i)$ -plane we plot the eigenvalues obtained by the global

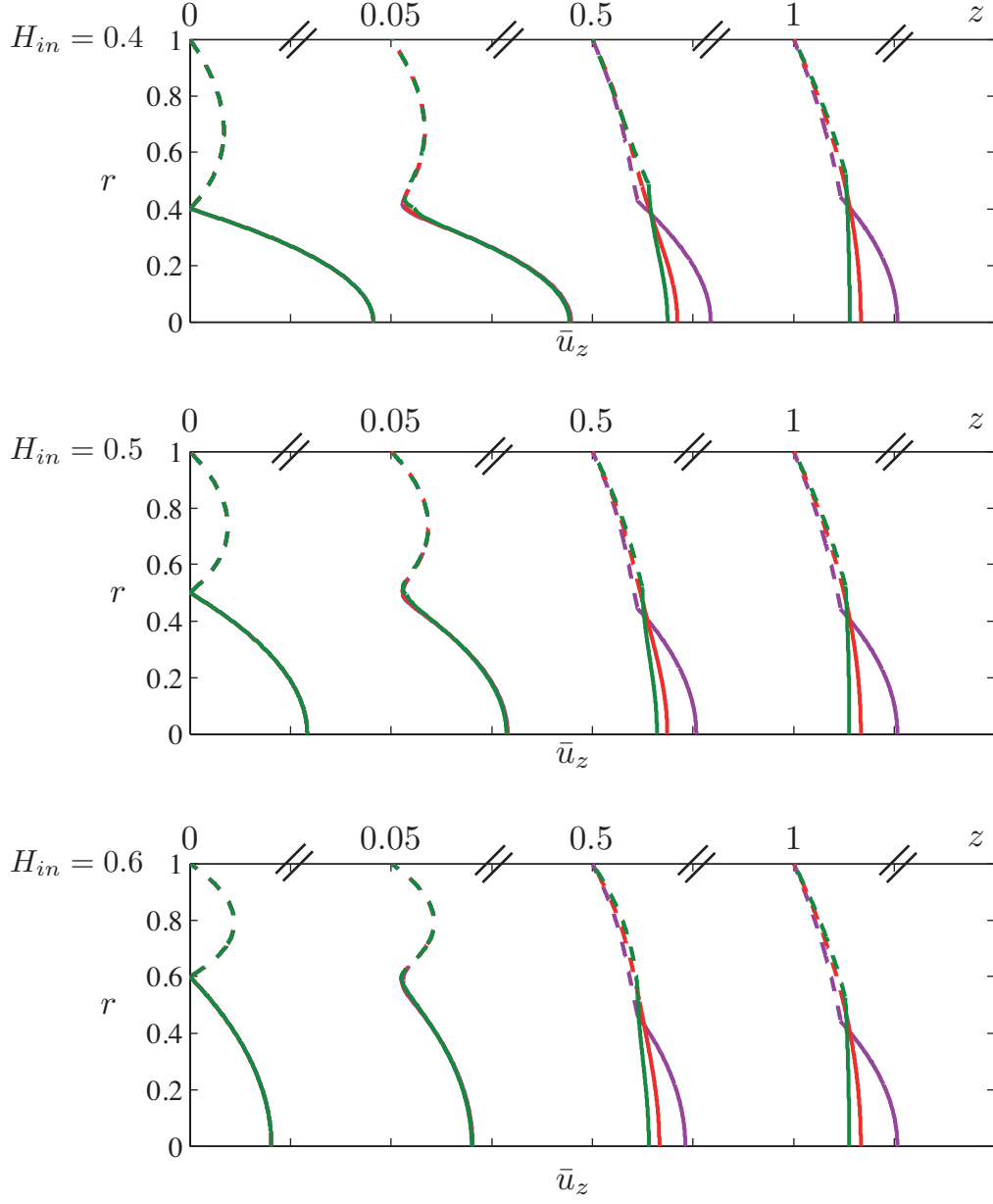


**Figure 3.6** – Velocity profile  $\bar{u}_z$  for different section along  $z = \{0, 0.05, 0.5, 1\}$ . The continuous lines are the velocity profiles for the inner fluid, while the dashed lines for the outer. Simulations done for  $\bar{Q}_1 = 0.9163$ ,  $\bar{Q}_2 = 1.1781$  and  $Ca = 1$ . From the top to the bottom  $H_{in} = 0.4, 0.5, 0.6$  and  $\lambda = 1/5$  (purple line),  $\lambda = 1$  (red line) and  $\lambda = 5$  (green line).

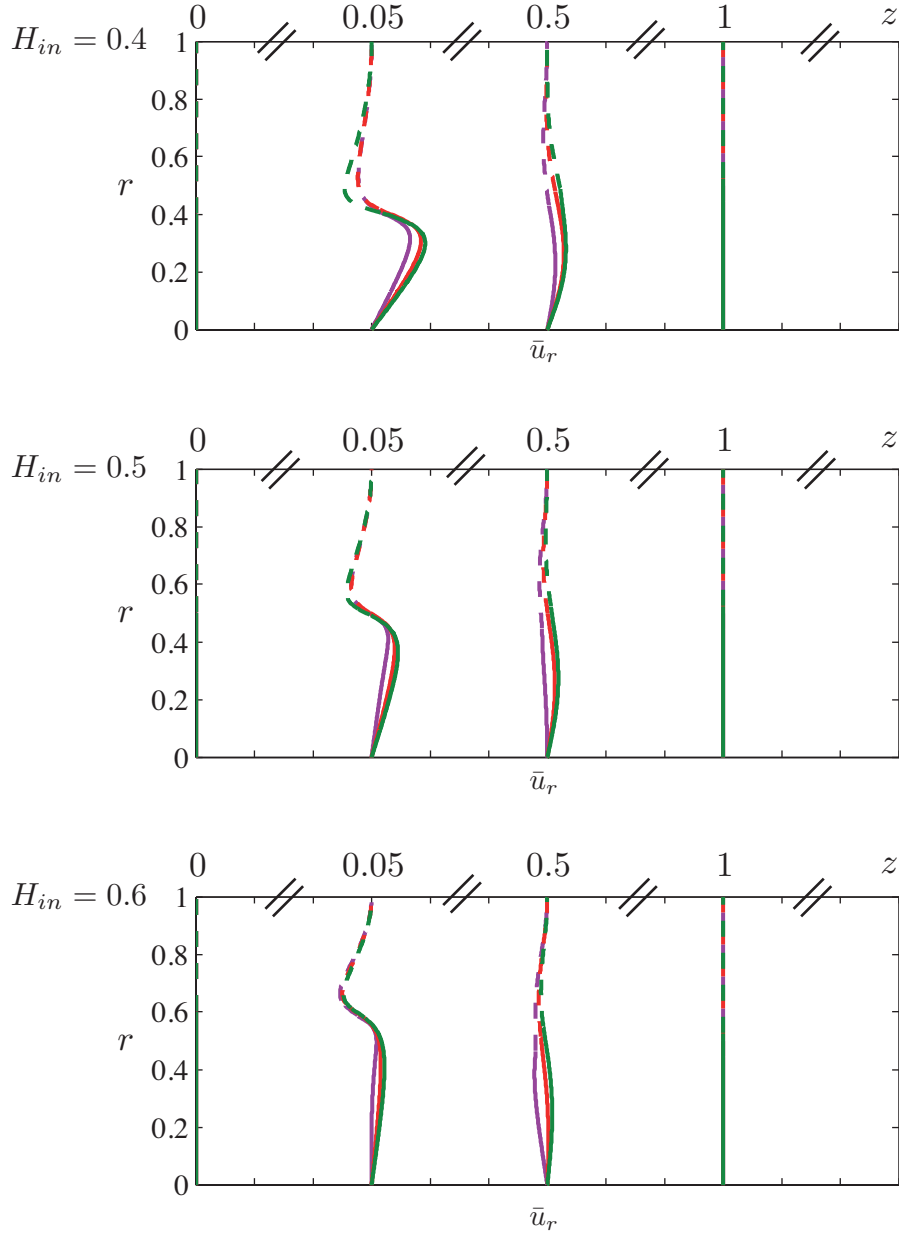


**Figure 3.7** – Velocity profile  $\bar{u}_r$  for different section along  $z = \{0, 0.05, 0.5, 1\}$ . The continuous lines are the velocity profiles for the inner fluid, while the dashed lines for the outer. Simulations done for  $\bar{Q}_1 = 0.9163$ ,  $\bar{Q}_2 = 1.1781$  and  $Ca = 1$ . From the top to the bottom  $H_{in} = 0.4, 0.5, 0.6$  and  $\lambda = 1/5$  (purple line),  $\lambda = 1$  (red line) and  $\lambda = 5$  (green line).

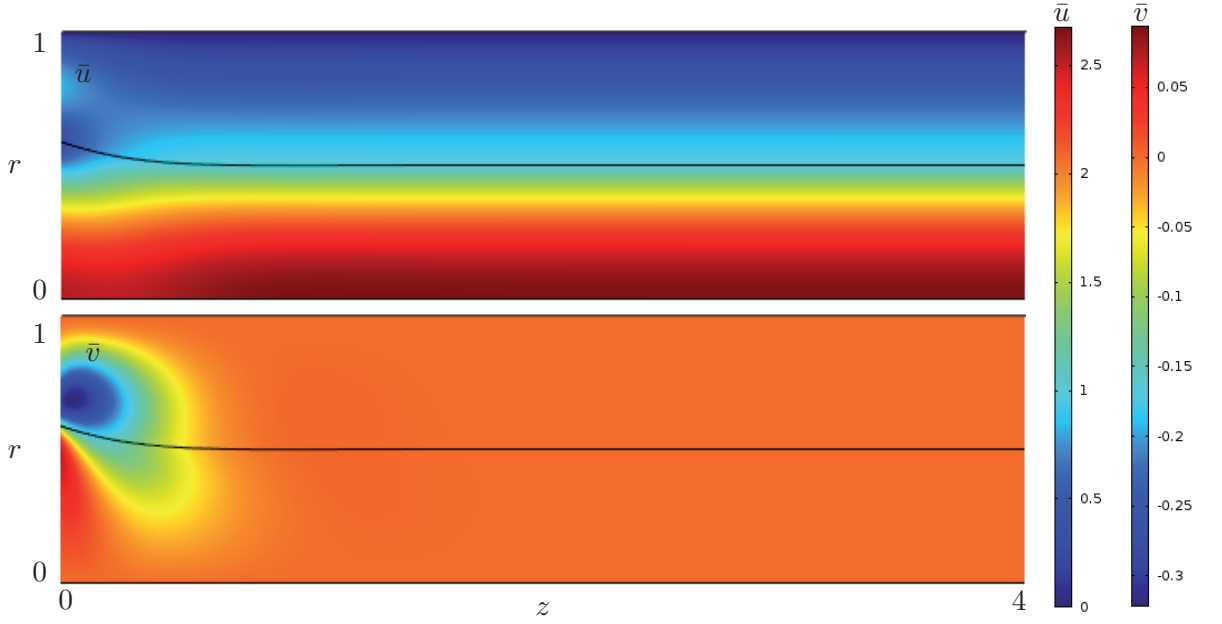


**Figure 3.8** – Streamwise velocity  $\bar{u}$  (top) and radial velocity  $\bar{v}$  for a co-axial flow with  $\bar{Q}_1 = 0.9163$ ,  $\bar{Q}_2 = 1.1781$ ,  $H_{in} = 0.6$ ,  $\lambda = 1/5$  and  $Ca = 1$ .

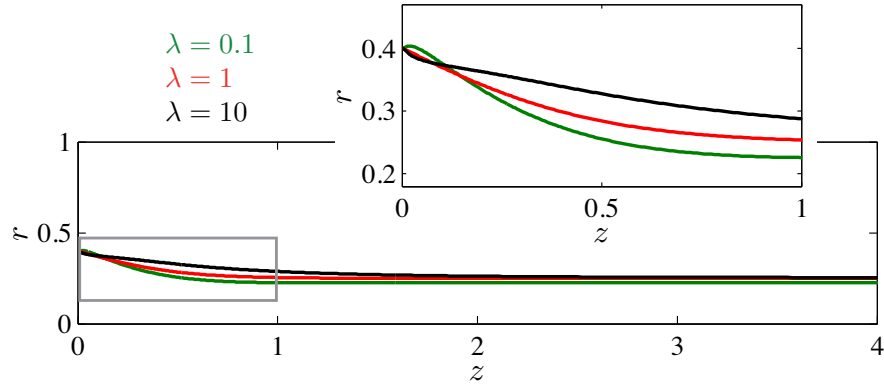


**Figure 3.9** – Influence of the viscosity ratio on the interface displacement. We impose at the inlet  $Q_1 = 0.2029$ ,  $Q_2 = 1.4726$  and  $H_{in} = 0.4$  and we determine the interface height for different viscosity ratio  $\lambda = \{0.1, 1, 10\}$ . When the outer flow is more viscous  $\lambda < 0.1$  (green line) we can observe the interface height  $h(x)$  is not monotonous, and it reaches the fully developed state faster than when the inner flow is more viscous  $\lambda = 10$  (black line).

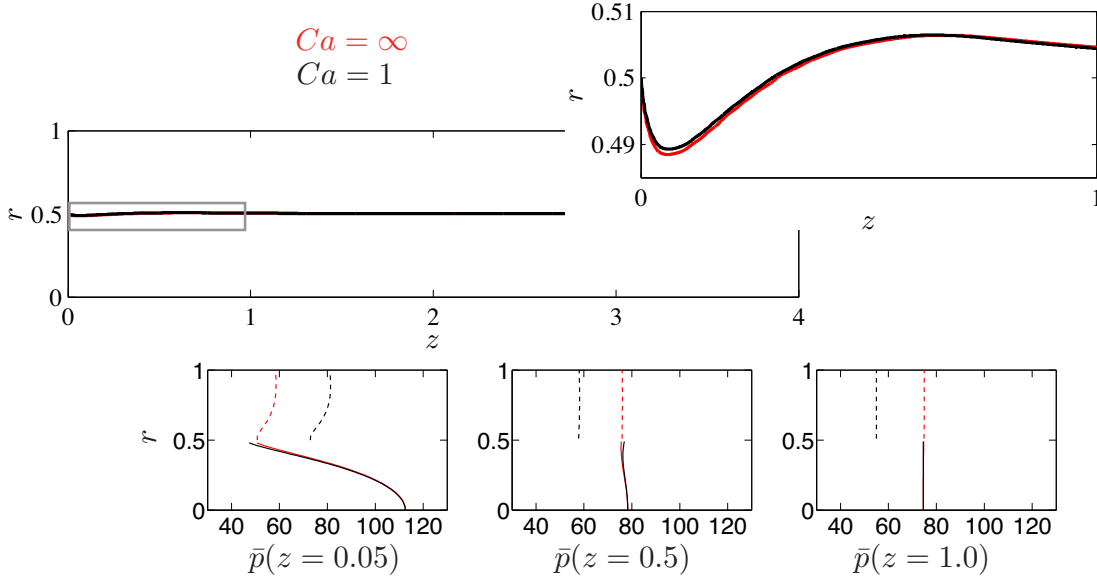


**Figure 3.10** – Influence of the surface tension on the base flow.  $H_{in} = 0.5$ ,  $H_{out} = 0.5$ ,  $\lambda = 5.0$ . Imposed flow rate  $Q_1 = 0.8116$  and  $Q_2 = 1.1781$ . The red line corresponds to the case without surface tension, while the black line is determined with  $Ca = 1$ .

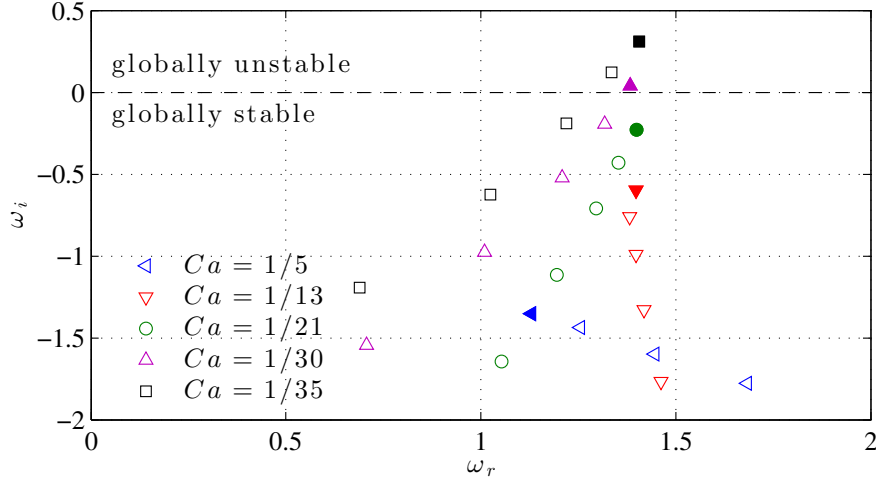


**Figure 3.11** – Eigenvalues for  $H_{in} = 0.5$ ,  $H_{out} = 0.4$ ,  $\lambda = 5$  and decreasing value of  $Ca$ . At each combination of color and marker is associated a different value of  $Ca$ . The filled markers are the most unstable eigenvalue for that capillary number.

stability described in § 3.2.2. The frequency and growth-rate of the eigenvalues are given by the real and complex part of  $\omega = \omega_r + i\omega_i$  respectively. We observe a bifurcation from stable ( $\omega_i < 0$ ) to unstable ( $\omega_i > 0$ ) between  $Ca = 1/21$  and  $Ca = 1/30$ . The growth rate increases if the Capillary number decreases. If  $Ca < 1/35$  there are several unstable modes, in analogy with the general picture shown in Sec. 3.3. The spatial shape of the unstable mode can be seen in figure 3.12. The streamwise and radial components of the oscillation  $\hat{u}$ ,  $\hat{v}$  and the perturbed interface are amplified downstream.

In the following, we are interested on the stable/unstable bifurcation point. The bifurcation point is found as the smallest Capillary number such that there is at least one unstable mode.

The bifurcation points can be determined as function of two dimensionless parameters: the interface position  $H_{out}$  and the capillary number  $Ca$ . Figure 3.13 describes the dynamic behavior of our system, with the transition separating the unstable region (below the points) and the stable region (above the points) in  $(H_{out}, Ca)$ -plane for a fixed inlet nozzle position  $H_{in} = 0.5$  and varying viscosity  $\lambda = \{1/5, 1, 5\}$ . In the  $(H_{out}, Ca)$ -plane we can also plot the absolute/convective unstable transition obtained from the local stability analysis for the same operating parameters. Convective instabilities, which are convected downstream while growing in amplitude, are in this setting represented by the stable eigenvalues. Absolute instabilities, which growth and travel backwards, instead, are represented by the unstable eigenvalues. In the specific, the bifurcation points are plotted against the A/C transition found by Guillot *et al.* (2007) (black lines) and Herrada *et al.* (2008) (red lines). Generally, we observe that the global stability predicts a more stable flow than the averaged and exact local analyses. In particular we notice that for small value of the degree of confinement  $H_{out}$  the analytical local solution and the global stability have the same qualitative and qualitative behaviour, while the averaged local stability fails in the prediction of the convective/absolute transition. In contrast the averaged and exact local solutions slightly overestimate the global results when the confinement ratio is large ( $H_{out} \leq 1$ ) and the flow becomes more sensitive to the presence of the wall. The viscosity ratio has a large impact on the stability proprieties of the flow. In particular, the flow is more and more stable as the viscosity ratio  $\lambda$  decreases.

We now let the nozzle radius  $H_{in}$  vary. From the different base flow behaviour depicted in Sec.3.4, a relevant effect was expected. Surprisingly, for a fixed  $H_{out}$  the critical capillary number slightly depends has been found insensitive to the nozzle dimension, as shown in figure 3.14. The error bars in the figure are computed by keeping fixed the mesh resolution and by just changing the interface interpolation spline. We estimate an average error of about 10% due to the interface interpolation procedure. We can see that the fitting error is comparable to the influence of the nozzle position. Out of these considerations, we can estimate a general uncertainty in the critical capillary number, related to the nozzle geometry along with the interface relaxation shape, of about 12.5%.

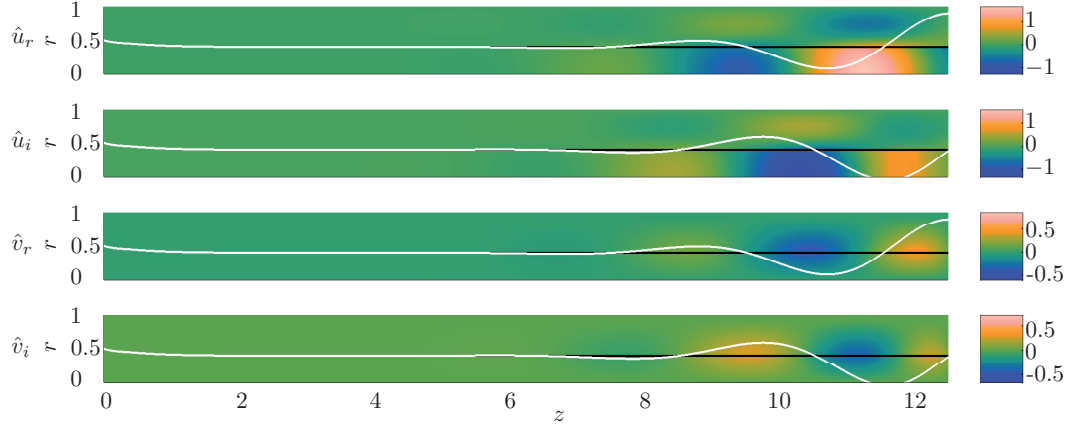


**Figure 3.12** – Real and imaginary part of the eigenfunctions of unstable mode for  $H_{in} = 0.5$ ,  $H_{out} = 0.4$ ,  $\lambda = 5$  and  $Ca = 1/30$ . Comparison unperturbed interface (black line) and perturbed interface (white line). The color map is scaled with the maximum real amplitude of  $\hat{\eta}$  of the eigenfunction.

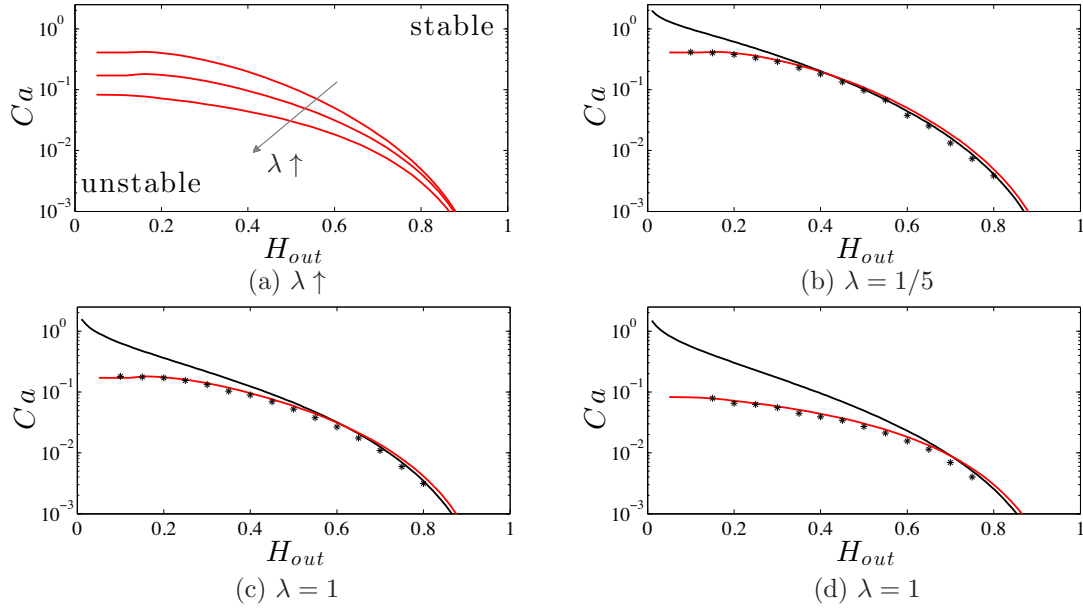


**Figure 3.13** – Phase diagram of the instability in the  $(H_{out}, Ca)$  plane for a fixed value of  $H_{in} = 0.5$  and different value of viscosity ratio  $\lambda = \{1/5, 1, 5\}$ . The black lines represent the local lubrication analysis Guillot *et al.* (2007), the red lines are the noninertial analytic local solution Herrada *et al.* (2008) with the addition of the flattening terms. The black point are the results of our global analysis. Above the lines, the system is stable, while below is unstable.



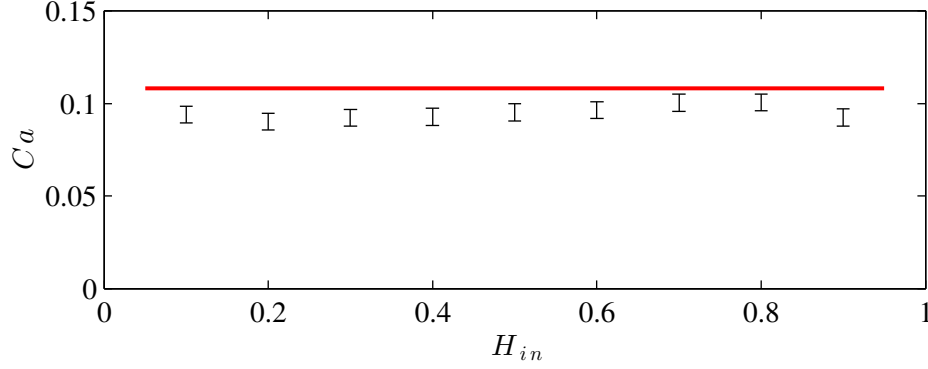


**Figure 3.14** – Phase diagram of the instability in the  $(H_{in}, Ca)$ -plane for a fixed value of the degree of confinement  $H_{out} = 0.5$  and viscosity ratio  $\lambda = 1/5$ . The red line is the theoretical line separating the dripping region (above) and the jetting region (below) predict by the local analysis (Herrada *et al.* (2008)). The black lines are the global modes and the respective error bars for different value of the inner radius of the pipe.

Following the guideline of Herrada *et al.* (2008) and Guillot *et al.* (2007), we represent the stability results also in the  $(Q_1, Q_2)$  operational plane, for values of the parameters common in microfluidic devices (see figure 3.15). This representation is particularly useful for comparison with experimental data, since in experiments the flow is modified by changing the flow rates. At fixed  $Q_2$ , increasing  $Q_1$  increases the jet velocity allowing the instability to have more convection, and this behaviour promotes continuous jets. As observed above, for small value of the outer flow rate  $Q_2$ , that correspond to large value of  $H_{out}$  the local solution slightly overestimate the global results. In the graphs is also plotted the error made keeping  $H_{in}$  fixed and with the interpolation of the steady interface. We notice that a constant error in the Capillary number is translated in a constant error on the interface velocity (grey region). We can conclude that the dripping to jetting transition is a process mostly dominated by the intrinsic properties of the developed streams, and that the development of the flow in the entry region stabilize the flow. In particular, the entry region seems to be more relevant for low values of the external flow rate. Moreover, also the uncertainty on the nozzle geometry seems to have a relevant role at those flow operating conditions. It is noteworthy that also available experimental data (see Herrada *et al.* (2008)) shows that in this regime the flow is more stable than the local analysis prediction. This is confirmed by figure 3.16: the stable/unstable transition is plotted against the co-axial experiments performed by A. Colin and M. Moire (IFP). From the graph we observe that the global stability prediction is more accurate than the local analysis one.

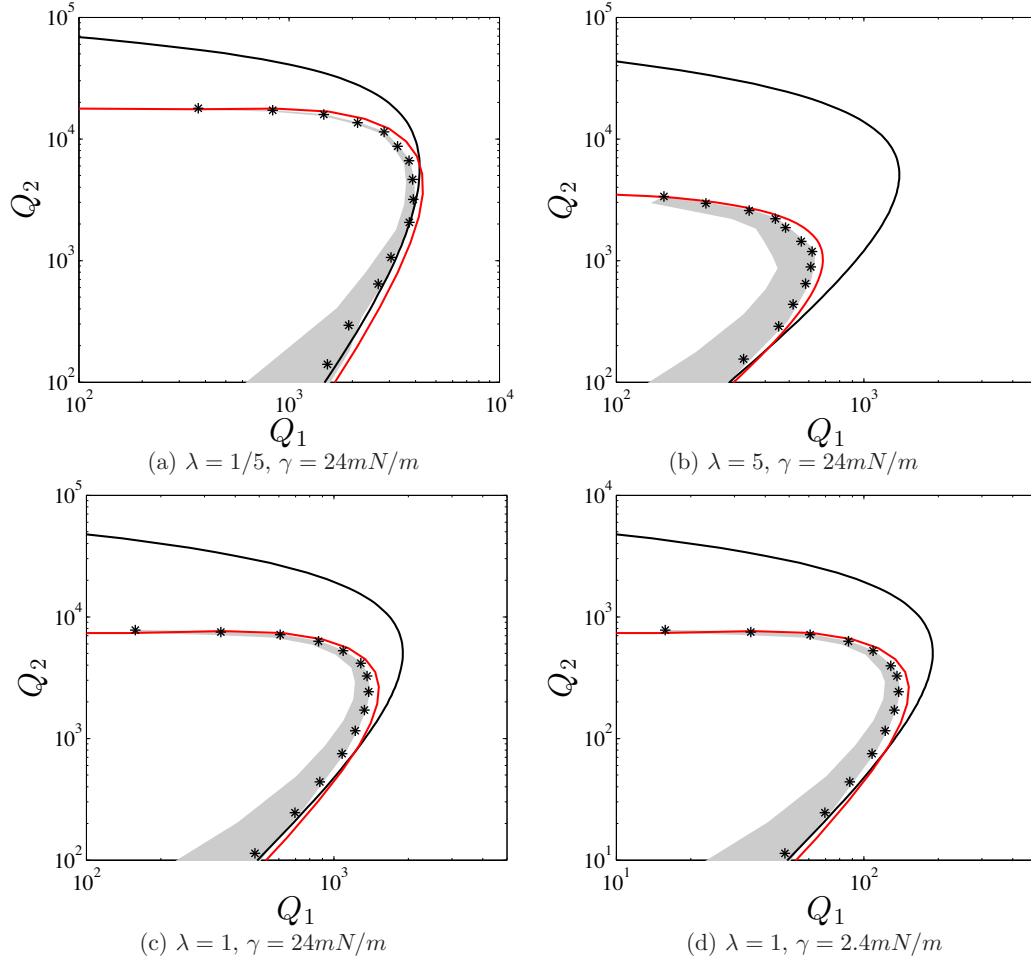


**Figure 3.15** – Dynamic behavior in  $(Q_1, Q_2)$  plane and stable/unstable transition. The black lines correspond to the lubrication co-axial analysis performed by Guillot *et al.* Guillot *et al.* (2007). The red line represent the no-inertial analytic solution found by Herrada *et al.* Herrada *et al.* (2008) with the addition of the flattening terms in the analysis. The black points are the results of our global stability analysis. The flow rates are expressed in  $[\mu L/h]$ , the outer radius is  $R = 275\mu m$  while the outer viscosity  $\mu_2 = 0.235Pa s$ . The nozzle radius is  $H_{in} = 1/2R$  for all transition illustrated.

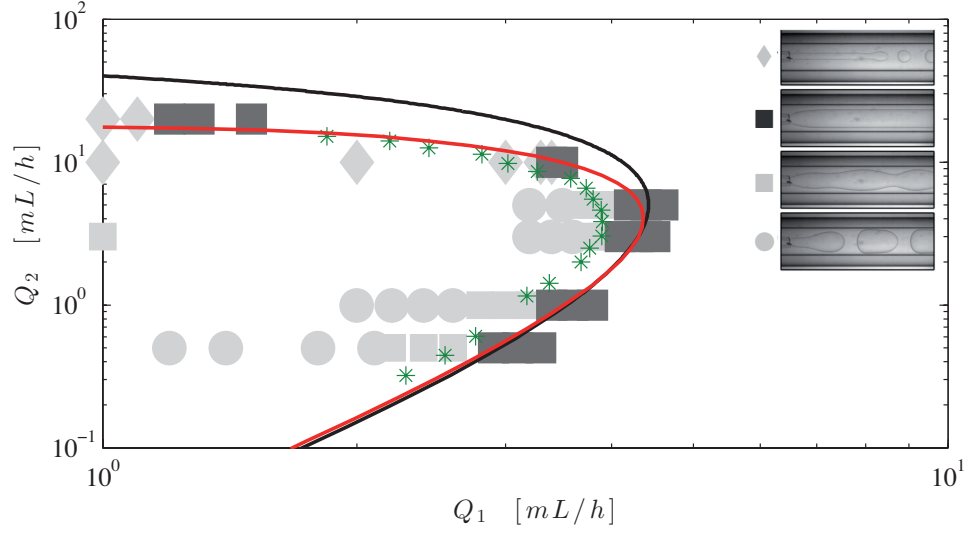


**Figure 3.16** – Flow behavior in the  $(Q_1, Q_2)$ -plane. The jetting regime comprises thin jets breaking into droplets ( $\diamond$ ), wide straight jets ( $\blacksquare$ ) and jets with peristaltic modulation ( $\blacksquare$ ), while the dripping regime is described by drop plug ( $\bullet$ ). The black line is the dripping/jetting transition found with the exact local analysis, while the red line is the stable/unstable transition found with the global analysis. Comparison of experimental data and numerical results with  $\mu_1 = 47.69 \text{ mPa s}$ ,  $\mu_2 = 247.29 \text{ mPa s}$ ,  $\mu_2$ ,  $\gamma = 26.5 \text{ mN/m}$ ,  $R_2 = 275 \mu\text{m}$ . Experiments made by A. Colin and M. Moire (IFP).

### 3.6 Conclusion

In this study, we have analysed the influence of the entry region on the dripping to jetting transition in a coflowing streams device.

We have first investigated the effect of several parameters such as the flow rate ratio  $Q$ , the viscosity ratio  $\lambda$  and the capillary number  $Ca$  on the flow behaviour of the steady continuous jets solution. In addition, we characterized the effect of geometry by varying the nozzle radius  $H_{in}$ , showing that the flow vary rapidly (in about one radius) from the bi-Poiseuille solution to the parallel developed flow.

In the second part we performed a global stability analysis of the spatially evolving two phase flow. We found that the global stability of the non-parallel flow recover always more stable results of the exact local analysis by Herrada *et al.* (2008). In the entry region, where the interface velocity is close to zero, the flow is locally absolutely unstable and, as consequence, the flow becomes globally more stable. Surprisingly, for high external flow rate value, the global stability analysis almost recover the same results of the exact local analysis. This implies that for low degree of confinement the dripping to jetting transition is a process dominated by the intrinsic proprieties of the developed streams and not by the geometrical details of the injection co-axial nozzle. In contrast for small external flow rate value, or high degree of confinement, the flow is more sensitive to the presence of the wall and becomes more stable than the local stability theory prediction.

Cordero *et al.* (2011) showed that the linear analysis fails to predict the frequency selection in the dripping regime and they suggest that it is maybe caused by local shear effects at the nozzle. However, the present analysis can not take into account transient non linear effects which can be dominant and have to be investigated by means of non linear simulations.

### 3.7 Appendix 1: Sponge region at the outlet of the perturbed computational domain

The sponge region is extends from  $L_{bf} = 12.5R$  to  $L_{gs} = 15$  and in this region we impose a forcing both in the momentum and kinematic equation:

$$\xi_f = \frac{\alpha f}{1 + \exp\left(\frac{1}{z'-1} + \frac{1}{z'}\right)} \quad (3.26)$$

where  $z' = \frac{z-L_{bf}}{L_{gs}-L_{bf}}$ ,  $\alpha = 50$  is the force strength parameter and  $f$  indicates respectively  $\{\mathbf{u}, \eta\}$ .

### 3.8 Appendix 2: Toy model for the global stability analysis of coaxial jets under the lubrication hypothesis

Under the lubrication hypothesis, the dispersion relation for the coaxial jets has a polynomial form (Guillot *et al.* (2007)):

$$\omega(k) = \alpha k + i\beta (k^2 - k^4 h^2) \quad (3.27)$$

where  $\alpha$  and  $\beta$  are functions of the flow parameters ( $Ca$ ,  $\lambda$  and  $Q$ ) and  $h$  is the interface position.

In same cases, such as this one, it is possible to recover the underlying PDE from the dispersion relation. Let us consider a general plane wave solution  $\phi(z, t) = \phi_0 \exp(ikz - i\omega t)$ , where the differential operators become:

$$\frac{\partial}{\partial t} = -i\omega \quad (3.28)$$

$$\frac{\partial^n}{\partial z^n} = (ik)^n \quad (3.29)$$

By manipulating Eqs.(3.28-3.29) and (3.27) we obtain:

$$\frac{\partial \phi}{\partial t} = -\beta \left( \frac{\partial^2 \phi}{\partial z^2} + h^2 \frac{\partial^4 \phi}{\partial z^4} \right) - \alpha \frac{\partial \phi}{\partial z} \quad (3.30)$$

This one dimensional problem can be used to carry out a global stability analysis and to investigate the effect of the streamwise confinement. In the spirit of a global analysis, let us consider a solution in the following form  $\phi(z, t) = \hat{\phi}(z) \exp(-i\omega t)$ , where only the time dependence is sought in normal mode form. We obtain the following eigenvalue problem:

$$-i\omega B \hat{\phi} = A(\alpha, \beta) \hat{\phi} \quad (3.31)$$

where  $A = -\beta \left( \frac{\partial^2}{\partial z^2} + h^2 \frac{\partial^4}{\partial z^4} \right) - \alpha \frac{\partial}{\partial z}$ .

Problem (3.31) is numerically solved with a Chebyshev spectral collocation method in a physical domain ranging from  $0 \leq z \leq L$ , with inlet and outlet homogeneous Dirichlet boundary conditions.

As already noted by Heaton *et al.* (2009), there is an upper limitation on the lenght  $L$  of the computational box. In figure 3.17 we can see that when  $L$  is larger than  $20\pi$  the global spectrum is not aligned on a single branch, but instead the eigenvalues arrange

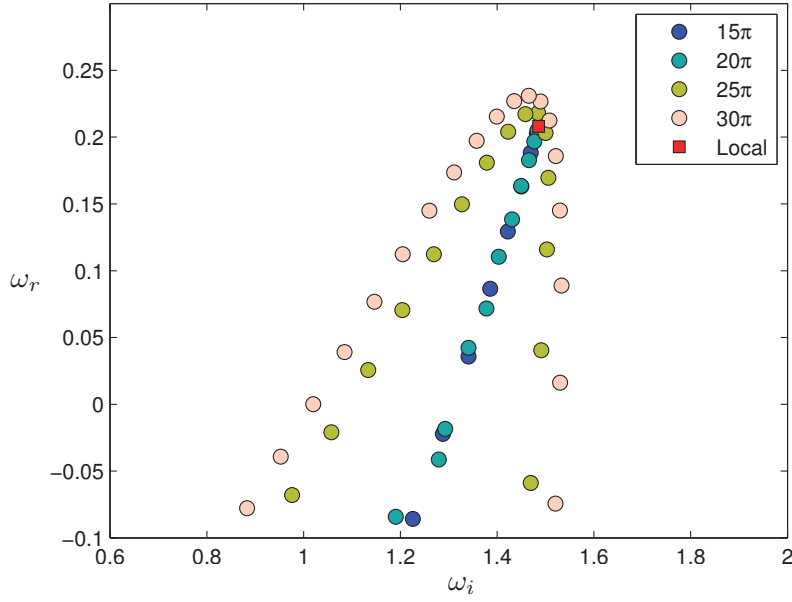


**Figure 3.17** – Influence of the length of the domain  $L$  on the eigenvalues with  $\alpha = 1$  and  $\beta = 0.4438$ , i.e. degree of confinement  $h = 0.5$ , viscosity ratio  $\lambda = 1$  and Capillary number  $Ca = 1/20$ .

themselves on a bell shaped curve which passes above the location of the true global mode. Heaton *et al.* (2009) suggest that this phenomenon is caused by a combination of the non-normality of the linear operator and issues of numerical precision. Since the global mode is expected to grow exponentially in the axial direction, if the computational box is too large the global mode can not be resolved accurately. Heaton *et al.* (2009) proposed that  $|k_{0i}|L < c$  where  $c$  is a constant that depends on the considered case.

## 4 Complex fluid-fluid interface: surface viscosity

In the previous chapters, we saw that interfaces between two-phase fluids occur in everyday life, both in nature or in industrial applications. When the two phases are not contaminated with insoluble material, the value of the surface tension is sufficient to characterize the interface (Young (1805)). However, in most biological and technological application, surfactants, particles and proteins will populate the interface. For this complex fluid interface, it becomes insufficient to characterize the interface only by its tension. It is necessary to generalize the interfacial transport phenomena both across and within the complex fluid-fluid interface (Slattery, Sagis & Oh (2007)). In addition to the surface tension, one should also consider a more general surface stress (Gibbs (1878)).

One of the first studies of a complex fluid-fluid interface was performed by Plateau (1873), who conducted some experiments using a magnetic compass needle. He interpreted the differences of the behavior of the floating needle on a bare interface and on an interface with surfactant as the existence of molecular forces. Plateau's interpretation was probably wrong, as suggested by Marangoni (1872): the rotating floating needle indeed sweeps the interface, and the concentration gradient responds creating a surface tension gradient. To resolve the misunderstanding of Plateau's results, Marangoni (1872) designed a new device with a solid brass disc, which oscillations do not cause any accumulation or dilution of the surface film, but he was not able to measure any significant difference between a bare interface and a surfactant-laden interface, in terms of surface viscosity. Few years later, Rayleigh (1890) proposed a new experiment using a ring. With this device Rayleigh was able to explain the importance of reducing area of the measurement geometry in contact with different phases. Boussinesq (1913) was the first to introduce a mathematical continuum mechanics interfacial description. Boussinesq's equations are not particularly convenient since they are expressed in terms of the principal axes of the surface rate of the deformation tensor. Scriven (1960) rewrote Boussinesq's equations describing the conservation of the momentum at fluid-fluid interface in terms of an arbitrary surface coordinate system.

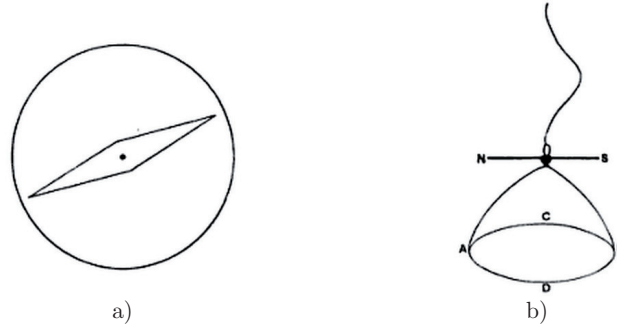


**Figure 4.1** – Sketches of the experiment performed by Plateau (1873) with the floating needle on the left, and by Marangoni (1872) with the brass disc on the right.

One approach is coupling surfactant transport and flow equation. This method can be very complex, because it involves several different processes (Edwards *et al.* (1991)). In general, interfacial stretching or compression induced by bulk flows alters the surface concentration of surfactants, hence the surface tension, which can lead to surface tension gradients (Marangoni effect). This is compensated by surface diffusion and, more importantly for soluble surfactants, by adsorption from the bulk, or desorption to the bulk. These exchanges between the bulk and the interface depend on the subphase bulk concentration, and can be limited either by diffusion or by sorption kinetics. The resulting interfacial stress results from this complex interplay, and only in highly simplified situations, such as in the absence of convection (Lucassen & van den Tempel (1972)), can surface elasticity and viscosity be predicted. In other cases, numerical simulations are required and have been used to study, e.g. drop detachment (Jin *et al.* (2006)). In alternative, instead to model these transport processes in detail, we get a first qualitative insight as to whether surfactants may affect jet instability. Therefore, we have chosen to retain only surface viscosity as a source of mechanical resistance, in the frame of the Boussinesq-Scriven constitutive equation of a Newtonian interface (Scriven (1960); Slattery *et al.* (2007)). This stringent simplification can be justified two-fold: (i) there are situations where the response of the surfactants is indeed dominated by an intrinsic surface viscosity, especially for concentrated solutions at high velocity (Scheid, Delacotte, Dollet, Rio, Restagno, van Nierop, Cantat, Langevin & Stone (2010)), (ii) surface viscosity can be considered as an effective parameter, which often describes qualitatively correctly the mechanical response of a surfactant adsorbed layer. For instance, in the classical example of the settling of a drop in a surface solution, surface elastic and viscous effects, coming from very different processes, all have the same qualitative effects to slow down the settling compared to the case of an interface with free shear (Levich (1962)).

In this chapter we introduce the governing equations and constitutive equations able to describe the surface viscosity in axisymmetric coordinates (§ 4.1). We then outline the effects of the surface viscosity on a viscous thread immersed into a dynamically inert



medium (§ 4.2). Finally, we consider the influence of surface rheology into the two-phase co-axial system (§ 4.3).

## 4.1 Dynamic description of a two-phase flow interface

### 4.1.1 Governing equation

Generally an interface is defined as a three dimensional surface of infinitesimal thickness, separating two adjoining bulk phases. The two-phase physical properties (i.e. mass, momentum and energy) change rapidly but continuously across this region, from their value in one bulk phase to their respective value in the other bulk phase. To describe the effects of interfacial stress-deformation behavior on the dynamics of two-phase systems, a mathematical model has to be introduced for the interface.

The interfacial region is usually modeled as a thin film, with its own behavior and constitutive equations (Slattery *et al.* (2007)-Sagis (2011)). As for the bulk phase, also for the interface the conservation laws have to be set. The interface balance equations act as interfacial boundary conditions for the two bulk phases of the system. In the hypothesis of no mass transfer to or from the interface, if we define as  $\mathbf{u}_s$  the interface velocity, then the conservation of mass requires that on the dividing interface

$$\frac{d_s \rho^s}{dt} + \nabla_s \cdot (\rho^s \mathbf{u}_s) + \llbracket \rho \mathbf{u} \cdot \xi \rrbracket = 0 \quad (4.1)$$

where  $\rho^s$  and  $\rho$  are respectively the density of the interface and the bulk phase and  $\xi$  is the unit normal vector.  $\nabla_s$  is the surface operator, and it is defined as  $\nabla_s = \mathbb{I}_s \cdot \nabla$ , where  $\mathbb{I}_s$  is the surface projector tensor. The surface material derivative  $d_s/dt$  is defined by (Slattery *et al.* (2007), Sagis (2011))

$$\frac{d_s \rho^s}{dt} = \frac{\partial \rho^s}{\partial t} + (\nabla_s \rho^s) \cdot (\mathbf{u}^s - \mathbf{v}) \quad (4.2)$$

where  $\mathbf{v}$  is the speed of displacement of the interface.

The momentum balance requires than on the fluid-fluid interface:

$$\rho^s \left( \frac{\partial \mathbf{u}_s}{\partial t} + (\mathbf{u}_s \cdot \nabla_s) \mathbf{u}_s \right) = \nabla_s \gamma + \gamma \mathcal{C} \xi + \nabla_s \tau^s + \llbracket \sigma \xi \rrbracket, \quad (4.3)$$

where  $\rho_s$  is the surface mass density,  $\gamma$  the surface tension,  $\mathcal{C}$  the curvature. The second order tensor  $\sigma$  is the stress tensor in the bulk phase, while  $\tau_s$  is the surface stress tensor. The equation (4.3) is often referred as jump momentum balance (Slattery *et al.* (2007)), and it describes the change time rate of the surface momentum as function of the surface stress at the interface, and inertial and viscous forces applied at the interface by the adjoining bulk phases.

In the limit of vanishing Reynolds number, and constant surface tension, the momentum balance (4.3) is reduced to

$$0 = \gamma \mathcal{C}\xi + \nabla_s \tau^s + \llbracket \sigma \xi \rrbracket. \quad (4.4)$$

The set of equations (4.1)-(4.4) need to be closed by a constitutive equation for the surface stress tensor  $\tau_s$ .

In order to model the surface stress tensor different constitutive equations have been proposed. Since we are interested in analyzing interfaces with a purely viscous response we use the linear Boussinesq surface fluid model (Scriven (1960)):

$$\tau_s = (\kappa_s - \mu_s) \nabla_s \cdot \mathbf{u}^s \mathbb{I}_s + 2\mu_s \mathbb{D}_s \quad (4.5)$$

where  $\kappa_s$  and  $\mu_s$  are respectively the surface dilatation viscosity and surface shear viscosity,  $\mathbb{I}_s$  is the surface projection tensor and  $\mathbb{D}_s$  is the surface rate of deformation tensor

$$\mathbb{D}_s = \frac{1}{2} \left( \mathbb{I}_s \cdot \nabla_s \mathbf{u}^s + (\nabla_s \mathbf{u}^s)^T \cdot \mathbb{I}_s \right) \quad (4.6)$$

### 4.1.2 Derivation of the constitutive equation

In the following, the essential steps leading to the computation of the divergence of surface stress  $\nabla_s \tau^s$  of a fluid-fluid interface are explain. The Slattery *et al.* (2007)'s notation are used. The derivation is made for a rotationally symmetric surface in cylindrical coordinates:

$$\begin{aligned} x^1 &= r \\ x^2 &= \theta \\ x^3 &= z \end{aligned} \quad (4.7)$$

The free interface is described by the function

$$r = h(z) \quad (4.8)$$

and it is parameterized by

$$\begin{aligned} y^1 &= z \\ y^2 &= \theta \end{aligned} \quad (4.9)$$

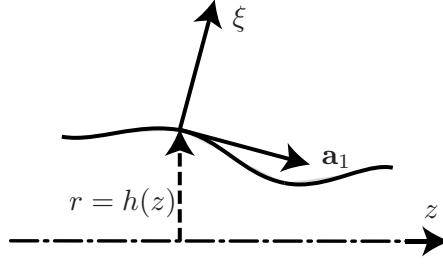


**Figure 4.2** – Geometry of the free surface.

The surface vectors are defined as:

$$\mathbf{a}_\alpha = \frac{\partial \mathbf{p}^s}{\partial y^\alpha} \quad (4.10)$$

where  $\mathbf{p}^s = h(z)\mathbf{e}_r + z\mathbf{e}_z$  is the position vector on the surface. Therefore:

$$\begin{aligned} \mathbf{a}_1 &= h'\mathbf{e}_r + \mathbf{e}_z \\ \mathbf{a}_2 &= h\mathbf{e}_\theta \end{aligned} \quad (4.11)$$

where the superscript denotes the derivative on  $z$ .

Let  $\xi$  be the unit normal vector to the interface pointing from inside to outside.

$$\xi = \frac{\mathbf{e}_r - h'\mathbf{e}_z}{\sqrt{1 + h'^2}} \quad (4.12)$$

Since the vector field  $\mathbf{a}_1$ ,  $\mathbf{a}_2$  and  $\xi$  are linearly independent, they form a basis for the spatial vector field on the free surface.

The divergence of the surface stress, according to Slattery *et al.* (2007) is written as

$$\begin{aligned} \nabla_s \cdot \tau^s &= \left[ (\kappa_s - \mu_s) \frac{\partial}{\partial y^\alpha} \nabla_s u^{s\alpha} \right. \\ &\quad \left. + \mu_s \left( u_{\alpha,\beta\gamma}^s + u_{\beta,\alpha\gamma}^s - 2u_{\xi,\gamma}^s B_{\alpha\beta} - 2u_\xi^s B_{\alpha\beta,\gamma} \right) a^{\beta\gamma} \right] \mathbf{a}^\alpha \\ &\quad + \left[ 2H (\kappa_s - \mu_s) \nabla_s \mathbf{u}_s + \mu_s \left( 2u_{\gamma,\beta}^s - 2u_\xi^s B_{\beta\gamma} \right) B^{\beta\gamma} \right] \xi \end{aligned} \quad (4.13)$$

where all undefined terms are now progressively introduced. The surface divergence of the surface velocity is

$$\nabla_s \cdot \mathbf{u}_s = u_\beta^{s\beta} - 2Hu_\xi^s \quad (4.14)$$

In order to express the divergence of the surface stress (4.13) for an axisymmetric surface,

we introduce the factors  $a_{\alpha\beta} \equiv \mathbf{a}_\alpha \cdot \mathbf{a}_\beta$  defined as:

$$\begin{aligned} a_{11} &= 1 + h'^2 \\ a_{22} &= h^2 \\ a_{12} &= a_{21} = 0 \end{aligned} \tag{4.15}$$

In contrast, the cofactors  $a^{\alpha\beta}$  are defined such that  $a^{\alpha\beta}a_{\beta\gamma} = a_{\gamma\beta}a^{\beta\alpha} = \delta_\gamma^\alpha$  where  $\delta_\gamma^\alpha$  is the Kronecker delta. Introducing the dual basis such that  $\mathbf{a}^\alpha = a^{\alpha\gamma}\mathbf{a}_\gamma$ , it is possible to define the surface velocity in terms of its tangential and normal component as:

$$\mathbf{u}_s = u^{s\alpha}\mathbf{a}_\alpha + u_\xi^s\xi \tag{4.16}$$

To gradients are computed using the rule

$$\frac{\partial \mathbf{a}_\alpha}{\partial y^\beta} = \Gamma_{\beta\alpha}^{s\gamma}\mathbf{a}_\gamma + B_{\beta\alpha}\xi \tag{4.17}$$

where  $\Gamma_{\beta\alpha}^{s\gamma}$  are the surface Christoffel symbols of second kind

$$\Gamma_{11}^{s1} = \frac{h'h''}{1+h'^2}, \quad \Gamma_{22}^{s1} = -\frac{hh'}{1+h'^2}, \quad \Gamma_{12}^{s2} = \Gamma_{21}^{s2} = \frac{h'}{h} \tag{4.18}$$

the other Christoffel symbols are zero.

The second ground form tangential tensor field  $\mathbf{B} = B_{\alpha\beta}\mathbf{a}^\alpha\mathbf{a}^\beta = B^{\alpha\beta}\mathbf{a}_\alpha\mathbf{a}_\beta$  for an axisymmetric surface is defined as

$$B_{11} = \frac{h''}{(1+h'^2)^{1/2}}, \quad B_{22} = -\frac{h}{(1+h'^2)^{1/2}}, \quad B_{12} = B_{21} = 0 \tag{4.19}$$

Hence, the mean curvature  $H$  is

$$H = \frac{1}{2}\text{tr}\mathbf{B} = \frac{h''}{2}(1+h'^2)^{-3/2} - \frac{1}{2h}(1+h'^2)^{-1/2} \tag{4.20}$$

while the surface covariant derivatives are:

$$\begin{aligned} u_{,\beta}^{s\alpha} &= \frac{\partial u^{s\alpha}}{\partial y^\beta} + \Gamma_{\beta\gamma}^{s\alpha}u^{s\gamma} \\ u_{\alpha,\beta}^s &= \frac{\partial u_\alpha^s}{\partial y^\beta} - \Gamma_{\beta\alpha}^{s\gamma}u_\gamma^s \\ B_{\alpha\beta,\gamma} &= \frac{\partial B_{\alpha\beta}}{\partial y^\gamma} - \Gamma_{\gamma\alpha}^{s\mu}B_{\mu\beta} - \Gamma_{\gamma\beta}^{s\mu}B_{\alpha\mu} \end{aligned} \tag{4.21}$$

For an axisymmetric surface  $v^{s2} = 0$  and  $\partial_{y^2} = 0$ , which leads to the simplified the

calculation:

$$\begin{aligned}
 \nabla_s \mathbf{u}_s &= \frac{\partial u^{s1}}{\partial z} + \frac{h'h''}{1+h'^2} u^{s1} - \frac{hh'' - h'^2 - 1}{h(1+h'^2)^{3/2}} \\
 u_{\alpha,\beta}^s &= \delta_\alpha^1 \delta_1^\beta \frac{\partial u^{s1}}{\partial z} - \Gamma_{\beta\alpha}^{s1} u^{s1} \\
 u_{\alpha,\beta\gamma}^s &= \delta_\alpha^1 \delta_1^\beta \delta_1^\gamma \frac{\partial^2 u^{s1}}{\partial z^2} - \left( \delta_\alpha^1 \Gamma_{\gamma\beta}^{s1} + \delta_1^\beta \Gamma_{\gamma\alpha}^{s1} + \delta_1^\gamma \Gamma_{\beta\alpha}^{s1} \right) \frac{\partial u^{s1}}{\partial z} \\
 &\quad - \delta_1^\gamma \frac{\partial \Gamma_{\beta\alpha}^{s1}}{\partial z} u^{s1} + \left( \Gamma_{\alpha\gamma}^{s\mu} \Gamma_{\beta\mu}^{s1} + \Gamma_{\gamma\beta}^{s\mu} \Gamma_{\mu\alpha}^{s1} \right) u^{s1}
 \end{aligned} \tag{4.22}$$

Replacing all the quantities found in the divergence of surface stress (4.13), and solving at the first order of the interface variable  $h$ , the final expression of  $\nabla_s \tau^s$  is found

$$\begin{aligned}
 \nabla_s \tau^s &= \left\{ (\kappa_s - \mu_s) \left( \frac{\partial^2 u}{\partial z^2} + \frac{\partial_z h}{h^2} v + \frac{1}{h} \frac{\partial v}{\partial z} \right) \right. \\
 &\quad \left. + 2\mu_s \left( \frac{\partial^2 u}{\partial z^2} + \frac{\partial_z h}{h} \frac{\partial u}{\partial z} - \frac{\partial^2 h}{\partial z^2} \frac{\partial v}{\partial z} - \left( \frac{\partial h^3}{\partial z} + \frac{\partial_z h}{h^2} \right) v \right) \right\} \mathbf{a} \\
 &\quad + \left\{ -(\kappa_s - \mu_s) \frac{1}{h} \left( \frac{\partial u}{\partial z} + \frac{v}{h} \right) + 2\mu_s \left( \frac{\partial^2 h}{\partial z^2} \frac{\partial u}{\partial z} - \frac{\partial_z h}{h^2} u - \frac{v}{h^2} \right) \right\} \xi
 \end{aligned} \tag{4.23}$$

where we replaced  $u^{s1} \equiv u$  and  $u_\xi^s = v$  for clarity. Since in the following we are interested to perform linear stability analysis, we limit the calculation of  $\nabla_s \cdot \tau^s$  at the first order.

In the limit of vanishing shear viscosity  $\mu_s = 0$ , the divergence of the surface stress is

$$\nabla_s \tau^s = \kappa_s \left( \frac{\partial^2 u}{\partial z^2} + \frac{v}{h^2} \frac{\partial h}{\partial z} + \frac{1}{h} \frac{\partial v}{\partial z} \right) \mathbf{a} - \kappa_s \frac{1}{h} \left( \frac{\partial u}{\partial z} + \frac{v}{h} \right) \xi \tag{4.24}$$

The constitutive equations relevant to hydrodynamic instability of two-phase flow with shear viscosity founded in § 4.1.2, are initially applied to the case of a viscous thread in a dynamically inert medium. In a second step we will analyze the influence of surface viscosity on the base flow and the stability of two-phase co-axial jet.

## 4.2 Stability of a viscous thread immersed in an inert medium

Let analyze the stability of a viscous thread immersed in a dynamically inert medium. The thread  $\bar{\mathbf{u}} = 0$  is considered infinitely long with a constant height  $h(z) = h_0$ , viscosity  $\mu$ , surface tension  $\gamma$  and dilatation viscosity  $\kappa_s$ , as sketched in figure 4.3. According to the kinematic equation  $\mathbf{u}|_{\partial\Omega} = \mathbf{u}_s$ , therefore in the following for clarity of reading the subscript  $s$  is dropped.

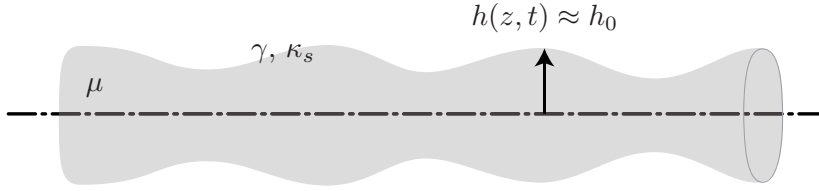


**Figure 4.3** – Domain sketch and notations used in this section

In the limit of vanishing Reynolds number, the governing equations are the Stokes equation with the kinematic condition. The new normal and tangential stress conditions close the problem

$$-p + 2\mu \frac{\partial v}{\partial r} \Big|_{\partial\Omega} = -\gamma \mathcal{C} - \kappa_s \frac{1}{h} \left( \frac{\partial u}{\partial z} + \frac{v}{h} \right) \quad (4.25)$$

$$\mu \left( \frac{\partial u}{\partial r} + \frac{\partial v}{\partial z} \right) \Big|_{\partial\Omega} = \kappa_s \left( \frac{\partial^2 u}{\partial z^2} + \frac{v}{h^2} \frac{\partial h}{\partial z} + \frac{1}{h} \frac{\partial v}{\partial z} \right) \quad (4.26)$$

As for the stability of a viscous thread without surface viscosity (see § 1.4.2), we can use the lubrication approximation to reduce the dimension of the problem. The velocity and pressure field are expanded in Taylor series around  $r = 0$ :

$$\begin{aligned} u(z, r, t) &= u_0(z, t) + u_2(z, t)r^2 + \dots \\ v(z, r, t) &= -\frac{1}{2} \frac{\partial u_0}{\partial z} r - \frac{1}{4} \frac{\partial u_2}{\partial z} r^3 - \dots \\ p(z, r, t) &= p_0(z, t) + p_2(z, t)r^2 + \dots \end{aligned} \quad (4.27)$$

The expanded field are inserted into the Stokes equation and it is solved at the lowest

## 4.2. Stability of a viscous thread immersed in an inert medium

order of  $r$ , giving the reduced Stokes equation:

$$0 = -\gamma \frac{\partial \mathcal{C}}{\partial z} + 3\mu \left( \frac{2}{h} \frac{\partial h}{\partial z} \frac{\partial u_0}{\partial z} + \frac{\partial^2 u_0}{\partial z^2} \right) + \frac{\kappa_s}{2} \left( \frac{1}{h} \frac{\partial^2 u_0}{\partial z^2} - \frac{1}{h^2} \frac{\partial h}{\partial z} \frac{\partial u_0}{\partial z} - h \frac{\partial^4 u_0}{\partial z^4} - h \frac{\partial h}{\partial z} \frac{\partial^3 u_0}{\partial z^3} \right) \quad (4.28)$$

and the reduced kinematic equation

$$\frac{\partial h}{\partial t} = -\frac{1}{2} h \frac{\partial u_0}{\partial z} + \frac{\kappa_s h^2}{8\mu} \frac{\partial^3 u_0}{\partial z^3} \quad (4.29)$$

Linearizing the equations (4.28)-(4.29) around the base flow, the perturbed equations are obtained:

$$0 = \gamma \frac{\partial}{\partial z} \left( \frac{\eta}{h_0} + \frac{\partial^2 \eta}{\partial z^2} \right) + 3\mu \frac{\partial^2 u'}{\partial z^2} + \frac{\kappa_s}{2h_0} \frac{\partial^2 u'}{\partial z^2} - \frac{\kappa_s h_0}{2} \frac{\partial^4 u'}{\partial z^4} \quad (4.30)$$

$$\frac{\partial \eta}{\partial t} = -\frac{1}{2} \frac{\partial u'}{\partial z} h_0 + \frac{\kappa_s h_0^2}{8\mu} \frac{\partial^3 u'}{\partial z^3} \quad (4.31)$$

and the associated dispersion relation is

$$-i\omega = \frac{1}{4\tau_v} \left( 1 - (kh_0)^2 \right) \frac{4 + Bq(kh_0)^2}{6 + Bq(1 + (kh_0)^2)} \quad (4.32)$$

where

$$Bq = \frac{\kappa_s}{\mu h_0} \quad (4.33)$$

is the Boussinesq number and it measures the relative importance of interfacial viscosity to bulk viscous effects.

As for the viscous thread without surface viscosity at the interface, the characteristic timescale is  $\tau_v$ . The instability is then described by three non-dimensional group:  $\omega\tau_v$ ,  $Bq$  and  $kh_0$ . The comparison can be made with the Palierne & Lequeux (1991) exact solution. Palierne & Lequeux (1991), in their work, consider the relation between the wavelength and growth rate of sausage instability of a viscous thread immersed in a quiescent medium, in the limit of vanishing Reynolds number. They analyzed a general viscoelastic fluid and took into account the dynamic properties of the interface stress due to the contamination of surfactants and the capability of the free interface to resist a shear deformation. In their paper, the authors analyzed different cases among which a viscous thread immersed in a viscous medium without surface stress retrieving the Tomotika (1935) equation, and the case of a viscous thread with surface dilatation at

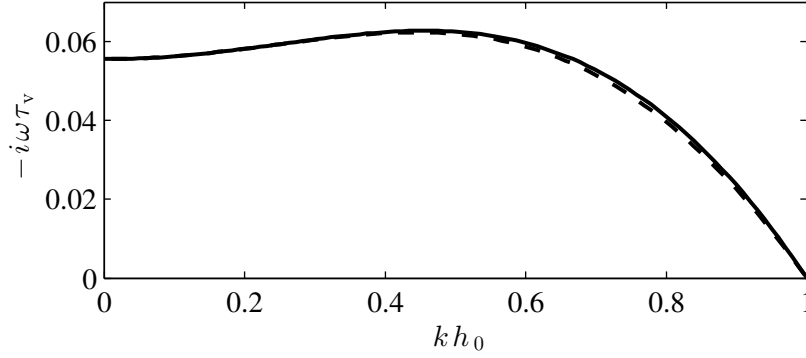


**Figure 4.4** – Dimensionless growth rate  $-i\omega\tau_v$  as function of the dimensionless wavenumber  $kh_0$  for a viscous thread with  $Bq = 12$ , and the lubricated approximation (continuous line) fits well the Palierne & Lequeux (1991) exact solution (dashed line).

the interface, the case of our interest. Palierne & Lequeux (1991) found:

$$-i\omega = \frac{1}{2\tau_v} \frac{(1 - (kh_0)^2) \left( \frac{2}{kh_0} \frac{I_1}{I_0} + Bq \left( kh_0 \left( \frac{I_1}{I_0} - \frac{I_0}{I_1} \right) + 2 \right) \right)}{2 \left( kh_0 \left( \frac{I_0}{I_1} - \frac{I_1}{I_0} \right) - \frac{I_1}{kh_0 I_0} \right) + \frac{I_1}{I_0} \left( kh_0 + \frac{1}{kh_0} \right) Bq} \quad (4.34)$$

The lubrication dispersion relation 4.32 and the exact solution 4.34 are in excellent agreement, as shown in figure 4.4. The lubrication solution slightly overestimate the exact solution, and for  $Bq \rightarrow 0$  the solution of the viscous thread given by Rayleigh (1892) is retrieved.

The dimensionless growth rate  $-i\omega\tau_v$  as function of dimensionless wavenumber  $kh_0$  is plotted for increasing value of the Boussinesq number  $Bq$  in figure 4.5. For  $0 \leq Bq \leq 6$  the most amplified wavenumber occurs at a zero value of the wavenumber  $k_m h_0 = 0$ , while for  $Bq \geq 6$  the maximum growth rate occurs for non zero value of the wavenumber. The variation of the most amplified wavenumber is a monotonous function of  $Bq$ , as shown in figure 4.6, and reaches its maximum  $k_m h_0 \sim 0.65$  for  $\kappa_s \rightarrow \infty$ . The viscous thread remains an ill-posed problem because the translation invariance ( $\omega(k=0) = 0$ ) is broken for any finite value of  $Bq$ . In order to have a well-posed problem, it is necessary to consider the inertial effects of the viscous thread or the viscous effect of the surrounding medium (for details see Palierne & Lequeux (1991)).



## 4.2. Stability of a viscous thread immersed in an inert medium

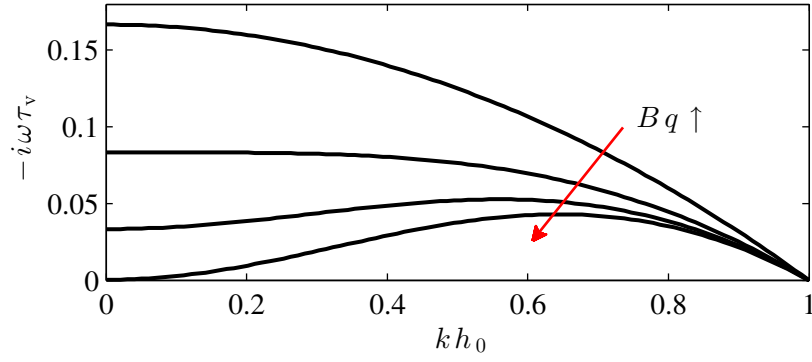


**Figure 4.5** – Dimensionless growth rate  $-i\omega\tau_v$  as function of the dimensionless wavenumber  $kh_0$  for with increasing value  $Bq = \{0, 6, 24, \infty\}$ .

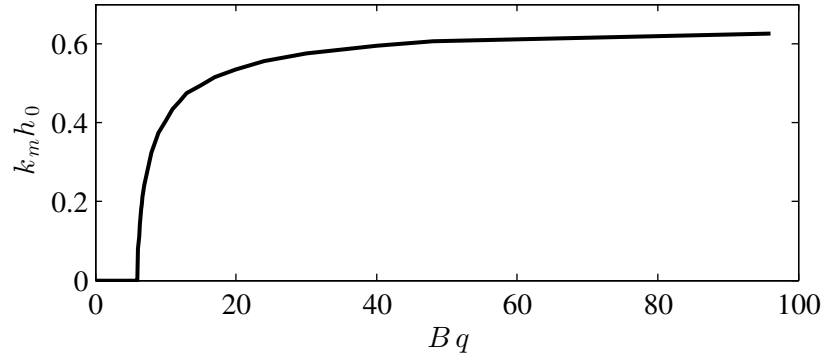


**Figure 4.6** – Most amplified wavenumber  $k_m h_0$  as function of  $Bq$  for a viscous thread.

### 4.3 Stability of a two-phase co-axial jet

Paper: *Influence of surface viscosity on co-axial flows*

## Influence of surface viscosity on co-axial flows

L. Augello<sup>1</sup> and B. Dollet<sup>2</sup> and F. Gallaire<sup>1</sup>

1) LFMI, École Polytechnique Fédérale de Lausanne, CH-1015 Lausanne, Switzerland

2) Institut de Physique de Rennes UMR6251, Université de Rennes - 35042 Rennes, France

Under consideration for publication in Physics of Fluid

**Key words:** instabilities, co-axial flow, surface viscosity

### 4.3.1 Introduction

Bubble and drop generation occurs in many industrial processes, e.g. liquid atomization in engines (Lefebvre (1989); Bayvel & Orzechowski (1993)), ink-jet printing (Wijshoff (2010)), or foaming and emulsification (Drenckhan & Saint-Jalmes (2015)). It often originates from the break-up of threads or jets. Recently, there has been much interest in the production of microdrops and microbubbles of controlled diameter; for instance, in medical imaging, microbubbles are used as ultrasound contrast agents (Quaia (2005)), and their echogenicity crucially depends on their size, which has triggered much interest in producing monodisperse microbubbles (Hettiarachchi, Talu, Longo, Dayton & Lee (2007); Dollet, van Hoeve, Raven, Marmottant & Versluis (2008)). This often requires the use of microfluidic tools, where drops can be produced at T-junctions, in cross flow, or in flow focusing (Anna, Bontoux & Stone (2003); Baroud *et al.* (2010)). In these geometries, there is a coflow of two fluid phases, and drops are formed as the inner phase is pinched off by the outer one. In practice, surfactants are used, to avoid dewetting and the pinning of the inner phase on the confining walls, which suppresses pinching.

Focusing on the coaxial flow of two phases (Cramer *et al.* (2004)), where the inner phase is injected by a nozzle inside a channel where the outer phase is flowing, drops can be created by two mechanisms, referred to as jetting and dripping. In the former case, a long slender jet forms at the nozzle exit, which eventually destabilizes to release drops. In the latter case, drops are formed close to the nozzle exit. These two processes can be rationalized by studying jet instability, but the detachment mechanism differs whether the instability be absolute or convective (Huerre & Monkewitz (1990)). These regimes, and the transition between absolute and convective instability, have been studied in detail by Guillot *et al.* (2007) and Guillot & Colin (2008). Experimentally, they have mapped the formation of drops by either dripping or jetting for various flow rates of both phases. Theoretically, they have performed a stability analysis of the coflow, taking as a base state two embedded parabolic velocity profiles (or bi-Poiseuille flow), yielding

an analytical prediction of the transition between convective and absolute instability in excellent agreement with the experimental transition between dripping and jetting. Global instabilities, accounting for the variation of jet radius after the nozzle exit to accommodate the outer flow, have also been studied (Castro-Hernández, Campo-Cortés & Gordillo (2012), Gordillo *et al.* (2013)).

The influence of surfactants on these coaxial flows has been much less considered, and the boundary condition on the tangential stress has generally been taken as a free-shear condition, thus neglecting any interfacial mechanical resistance. However, it is well known that surfactant adsorption layers at fluid-fluid interfaces can display a finite elasticity and viscosity (Sagis (2011); Fuller & Vermant (2012)), leading to a drastic modification of boundary conditions from free shear to no slip, or to tip streaming (Anna & Mayer (2006)). The influence of surfactants and of surface viscoelasticity has been studied on liquid threads (Palierne & Lequeux (1991); Hansen *et al.* (1999); Timmermans & Lister (2002)) or liquid jets with a quiescent surrounding phase, but not in coflow. The aim of our paper is therefore to study whether surfactants can affect jet stability in a coflow situation.

In the general case, coupling surfactant transport and flow is very complex, because it involves several different processes (Edwards *et al.* (1991)). In general, interfacial stretching or compression induced by bulk flows alters the surface concentration of surfactants, hence the surface tension, which can lead to surface tension gradients (Marangoni effect). This is compensated by surface diffusion and, more importantly for soluble surfactants, by adsorption from the bulk, or desorption to the bulk. These exchanges between the bulk and the interface depend on the subphase bulk concentration, and can be limited either by diffusion or by sorption kinetics. The resulting interfacial stress results from this complex interplay, and only in highly simplified situations, such as in the absence of convection (Lucassen & van den Tempel (1972)), can surface elasticity and viscosity be predicted. In other cases, numerical simulations are required and have been used to study e.g. drop detachment (Jin *et al.* (2006)).

Our aim is not to model these transport processes in detail, but to get a first qualitative insight as to whether surfactants may affect jet instability. Therefore, we have chosen to retain only surface viscosity as a source of mechanical resistance, in the frame of the Boussinesq–Scriven constitutive equation of a Newtonian interface (Scriven (1960); Slattery *et al.* (2007)). This is a major simplification, because it enables to disregard surface and bulk concentration fields, and to solve only for the velocity field. This stringent simplification can be justified two-fold. First, there are situations where the response of the surfactants is indeed dominated by an intrinsic surface viscosity, especially for concentrated solutions at high velocity (Scheid *et al.* (2010)). Second, in more complex situations, surface viscosity can be considered as an effective parameter, which often describes qualitatively correctly the mechanical response of a surfactant adsorbed layer. For instance, in the classical example of the settling of a drop in a surface solution,

surface elastic and viscous effects, coming from very different processes, all have the same qualitative effects to slow down the settling compared to the case of an interface with free shear (Levich (1962)). This approach has been undertaken before in other contexts, such as the formation of free-standing films (van Nierop, Scheid & Stone (2008)) or in dip coating (Scheid *et al.* (2010)).

In Sec. § 4.3.2, we present the governing equations and boundary conditions of the co-axial flow in presence of surface viscosity. In Sec. 4.3.3 we describe the base flow, while in Sec. § 4.3.4 the perturbed flow, with focus on the linearized lubrication analysis (§ 4.3.4.1) and dispersion relation (§ 4.3.4.2). Then, in Sec. § 4.3.5 we analyze the effects of the surface viscosity on the fully developed flow, and in Sec. § 4.3.6 the effects on the region of the nozzle exit. Eventually, in Sec. § 4.3.7 we summarize the results and present the conclusions.

#### 4.3.2 Governing equations and boundary conditions

We consider a cylindrical capillary liquid jet, confined in a cylindrical co-axial pipe of radius  $R$ , as sketched in figure 4.7. The two fluids have the same density  $\rho$  but different viscosity:  $\mu_1$  for the inner flow and  $\mu_2$  for the outer. The inlet velocity of respective stream has a Poiseuille profile with flow rate  $Q_1$  for the inner flow, and  $Q_2$  for the outer. The interface evolves downstream until it reaches the fully developed velocity  $\bar{u}_d$ . In the following, we neglect the inertial effects, as well as gravity, compared to the capillary forces  $\rho u_d^2 \ll \gamma/R$ , where  $\gamma$  is the surface tension.

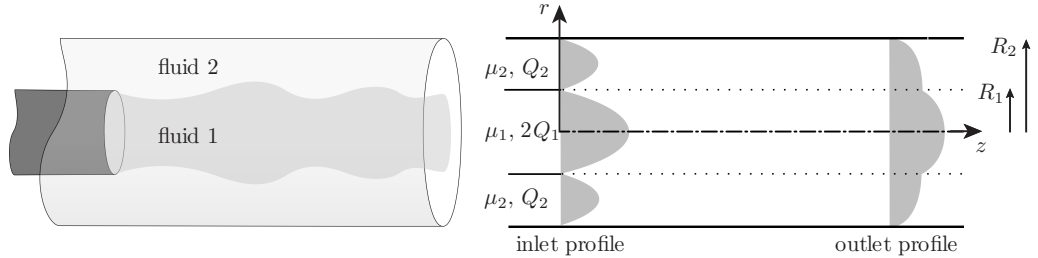


**Figure 4.7** – Flow domain and notations used in the text. On the left a 3D sketch of the core-annular flow, on the right a 2D view of the geometry. The dash-dot (— · —) line is the axisymmetric axis, at the position  $r = 0$ , and the dotted line (··) is the interface, at the position  $r = R_1$ , while the continuous line is the pipe wall at  $r = R_2$ . The inner fluid, with viscosity  $\mu_1$  and flow rate  $Q_1$ , flows in an immiscible fluid with viscosity  $\mu_2$  and flow rate  $Q_2$ .

The governing equation for the fluids are the incompressible Stokes equations in axisymmetric coordinates  $(r, z)$ , scaled with the external pipe radius  $R_2$ , the fully developed interface velocity  $\bar{u}_d$  and the outer viscosity  $\mu_2$ . The flow variables are the velocity  $\mathbf{u}(r, z) = v\mathbf{e}_r + u\mathbf{e}_z$ , the pressure  $p$  and the fluid-fluid interface is defined by

$$r = \pm R_1/R_2 = \pm h_d(z)$$

$$0 = -\nabla p_i + \mu_i \Delta \mathbf{u}_i \quad (4.35)$$

$$\nabla \cdot \mathbf{u}_i = 0 \quad (4.36)$$

The subscripts  $i = \{1, 2\}$  denote the inner and outer flow. The unit normal vector  $\xi$  to the interface pointing towards the outer fluid, the tangential vector  $\mathbf{a}$  and the mean curvature  $\mathcal{C}$  can be written as:

$$\xi = \frac{(1, -\partial_z h)}{(1 + (\partial_z h)^2)^{1/2}} \quad (4.37)$$

$$\mathbf{a} = \frac{(\partial_z h, 1)}{(1 + (\partial_z h)^2)^{1/2}} \quad (4.38)$$

$$\mathcal{C} = -\nabla \cdot \mathbf{n} \quad (4.39)$$

Along the interface, the continuity of tangential and normal stress are imposed at the interface

$$\mathbf{a} \cdot \boldsymbol{\tau} \cdot \mathbf{a} = \mathbf{a} \cdot \nabla_s \boldsymbol{\tau}^s \quad (4.40)$$

$$\xi \cdot \boldsymbol{\tau} \cdot \xi = \xi \cdot \nabla_s \boldsymbol{\tau}^s \quad (4.41)$$

where  $\tau_{ij} = \mu(\partial_{x_i} u_j + \partial_{x_j} u_i) - p \delta_{ij}$  is the stress tensor in the Newtonian liquid bulk,  $\delta_{ij}$  the Kronecker delta, while  $\nabla_s$  is the surface divergence of the constraint tensor at the interface  $\boldsymbol{\tau}^s$ . The surface stress tensor  $\boldsymbol{\tau}^s$  depends from both the surface tension and surface viscosity, and it can be described as

$$\boldsymbol{\tau}^s = \gamma \mathbb{I}_s + (\kappa_s - \mu_s) (\mathbb{I}_s : \mathbb{D}_s) \mathbb{I}_s + 2\mu_s \mathbb{D}_s \quad (4.42)$$

where  $\kappa_s$  and  $\mu_s$  are the surface viscosity (respectively dilation and shear surface viscosity). The unit surface tension  $\mathbb{I}_s = \mathbb{I} - \xi \otimes \xi$  can be written in compact form as:

$$\mathbb{I}_s = \frac{h'^2}{1 + h'^2} (\hat{\mathbf{e}}_r \otimes \hat{\mathbf{e}}_r) + (\hat{\mathbf{e}}_\theta \otimes \hat{\mathbf{e}}_\theta) + \frac{1}{1 + h'^2} (\hat{\mathbf{e}}_z \otimes \hat{\mathbf{e}}_z) + \frac{h'^2}{1 + h'^2} (\hat{\mathbf{e}}_r \otimes \hat{\mathbf{e}}_z + \hat{\mathbf{e}}_z \otimes \hat{\mathbf{e}}_r) \quad (4.43)$$

while  $\mathbb{D}_s = \nabla_s \otimes \mathbf{v}_s$  is the surface rate of strain, with  $\nabla_s = \mathbb{I}_s \cdot \nabla$  the surface gradient and  $\mathbf{v}_s$  the velocity at the interface according to the Slattery *et al.* (2007) notation.

$$\nabla_s = \frac{h'^2}{1 + h'^2} \left( \frac{\partial}{\partial r} + \frac{\partial}{\partial r} \right) \hat{\mathbf{e}}_r + \frac{1}{r} \frac{\partial}{\partial \theta} \hat{\mathbf{e}}_\theta + \left( \frac{h'^2}{1 + h'^2} \frac{\partial}{\partial r} + \frac{1}{1 + h'^2} \frac{\partial}{\partial z} \right) \hat{\mathbf{e}}_z \quad (4.44)$$

Finally the divergence  $\nabla_s \tau^s$  of the viscous constraint at the interface  $\tau^s$  for an axisymmetric problem is define as

$$\begin{aligned} \nabla_s \tau^s = & \left\{ (\kappa_s - \mu_s) \left( \frac{\partial^2 u}{\partial z^2} + \frac{\partial_z h}{h^2} v + \frac{1}{h} \frac{\partial v}{\partial z} \right) \right. \\ & + 2\mu_s \left( \frac{\partial^2 u}{\partial z^2} + \frac{\partial_z h}{h} \frac{\partial u}{\partial z} - \frac{\partial^2 h}{\partial z^2} \frac{\partial v}{\partial z} - \left( \frac{\partial h^3}{\partial z} + \frac{\partial_z h}{h^2} \right) v \right) \Big\} \mathbf{a} \\ & + \left\{ -(\kappa_s - \mu_s) \frac{1}{h} \left( \frac{\partial u}{\partial z} + \frac{v}{h} \right) + 2\mu_s \left( \frac{\partial^2 h}{\partial z^2} \frac{\partial u}{\partial z} - \frac{\partial_z h}{h^2} u - \frac{v}{h^2} \right) \right. \\ & \left. \left. - \gamma \left( \frac{1}{h} - \frac{\partial^2 h}{\partial z^2} \right) \right\} \xi \end{aligned} \quad (4.45)$$

The problem is therefore characterized by four dimensionless parameters:

$$Ca = \frac{\mu_2 u_d}{R_2}, \quad \lambda = \frac{\mu_1}{\mu_2}, \quad h_d = \frac{R_1}{R_2}, \quad Bq = \frac{\kappa_s + 3\mu_s}{\mu_2 R_2} \quad (4.46)$$

where  $Ca$  is the Capillary number,  $\lambda$  is the viscosity ratio,  $h_d$  is the degree of confinement and  $Bq$  is the Boussinesq number. We have constructed  $Bq$  with  $\kappa_s + 3\mu_s$  because, how we will see in the following, this is exactly the combination of dilation and shear viscosity that describes the characteristic length of the base flow adaption.

### 4.3.3 Base flow

We first turn to the description of the base flow solution: this amounts to determine the steady interface location which ensures that the steady Stokes equations are satisfied in each fluid as well as the nullity of the normal velocity component across the interface and the interface stress jump condition. The numerical resolution of this strongly coupled problem requires a dedicated discretization method well-suited to the approximation of all surface differential operators, and has not been, to the author's knowledge, reported in the literature so far.

A first observation is that the classical bi-Poiseuille parallel analytical solution remains a valid solution in presence of surface rheology when streamwise invariance is assumed. The absence of radial velocity and the constance of the tangential velocity ensure indeed that all interfacial viscous jumps vanish, except the interfacial tension term. However, in a real system, the spatial invariance is broken by the inlet condition and the flow needs a certain adaptation length to reach this streamwise invariant solution, referred to as the entry length.

While for pure tensile interfaces, the entry length, i.e. the distance needed for the inlet

velocity profile to smoothly adapt through diffusion to the fully developed profile, is expected to scale with the tube radius in the creeping flow limit, we expect surface viscosity to retard this adaptation and to significantly increase the entry length. Indeed surface viscosity will slow down the acceleration of the interface from its null velocity at the inlet to its nominal fully developed velocity. The resulting separation of scales between this surface rheology induced adaptation length and the tube radius (an hypothesis that will be validated a posteriori) calls for a parallel flow approximation. Let us accordingly assume that the interface remains cylindrical at a streamwise-independent location  $h_d = R_1/R_2$  and consider an approximate base flow solution where radial velocity components are neglected and where surface viscosity effects retard the progressive acceleration of the surface velocity  $\mathbf{v}_s \approx \bar{u}_s(z)\mathbf{e}_z$  from its entry null value to its fully developed value.

Under these assumptions, the solution remains unidirectional and a local bi-Poiseuille-like flow prevails, with the stream-wise velocity defined as:

$$\bar{u}_1 = A_1 (r^2 - h_d^2) + \bar{u}_s \quad (4.47)$$

$$\bar{u}_2 = A_2 (r^2 - h_d^2) + B_2 \log \frac{r}{h_d} + \bar{u}_s \quad (4.48)$$

where the coefficients  $A_{1,2}$  are related to the pressure gradients by  $A_i = \partial_z p_i / (4\mu_i)$ , the coefficient  $B_2$  is related to the no-slip condition  $\bar{u}_2(r=1) = 0$ . The radial velocities are null  $\bar{v}_1 = \bar{v}_2 = 0$  due to the parallel assumption.

The explicit expression of the stress conditions at the interface (4.40)-(4.41) are greatly simplified with the parallel geometry assumption:

$$\mu_1 \frac{\partial \bar{u}_1}{\partial r} - \mu_2 \frac{\partial \bar{u}_2}{\partial r} = (\kappa_s + \mu_s) \frac{\partial^2 \bar{u}_s}{\partial z^2}, \quad (4.49)$$

$$-p_1 + p_2 = -(\kappa_s - \mu_s) \frac{1}{h_d} \frac{\partial \bar{u}_s}{\partial z} - \frac{\gamma}{h_d}, \quad (4.50)$$

which express respectively the continuity of tangential stress and normal stress at the unperturbed interface  $r = h_d$ .

Derivating the normal stress boundary condition with respect to  $z$  and combining with the tangential condition, together with the no-slip condition at the wall and the flow rate conservation, we get a simple ODE for the evolution of the interface velocity  $\bar{u}_s$ :

$$\begin{aligned} \frac{\kappa_s + 3\mu_s}{R_1} \left( - \left( R_2^2 + R_1^2 \right) \log \frac{R_1}{R_2} - R_2^2 + R_1^2 \right) \bar{u}_s''(z) \\ - 2\mu_2 \left( R_2^2 - R_1^2 \right) \bar{u}_s'(z) = \frac{4\mu_2 Q_2}{\pi} \end{aligned} \quad (4.51)$$



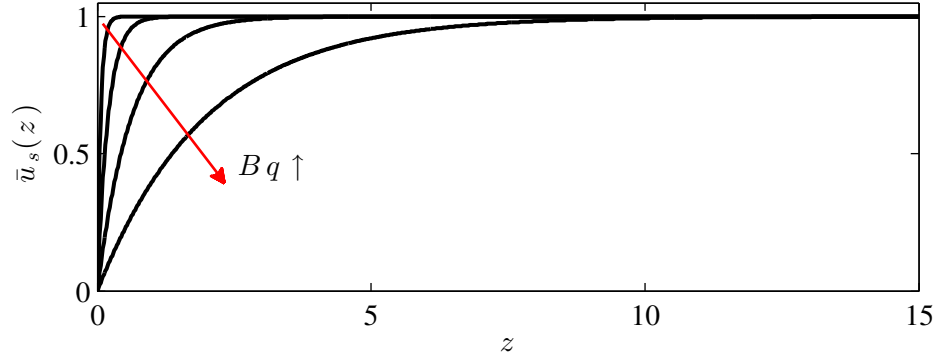


**Figure 4.8** – Interface velocity  $\bar{u}_s$  as function of the coordinate  $z$  for different value of the Boussinesq number  $Bq = \{0.1, 1, 10, 100\}$ , with  $h_d = R_1/R_2 = 0.5$ ,  $\mu = \mu_1/\mu_2 = 0.1$  and terminal velocity  $u_d = 1$ . Increasing the surface viscosity, the interface velocity tends to the fully developed velocity more downstream.

Imposing zero velocity at the inlet  $z = 0$  and a finite velocity for the fully developed flow  $z \rightarrow \infty$ , this equation can be solved to yield

$$\bar{u}_s(z) = \left(1 - e^{-z/L_s}\right) u_d. \quad (4.52)$$

The expression of the interface velocity  $\bar{u}_s(z)$  predicts the same fully developed interface velocity found by Guillot & Colin (2008)  $u_d = \frac{2Q_2}{\pi R_2^2(1-h_d^2)}$ . Figure 4.8 confirms that this terminal velocity does not depend on the surface viscosity. The surface viscosity adaptation length appears naturally as the exponential relaxation length in expression (4.52), in non dimensional terms

$$L_s = \sqrt{\frac{(\kappa_s + 3\mu_s) \left( - (R_2^2 + R_1^2) \log \frac{R_1}{R_2} - R_2^2 + R_1^2 \right)}{2\mu_2 (R_2^2 - R_1^2) R_1}} \quad (4.53)$$

Therefore the order of magnitude of the characteristic length is  $L_s \propto \sqrt{R_2 \mu^* / \mu_2}$  where  $\mu^*$  the effective viscosity is a combination of dilatation and shear viscosity  $\mu^* = (\kappa_s + 3\mu_s)$ . Remembering that the Boussinesq number is defined as  $Bq = (\kappa_s + 3\mu_s) / (\mu_2 R_2)$ , the characteristic length can be rewritten as  $L_s \propto R_2 \sqrt{Bq}$ . The validity of this scaling is confirmed in figure 4.9, where the dependence of the entry length with the interface location is shown. The characteristic length tends towards zero both as  $h_d$  tends towards 0 and 1, because the stress exerted by the outer flow diverges for  $h_d \rightarrow 1$ , whereas the stress exerted by the inner flow diverges for  $h_d \rightarrow 0$ .

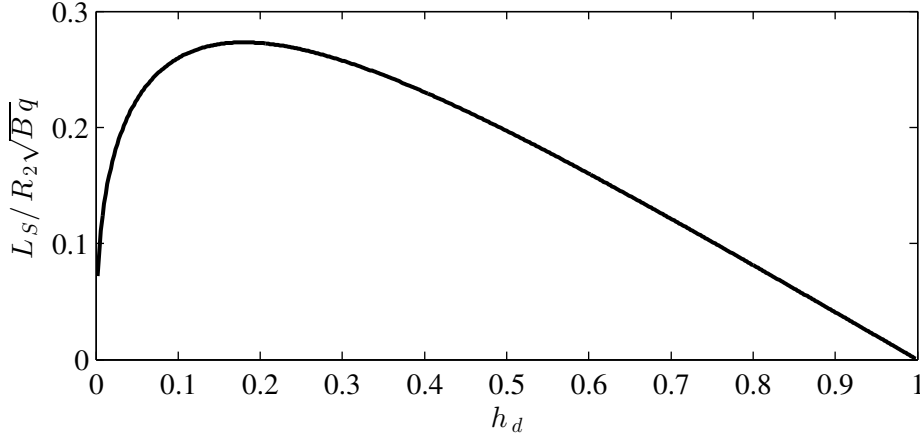


**Figure 4.9** – Dependency of the characteristic length  $L_S$ , rescaled by  $R_2\sqrt{Bq}$ , as function of the radius ratio  $h_d = R_1/R_2$ .

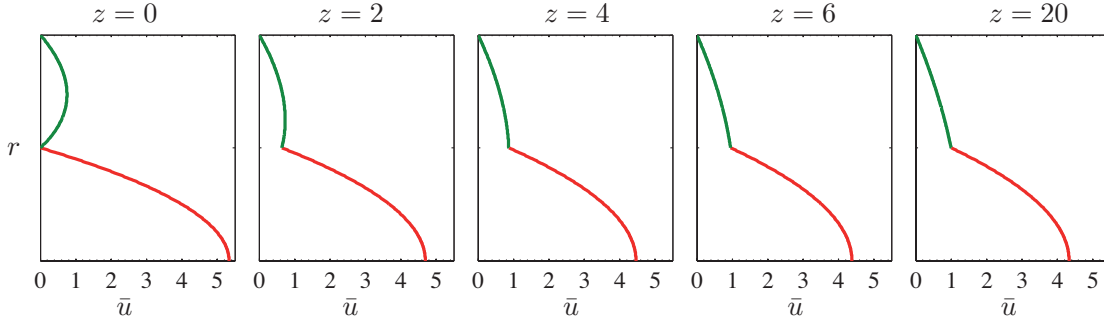


**Figure 4.10** – Base flow evolution for  $\lambda = 0.1$ ,  $Ca = 1$  and  $Bq = 100$  at different location  $z = \{0, 2, 4, 6, 20\}$ . The characteristic length scale is  $L_S = 1.97$ . At  $z = 2$  the interface velocity has reached the 64% of the fully developed velocity ( $\bar{u}_s(z = 2) = 0.6377u_d$ ). While at  $z = 4$  the 87%, and at  $z = 6$  the 95% and finally at  $z = 20$   $\bar{u}_s(z = 20) = u_d$ .

### 4.3.4 Stability analysis

#### 4.3.4.1 Linearized lubrication analysis

Guillot & Colin (2008), Guillot *et al.* (2007) and Herrada *et al.* (2008) have addressed the local stability problem of the core-annular flow, when capillary effects are predominant compare to the inertial forces, in absence of surface viscosity. While Guillot *et al.* use the lubrication assumption, Herrada *et al.* solve the problem analytically. Both approaches lead to similar results. Even though the lubrication approximation is expected to be less accurate, the difference between the results is rather marginal in the parameter space explored, and we will therefore prefer the lubrication approximation.

The parallel stability analysis is made by assuming small disturbances, so that the Stokes

equations can be linearized around the steady state. The flow field is decomposed into a steady and fluctuating part so that velocity field  $\mathbf{u} = \bar{\mathbf{u}} + \varepsilon \mathbf{u}'$ , pressure  $p = \bar{p} + \varepsilon p'$  and interface location  $h = h_d + \varepsilon h'$ , with  $\varepsilon \ll 1$ . We consider the spatio-temporal response of the system to small  $z$ -dependent perturbations.

Besides the no-slip conditions at the wall ( $u'_2|_{r=R_2} = v'_2|_{r=R_2} = 0$ ) and the symmetry condition ( $\partial_r u'_1|_{r=0} = v'_1|_{r=0} = 0$ ), the flow has to satisfy the interfacial boundary conditions: continuity of the velocity  $\mathbf{u}'_1 + h' \partial_r \mathbf{u}_1 = \mathbf{u}'_2 + h' \partial_r \mathbf{u}_2$  at the unperturbed interface and stress continuity conditions. The stress equations (4.40)-(4.41), with the lubrication assumption for a small perturbation assume the explicit form respectively for the tangential and normal stress:

$$\left[ \left[ \mu \frac{\partial u'}{\partial r} + \mu \frac{\partial v'}{\partial z} + \mu h' \frac{\partial^2 \bar{u}}{\partial r^2} - 2\mu \frac{\partial \bar{u}}{\partial z} \frac{\partial h'}{\partial z} \right] \right]_{i=1 \rightarrow 2} = (\kappa_s + \mu_s) \frac{\partial^2 u'}{\partial z^2} + \frac{\kappa_s - \mu_s}{h_d} \frac{\partial v'}{\partial z} + \frac{\kappa_s + \mu_s}{h_d} \frac{\partial \bar{u}_s}{\partial z} \frac{\partial h'}{\partial z} \quad (4.54)$$

$$\begin{aligned} \left[ -p' + 2\mu \frac{\partial v'}{\partial r} - \mu \frac{\partial \bar{u}}{\partial r} \frac{\partial h'}{\partial z} \right]_{i=1 \rightarrow 2} &= -\frac{\kappa_s - \mu_s}{h_d} \frac{\partial u'}{\partial z} + (\kappa_s - \mu_s) \frac{h'}{h_d^2} \frac{\partial \bar{u}_s}{\partial z} - (\kappa_s + \mu_s) \frac{v'}{h_d^2} \\ &\quad + 2\mu_s \frac{\partial^2 h'}{\partial z^2} \frac{\partial \bar{u}_s}{\partial z} - 2\mu_s \frac{\partial h'}{\partial z} \frac{\bar{u}_s}{h_d^2} + (\kappa_s + \mu_s) \frac{\partial^2 \bar{u}_s}{\partial z^2} \frac{\partial h'}{\partial z} + \gamma \left( \frac{h'}{h_d^2} + \frac{\partial^2 h'}{\partial z^2} \right) \end{aligned} \quad (4.55)$$

where the notation  $[\cdot]_{i=1 \rightarrow 2}$  denotes the jump from the inner to the outer flow.

Finally, the linearized kinematic equation imposes, at the unperturbed interface,

$$\frac{\partial h'}{\partial t} = v'_i - \bar{u}_s \frac{\partial h'}{\partial z}. \quad (4.56)$$

The next step in the resolution of our problem is to scale the different terms in the Stokes equations and in the boundary conditions, so as to proceed to a lubrication approximation. There are indeed three length scales to be used to scale the equations: the external jet radius  $R_2 \sim 1$ , the characteristic length of the base flow  $L_S$ , and the characteristic length of the perturbation  $\lambda$ . In the previous section, the analysis of the characteristic length of the base flow has shown that  $1 \ll L_S$ , while the lubrication requires that the perturbation wavelength is much larger than the external radius  $1 \ll \lambda$ . All equation will be solved at the lowest sensible order. We set for the  $z$ -coordinate  $\bar{z} = L_S z^*$ ,  $z' = \lambda z^*$ , for the radial coordinate  $\bar{r} = R_2 r^*$ ,  $r' = R_2 r^*$ , for the axial velocity  $\bar{u} = u_d u^*$ ,  $u' = u_d u^*$ ,

for the radial velocity  $\bar{v} = R_2/L_S u_d v^*$ ,  $v' = R_2/\lambda u_d v^*$ , for the pressure  $p' = P p^*$  and for the surface tension  $\gamma = \Gamma \gamma^*$ . We have already set for the effective viscosity  $\mu^* \sim L_S^2$ .

According to the dominant balance principle, let us set the characteristic length of steady flow and perturbation with the same magnitude order  $1 \ll \lambda \sim L_S$ . With this adimensionalization the equation (4.54)-(4.55) will be slightly simplified:

$$\left[ \left[ \mu \left( \frac{\partial u'}{\partial r} + h' \frac{\partial^2 \bar{u}}{\partial r^2} \right) \right] \right]_{i=1 \rightarrow 2} = (\kappa_s + \mu_s) \frac{\partial^2 u'}{\partial z^2} + \frac{\kappa_s - \mu_s}{h_d} \frac{\partial v'}{\partial z} + \frac{\kappa_s + \mu_s}{h_d} \frac{\partial \bar{u}_s}{\partial z} \frac{\partial h'}{\partial z} \quad (4.57)$$

$$\begin{aligned} \left[ -p' \right]_{i=1 \rightarrow 2} &= -\frac{\kappa_s - \mu_s}{h_d} \frac{\partial u'}{\partial z} + (\kappa_s - \mu_s) \frac{h'}{h_d^2} \frac{\partial \bar{u}_s}{\partial z} \\ &\quad - (\kappa_s + \mu_s) \frac{v'}{h_d^2} - 2\mu_s \frac{\partial h'}{\partial z} \frac{\bar{u}_s}{h_d^2} + \gamma \left( \frac{h'}{h_d^2} + \frac{\partial^2 h'}{\partial z^2} \right) \end{aligned} \quad (4.58)$$

#### 4.3.4.2 Dispersion relation

We make the local mode Ansatz proportional to  $e^{i(kz - \omega t)}$ , where  $k$  is the wavenumber and  $\omega$  the complex angular frequency. The analysis yields a dispersion relation  $\omega = f + ig$  where both frequency  $f$  and growth rate  $g$  can be slip in one term depends on the surface viscosity parameters, and one term does not

$$\omega = F(k) + F_{sv}(k, \mu^*) + i(G(k) + G_{sv}(k, \mu^*)) \quad (4.59)$$

Furthermore, in the frequency we recognize three term: one term  $F_u$  proportional to the velocity of the jet interface, one term  $F_f$  proportional to  $(\partial_r \bar{u}_1 - \partial_r \bar{u}_2)|_{r=h_d}$  due to the flattening of the velocity continuity at the interface, and one term  $F_p$  proportional to  $(\mu_1 \partial_{rr} \bar{u}_1 - \mu_2 \partial_{rr} \bar{u}_2)|_{r=h_d}$  that will vanish for the fully developed flow, when the velocity reaches the bi-Poiseuille profile

$$f = (F_u + F_f + F_p) k + F_{u_{sv}}(k, \mu^*) + F_{f_{sv}}(k, \mu^*) + F_{p_{sv}}(k, \mu^*). \quad (4.60)$$

The frequency terms that do not depend on the surface viscosity are linear in the wavenumber  $k$ , while the terms that depends on the surface rheology are not linear function of the wavenumber (their exact expressions are given in Appendix 1 - § 4.3.8).

Likewise, the growth rate can be split in three terms: the first term  $G_\gamma$  is proportional to the surface tension and does not depend on the surface viscosity,  $G_{\gamma_{sv}}$  is proportional to the surface tension and depends on the surface rheology parameters and  $G_{u_{sv}}$  depends on the surface viscosity and it is proportional to  $\partial_z \bar{u}_s$ . The latter term vanishes when

the the flow reaches the fully developed state.

$$g = G_\gamma(k^2 - h^2 k^4) + G_{\gamma_{sv}}(k, \mu^*) + G_{uz_{sv}}(k, \mu^*) \quad (4.61)$$

The terms  $F_u$ ,  $F_f$  and  $G_\gamma$  are the same elements found by Guillot *et al.* analysis. The contribution  $F_p$  results from taking into account velocity profiles which are not fully developed, while all other terms are associated to surface rheology effects.

While for a jet immersed in an inviscid inert medium the shear viscosity can be neglected (van den Tempel (1977)), this is not necessary anymore true for two-phase flow. With this limitation in mind the results of the local stability will still be given neglecting  $\mu_s$  with respect to  $\kappa_s$ , in first instance. Then the effects of the shear viscosity will be introduced and discussed.

#### 4.3.5 Effect of surface rheology on the temporal and spatio-temporal stability of the fully developed flow

In this section, we first consider the effect of surface dilatation viscosity on the linear stability properties of the fully developed core-annular velocity profile under the assumption of parallel flow. For conciseness the analysis is here reported only for an interface location  $h = 0.5$  and for three representative viscosity ratios,  $\lambda = 0.1, 1, 10$ . We first turn to the temporal stability analysis: a real wavenumber  $k$  is imposed and one looks for the complex eigenvalues  $\omega(k)$ . Figure 4.11 shows the effect of an increasing surface dilatation viscosity (of non dimensional values  $Bq = 1, 10, 100$  and  $\mu_s = 0$ ) onto both the frequency and the growth-rate of the dispersion relation.

##### 4.3.5.1 Temporal stability

Figure 4.11 (a,c,e) shows that an increase in the surface dilatation viscosity  $\kappa_s$  increases the frequency  $f$ . This effect is more pronounced when the outer flow is more viscous than the inner flow  $\lambda < 1$  (fig. 4.11a), while the addition of surface viscosity does not have any effect on the frequency when the two fluids have the same viscosity  $\lambda = 1$  (fig. 4.11c).

As far as the temporal growth-rate is concerned, the addition of surface viscosity is seen to have an overall stabilizing effect, as seen in figure 4.11 (b,d,f). Interestingly, the cut-off wavenumber is not affected, it is solely dictated by the interface location  $k_c = 1/h_d$ . As already noticed on the real part of the dispersion relation, the strongest effect of the surface rheology are observable when the inner flow is less viscous than the outer flow  $\lambda < 1$  (fig. 4.11b).

Now we fix the value of the dilatation viscosity  $\kappa_s = 100$  and let the shear viscosity  $\mu_s$

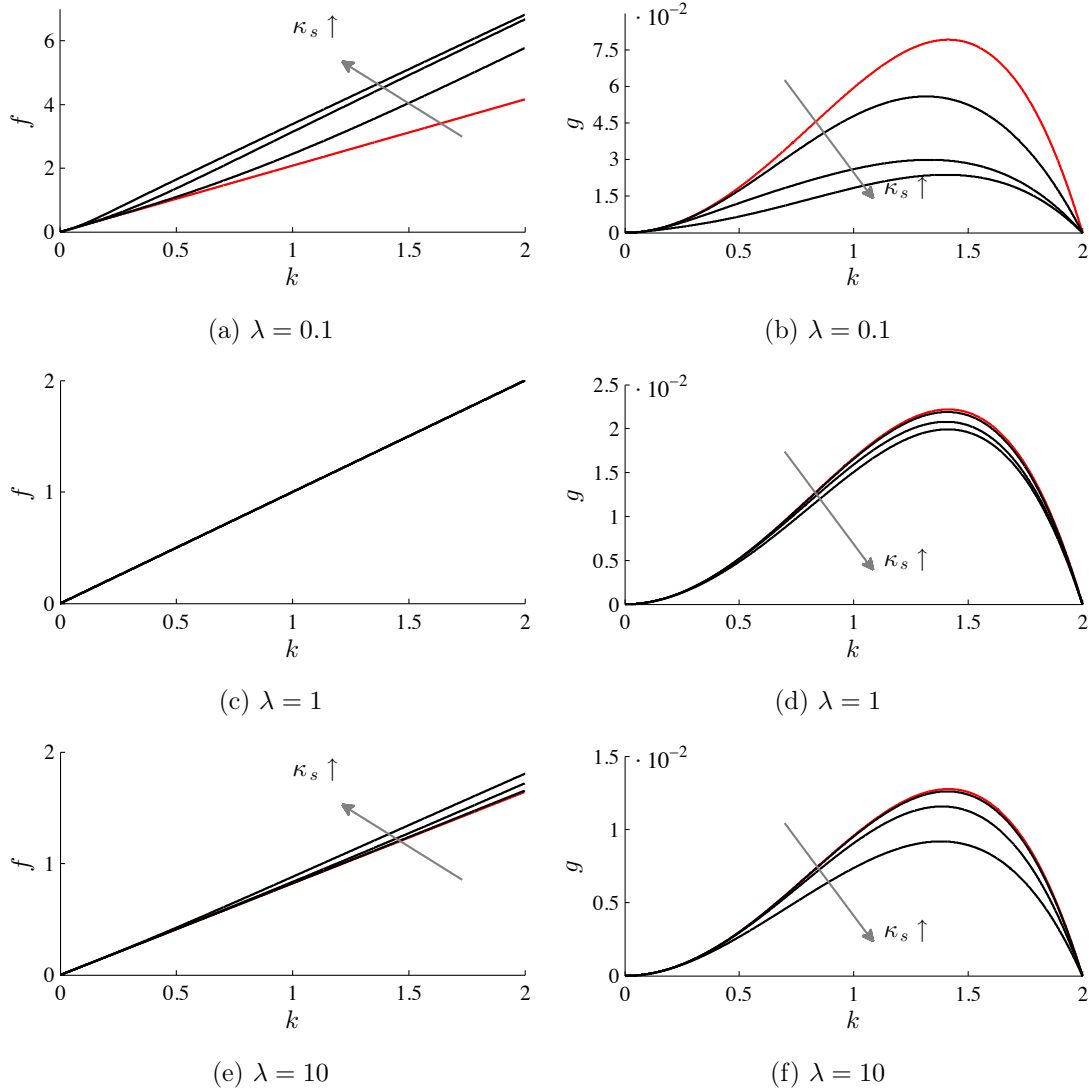


**Figure 4.11** – Spatio-temporal stability analysis for a cross section of fully developed flow with interface position  $h = 0.5$ , Capillary number  $Ca = 1$ , for different value of viscosity ratio  $\lambda = \{0.1, 1, 10\}$  and surface dilatation viscosity  $\kappa_s = \{0, 1, 10, 100\}$ . On the left column the frequency  $f$ , and on the right column the growth rate  $g$  as function of the wavenumber  $k$ .

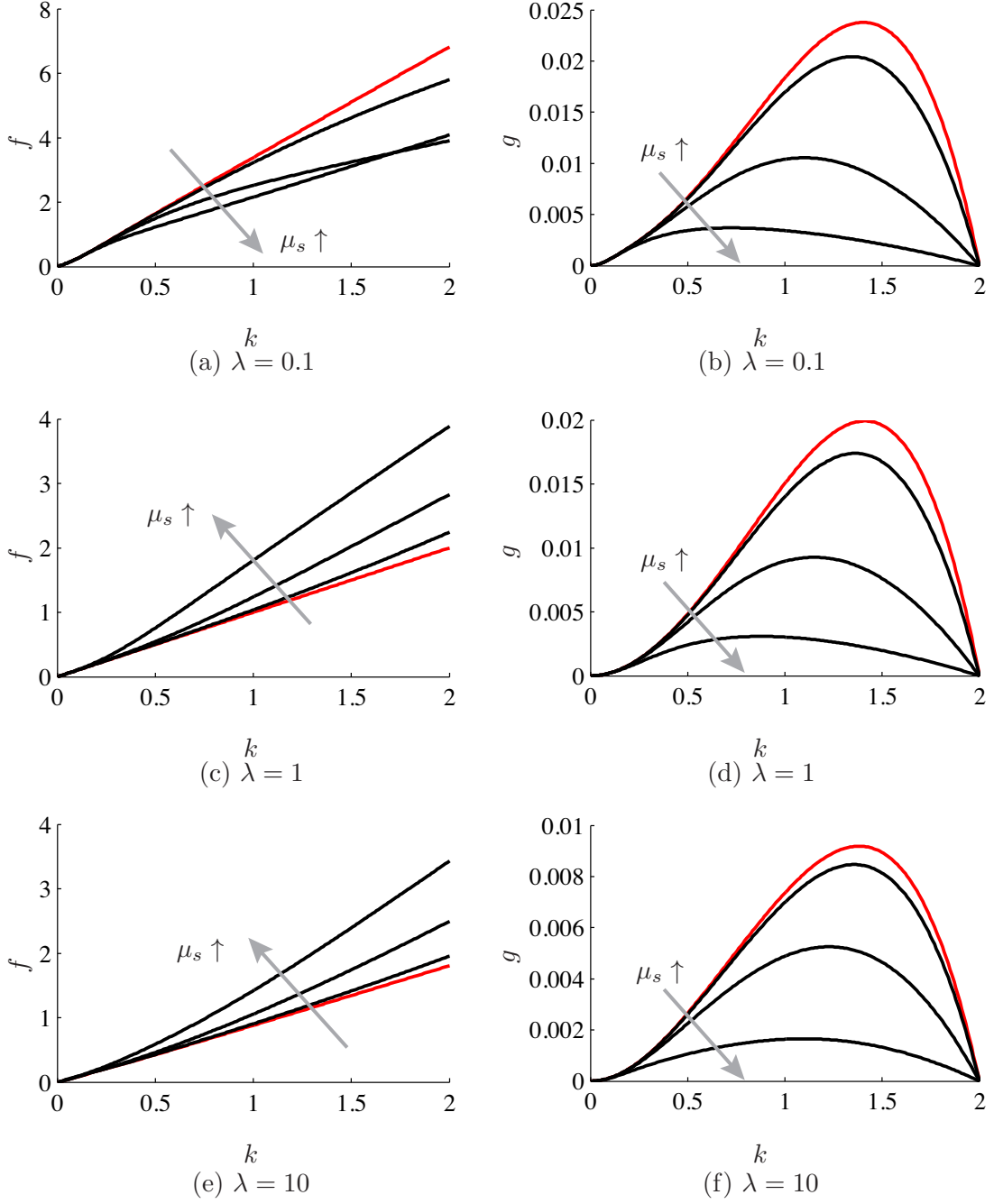


**Figure 4.12** – Spatio-temporal stability analysis for a cross section of fully developed flow with interface position  $h = 0.5$ , Capillary number  $Ca = 1$ , for different value of viscosity ratio  $\lambda = \{0.1, 1, 10\}$ , surface dilatation viscosity  $\kappa_s = 100$  and increasing value of the shear viscosity  $\mu_s = \{0, 1, 10, 100\}$ . On the left column the frequency  $f$ , and on the right column the growth rate  $g$  as function of the wavenumber  $k$ .

vary. As for the dilation viscosity, also the shear viscosity has a stabilizing effect on the temporal growth-rate (fig. 4.12 b,d,f). Again the cut-off  $k_c = 1/h_d$  only depends on the interface position and not the surface viscosity.

An increase of the shear viscosity  $\mu_s = 0, 1, 10, 100$  corresponds to an increase of the frequency only if  $\lambda \geq 10$  (fig. 4.12 c,e). In contrast when the outer flow is more viscous than the inner flow ( $\lambda = 0.1$ ), an increase of the shear viscosity  $\mu_s$  decreases the frequency  $f$  (fig. 4.12 a).

### 4.3.5.2 Spatio-temporal stability

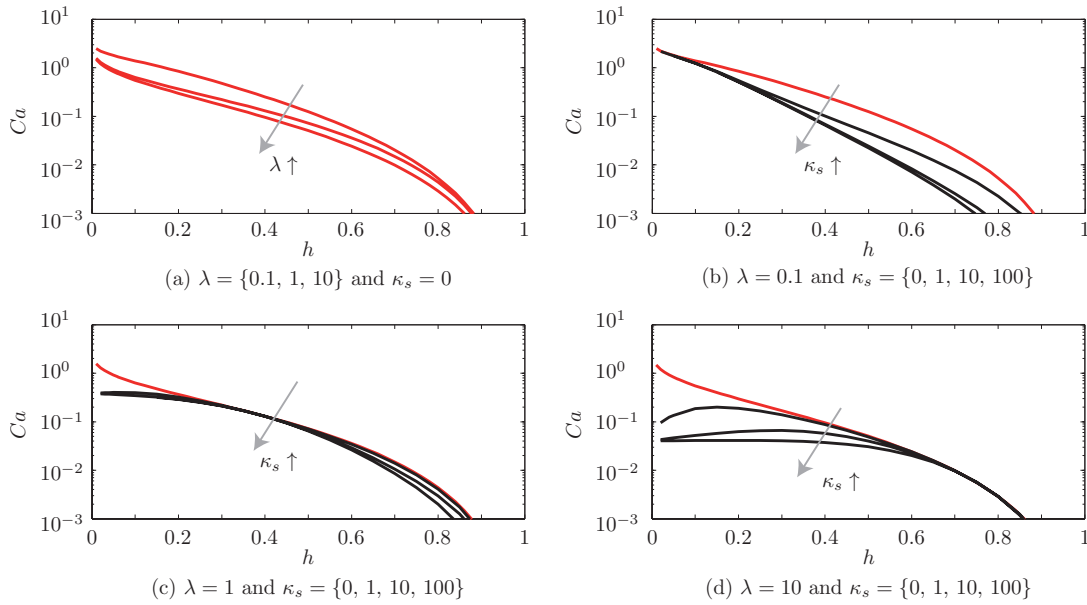


**Figure 4.13** – Phase diagram of the instability in the  $(h, Ca)$  plane for different value of viscosity ratio  $\lambda = \{0.1, 1, 10\}$  and surface dilatation viscosity  $\kappa_s$ . The red lines correspond to the co-axial flow analysis without surface viscosity, while the black lines correspond to different value of  $\kappa_s = \{1, 10, 100\}$  with  $\mu_s = 0$ . Above the lines, the system is convectively unstable, while below is absolutely unstable.

Since the growth rate is a nonlinear function of the wavenumber, the spatio-temporal growth and propagation of the perturbations occurs in dispersive way. An unstable wavepacket grows and travels within two limiting velocities ranging between  $v^-$  characterizing the receding edge and  $v^+$ , which characterizes the leading edge. Of particular importance is the sign of  $v^-$ , which determines if the flow is convectively or absolutely unstable. If  $v^- > 0$  all unstable perturbations are convected downstream making the jet convectively unstable, while if  $v^- < 0$  there are unstable perturbations that travel backwards and the flow is absolutely unstable.

Guillot *et al.* (2007) predicted that the transition from an absolute to a convective



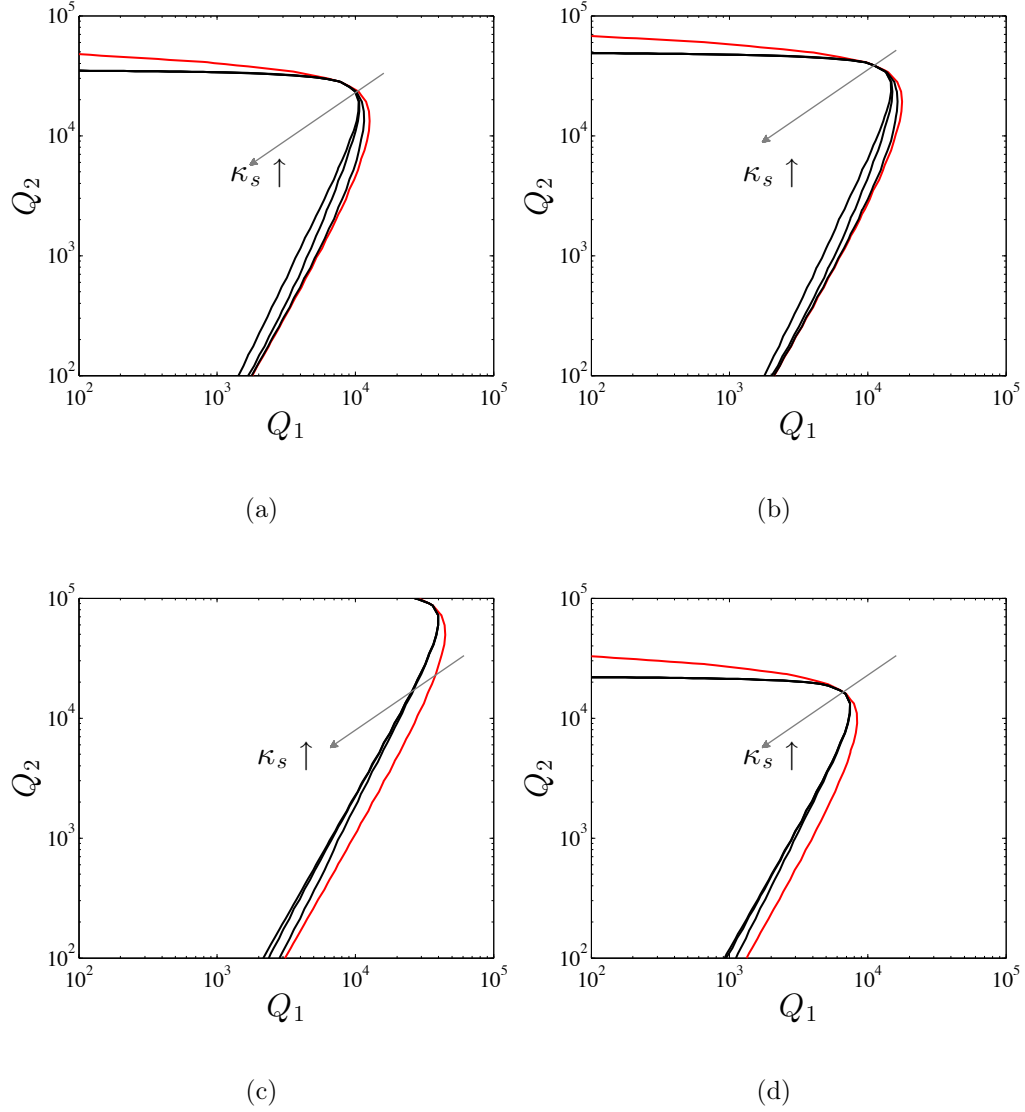


**Figure 4.14** – Dynamic behavior in the  $(Q_1, Q_2)$  plane and A/C transition. The red lines correspond to the co-axial flow analysis without surface viscosity, while the black lines correspond to increasing value of  $\kappa_s$ . Above the lines, the system is convectively unstable, while below is absolutely unstable. For the figure (a) and (b):  $\mu_1 = 0.055 \text{ Pa s}$ ,  $\mu_2 = 0.235 \text{ Pa s}$  and  $\gamma = 24 \text{ mN/m}$  with  $R_2 = 275 \mu\text{m}$  for (a) and  $R_2 = 435 \mu\text{m}$  for (b). For (c) and (d)  $\mu_1 = 1 \text{ mPa s}$ ,  $\mu_2 = 3 \text{ mPa s}$  and  $R_2 = 275 \mu\text{m}$  with  $\gamma = 12 \text{ mN/m}$  for (c) and  $\gamma = 0.12 \text{ mN/m}$  for (d). The flow rates are expressed in  $[\mu\text{L/h}]$ .

instability (A/C transition) depends on a critical value of capillary number  $Ca = \mu_2 u_D / \gamma$ . This critical  $Ca$  was found to well predict the transition from the dripping to the jetting regimes. With a dispersion relation of the form  $\omega = Fk + G((k/k_c)^2 - (k/k_c)^4)$ , the receding edge velocity is determined from the equality of the envelope velocity and group velocity  $\omega_i/k_i = \partial_{k_i} \omega_i$  and the condition maximal growth rate  $\partial_{k_r} \omega_i = 0$  (van Saarloo

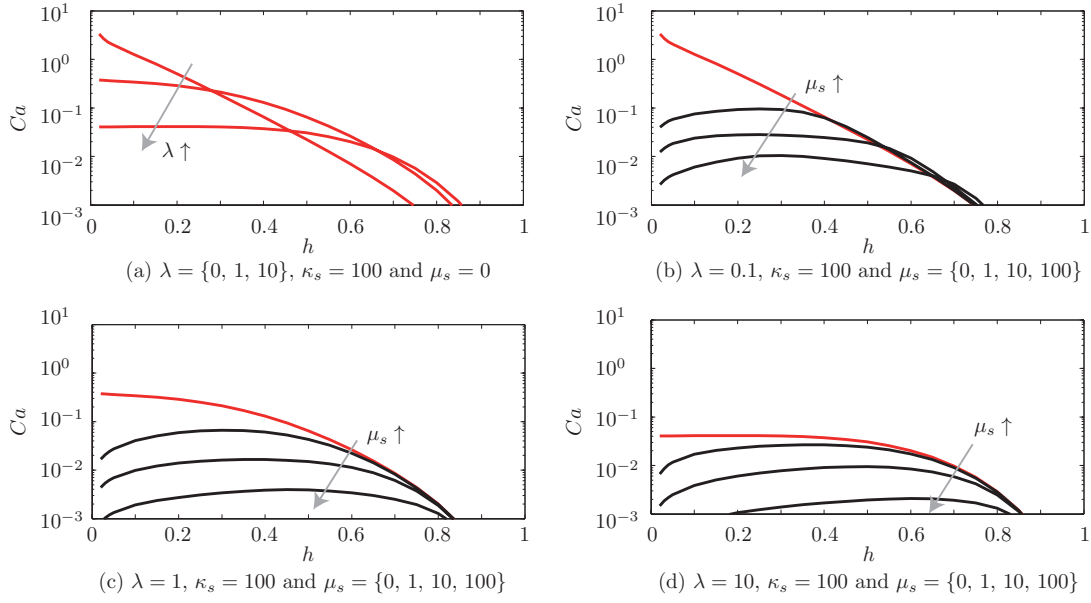


**Figure 4.15** – Phase diagram of the instability in the  $(h, Ca)$  plane for different value of viscosity ratio  $\lambda = \{0.1, 1, 10\}$ , fixed value of surface dilatation viscosity  $\kappa_s = 100$  and increasing shear viscosity  $\mu_s$ . The red lines correspond to the co-axial flow analysis without surface viscosity, while the black lines correspond to different value of  $\mu_s = \{1, 10, 100\}$ . Above the lines, the system is convectively unstable, while below is absolutely unstable.

(1988)):

$$v^- = F - G \left( \frac{5 + \sqrt{7}}{12} \frac{1}{k_c^2} - \frac{5 + \sqrt{7}}{36} \frac{1}{k_c^4} \right) k_c \sqrt{\frac{24}{\sqrt{7} - 1}} \quad (4.62)$$

The A/C transition is reached when  $v^- = 0$  and it can easily plotted as function of two dimensionless parameters: the interface position  $h$  and the capillary number  $Ca = \mu_2 u_D / \gamma$ . As seen in Figure 4.13, the  $(h, Ca)$ -plane is separated into an convectively unstable region above the A/C marginal curve at large  $Ca$  and  $h$  and a absolutely unstable region at small  $h$  and small  $Ca$ .

Let us now investigate the influence of surface viscosity on the spatio-temporal properties of the fully developed co-axial jet velocity profile. Since the addition of surface dilatation viscosity decreases the growth-rate and increases the frequency, the combined effect of less growth and more advection is expected to make the flow more convectively unstable.

This is confirmed by figure 4.13: for the three chosen values of the viscosity ratio, an increase in  $\kappa_s$  is always seen to decrease the region of absolute instability at the expense of the convective region. The A/C transition can be also plotted against the flow rates  $Q_1$  and  $Q_2$  for realistic values of the parameters of microfluidic devices. Figure 4.14 confirms the above results by comparing the A/C transition curve in absence of viscosity. When

increasing  $\kappa_s$ , the convectively unstable region increases. The figure compare the Guillot *et al.* (2007) predictions (red lines) to the same co-axial flow with surface viscosity (black lines) obtained for different value of viscosity ratios, external radii and capillary numbers.

Let us now analyze the influence of the shear viscosity on the A/C transition for three choose representative value of viscosity ratio  $\lambda = 0.1, 1, 10$  and one choose value of dilation viscosity  $\kappa_s = 100$ . As we have seen in the temporal stability, for  $\lambda \geq 1$  an increase in  $\mu_s$  corresponds to a decrease of the absolutely unstable region and an increase of the convectively unstable region (fig. 4.15 c,d). For  $\lambda = 0.1$ , an increase in  $\mu_s$  corresponds instead to an increase of the convective region for small value of confinement degree, for large value of the confinement  $h \lesssim 1$  it yields a decrease of the convective region, while the flow becoming more absolutely unstable.

#### 4.3.6 Effect of surface viscosity on the stability of the overall flow

In the following, we study the influence of surface viscosity in the co-axial flow in all its complexity: we proceed to a weakly non parallel analysis of the flow at different streamwise locations ranging from the inlet to the region where the flow has reached the fully developed state, via the entry region. As discussed in section § 4.3.3, this region has, for pure Stokes flow without the surface rheology, a length which scales like the external radius  $l \sim R_2$  and the flow quickly reaches the fully developed state. This lack of separation of scale between the streamwise base flow evolution and the characteristic instability scale outrules the quasi-parallel assumption. In contrast, with the addition of surface viscosity at the interface, we have shown in section § 4.3.3 that the characteristic length of the transition region  $L_S \propto \sqrt{R_2 \mu^* / \mu_2}$  becomes large when the Boussinesq number is large.

With the base flow evolving over a lengthscale which is much larger than the typical unstable wavelengths, it becomes relevant to conduct a weakly non parallel stability analysis: the base flow is chopped into slices, as it evolves downstream and the parallel spatio-temporal instability analysis is extensively repeated on a slice by slice basis. With the flow evolving slowly spatially, a local stability analysis can be conducted considering the flow prevailing at any streamwise station as strictly parallel and determining the local dispersion relation, as described in section 4.3.4. While the absolute/convective analysis can be conducted using the full dispersion relation (Herrada *et al.* (2008)), we have followed a different approach which consists of approximating the temporal dispersion relation by  $\omega \sim Fk + G((k/k_c)^2 - (k/k_c)^4)$  so as to immediately get the effect of the surface viscosity onto the A/C convective properties of flow, within less than 5% error. Approximating the dispersion relation as  $\omega(k, z) \sim F(z)k + G(z)((k/k_c)^2 - (k/k_c)^4)$ , it is straightforward to determine the absolute/convective of the flow prevailing at a given station  $z$ .

The A/C transition is plotted in fig. 4.16 as function of the  $z$ -coordinate and the capillary number, for a fixed interface position and three fixed value of the viscosity ratio. While the flow becomes eventually more convectively unstable once it reaches its fully developed profile, the surface viscosity creates an absolute region at the inlet, that is expected to promote droplet formation. The length of the absolute region increases when  $\kappa_s$  increases, in accordance with the base flow description provided in section § 4.3.3. The effect of  $\kappa_s$  is more pronounced when the two fluid have the same viscosity (fig. 4.16c) due to an increase in the entry length.

Interestingly the smallest absolute region is obtained for capillary numbers not far from one. When the capillary number is too small the flow becomes absolutely unstable throughout the domain, while when the capillary number becomes large, the absolute region extends.

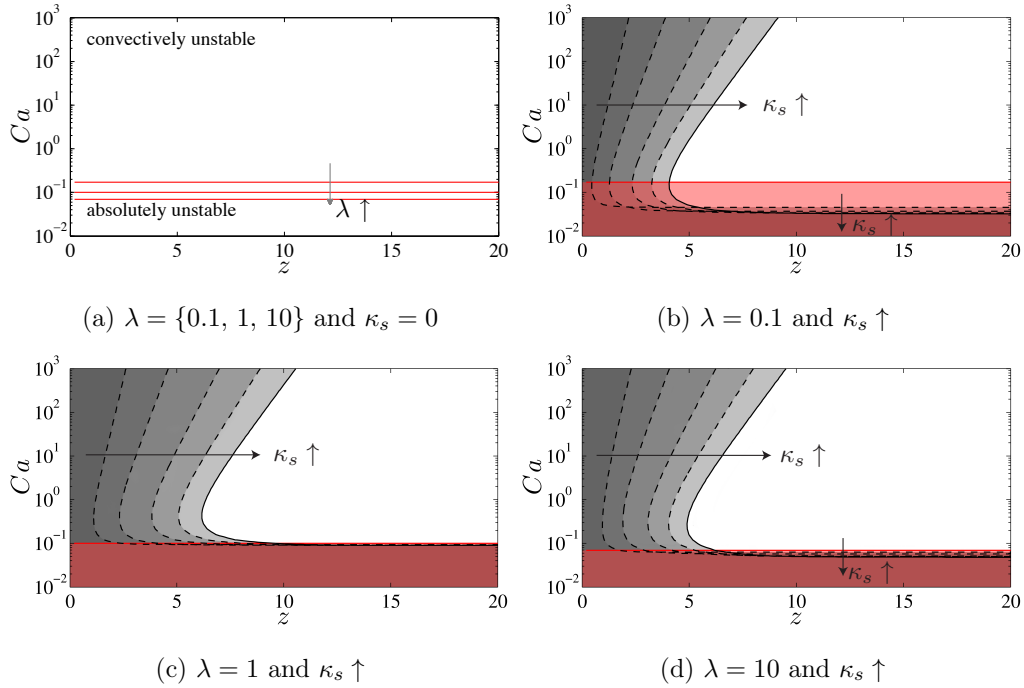


**Figure 4.16** – A/C transition in the  $(z, Ca)$  plane for different value of viscosity ratio  $\lambda = \{0.1, 1, 10\}$  and surface dilatation viscosity  $\kappa_s = \{10, 25, 50, 75, 100\}$ , while the interface position is set  $h = 0.5$ . The red lines correspond to the co-axial flow analysis for  $\kappa_s = 0$ . While the black lines correspond for increasing value of  $\kappa_s$ . The shaded region is the absolute region, convective otherwise.

To better understand the physical origin of this absolutely unstable flow region, we now fix the capillary number in addition to the interface position and the viscosity ratio. It is then possible to analyze the co-axial flow for different location along  $z$ . In the first instance we set the capillary number such that the flow without surface viscosity

will result convectively unstable  $Ca = 1$  (fig. 4.17). If we include surface rheology, the convectively unstable character of the fully developed flow is reinforced, but the inlet region displays an absolute region. Proceeding downstream, one can observe a competition between the advection resulting from the Doppler effect associated to the almost linear frequency dependence with the wavenumber and the spreading of the unstable wave packet associated to the unstable wavenumber band. As  $z$  is increased, the slope of  $f(k)$  decreases slower than the maximum growth rate, causing the change of  $v^-$  sign. The flow turns convectively unstable at a certain distance from the inlet.

We can observe a similar behavior if we consider a co-axial flow with the same flow parameters, but with lower capillary number  $Ca = 0.1$  (fig. 4.18). In this configuration the case  $\kappa_s = 0$  is absolutely unstable. If we add surface viscosity  $\kappa_s = 100$ , the flow presents an absolutely unstable initial region before it becomes convective.

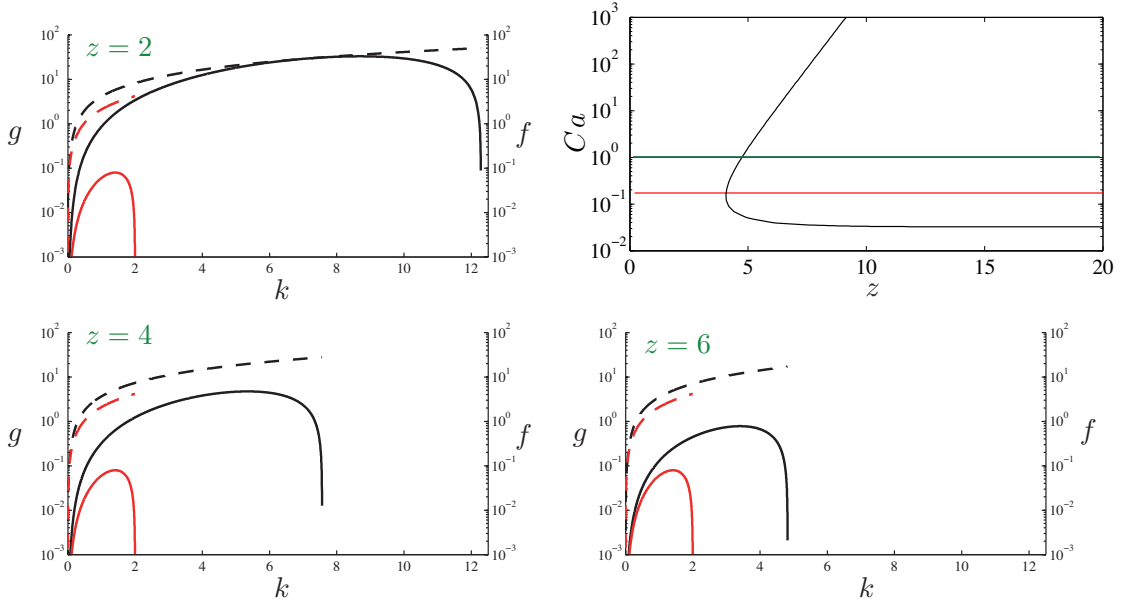


**Figure 4.17** – A/C transition and spatio temporal analysis for  $h = 0.5$ ,  $\lambda = 0.1$  and  $Ca = 1$  (green line). The red line is plotted for  $\kappa_s = 0$ , while the black line for  $\kappa_s = 100$ . The spatio - temporal analysis is performed at three different location  $z = \{2, 4, 6\}$ . The characteristic length scale is  $L_S = 1.97$ .

This shows that the addition of surface viscosity considerably changes the stability predictions of the flow. Because of the slow base flow evolution towards the fully developed flow, an absolutely unstable region opens whether or not the fully developed flow is absolutely unstable. The somewhat peculiar situation arises where the fully developed flow is absolute in absence of surface viscosity, convective once the latter is introduced, but the flow becomes absolutely unstable over a noticeable portion of its entry region.

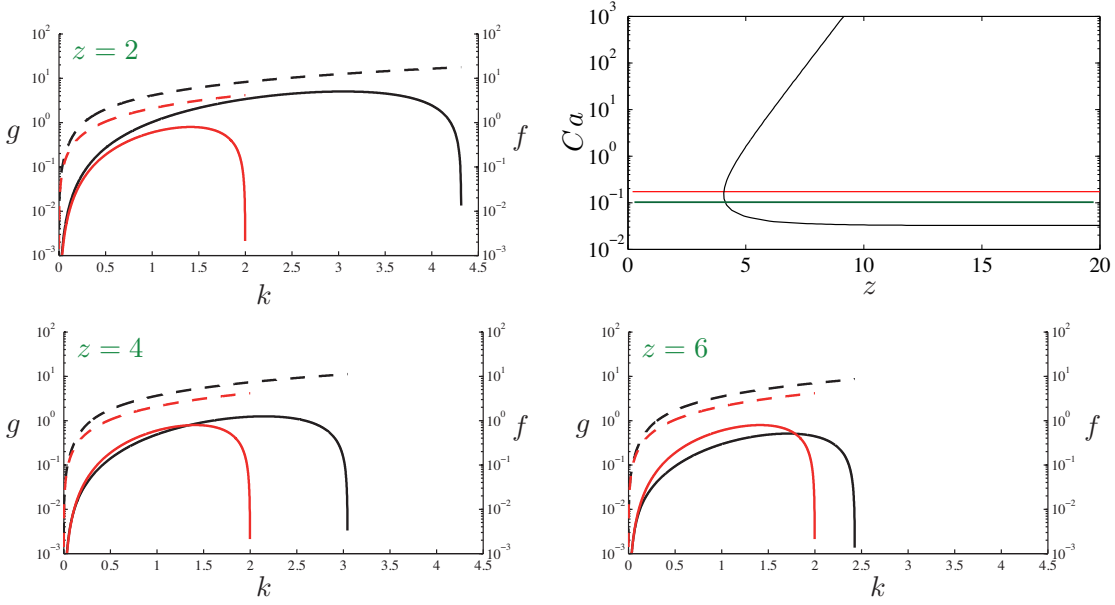


**Figure 4.18** – A/C transition and spatio-temporal analysis for  $h = 0.5$ ,  $\lambda = 0.1$  and  $Ca = 0.1$  (green line). The red line is plotted for  $\kappa_s = 0$ , while the black line for  $\kappa_s = 100$ . The spatio-temporal analysis is performed at three different locations  $z = \{2, 4, 6\}$ . The characteristic length scale is  $L_S = 1.97$ .

#### 4.3.7 Discussion and conclusion

The implications of the results obtained in the last section are the following. According to recent development in global mode theories (see Chomaz (2005) for a review), a spatially evolving flow will become globally unstable once it has a sufficiently large pocket of absolute instability. While the required finite extension remains problem specific, one can expect that as soon as the surface viscosity becomes large enough, the flow will turn globally unstable, with a substantial portion of the entry region becoming globally unstable. In this case, dripping would be observed independently of the capillary number.

There are several natural continuations of this work that could help confirming this prediction. On one hand, careful experiments should be conducted using surfactants which provide a large viscosity to the interface. On the other hand, we plan to conduct global stability calculations including both (i) the determination of the base flow and its interface deflection, relaxing the parallel interface condition used in the present study (ii) global stability calculations relaxing the weakly non parallel stability analysis approach. These two steps require the development of dedicated numerical methods. A last approach would be to directly simulate the governing Stokes equations, including the full nonlinear conditions prevailing at the interface, i.e. the kinematic equation as well as the complete interfacial stress jump accounting for the surface dynamics.

### 4.3.8 Appendix 1: Normal mode expansion

Linearized Stokes equation and continuity equation around the steady state, with the lubrication assumption:

$$\frac{1}{r}\partial_r(rv) + \partial_z u = 0 \quad (4.63)$$

$$0 = -\partial_r p \quad (4.64)$$

$$0 = -\partial_z p + \mu \frac{1}{r} \partial_r(r \partial_r u) \quad (4.65)$$

Integrating the continuity equation (4.63) and the  $z$ -momentum (4.65), using the local normal mode decomposition  $u' = \hat{u}(r)e^{i(kz-\omega t)}$ ,  $p' = \hat{p}(r)e^{i(kz-\omega t)}$  and  $h' = \hat{h}(r)e^{i(kz-\omega t)}$ , we obtain the velocity field:

$$\hat{u}_j(r) = \frac{ik}{4\mu_j}(\hat{p}_j r^2 + C_j \log r + D_j) \quad j = 1, 2 \quad (4.66)$$

$$\hat{v}_j(r) = \frac{k^2}{4\mu_j} \left( \frac{\hat{p}_j r^3}{4} + \frac{C_j}{2} \left( r \log r - \frac{r}{2} \right) + \frac{D_j r}{2} + \frac{E_j}{r} \right) \quad j = 1, 2 \quad (4.67)$$

where  $C_j, D_j, E_j$  are constant of integrations (for the symmetry condition  $C_1 = E_1 = 0$ ).

Boundary conditions with the normal mode decomposition:

- No-slip conditions

$$\hat{p}_2 R_2^2 + C_2 \log R_2 + D_2 = 0 \quad (4.68)$$

$$\frac{\hat{p}_2 R_2^3}{4} + \frac{C_2}{2} \left( R_2 \log R_2 - \frac{R_2}{2} \right) + \frac{D_2 R_2}{2} + \frac{E_2}{R_2} = 0 \quad (4.69)$$

- Continuity of the velocity at the interface

$$\left( \hat{p}_1 R_1^2 + D_1 \right) - \frac{2i\partial_z \bar{p}}{k} R_1 \hat{h} = \lambda \left( \hat{p}_2 R_1^2 + C_2 \log R_1 + D_2 \right) - \lambda \frac{2i\partial_z \bar{p}}{k} R_1 \hat{h} \quad (4.70)$$

$$\hat{p}_1 R_1^3 + 2D_1 R_1 = \lambda \left( \hat{p}_2 R_1^3 + 2C_2 \left( R_1 \log R_1 - \frac{R_1}{2} \right) + 2D_2 R_1 + 4\frac{E_2}{R_1} \right) \quad (4.71)$$

- Kinematic equation

$$-i\omega\hat{h} = \frac{k^2}{4\mu_1} \left( \frac{\hat{p}_1 R_1^3}{4} + \frac{D_1 R_1}{2} \right) - ik\bar{u}_s \hat{h} \quad (4.72)$$

- Tangential stress

$$\begin{aligned} & \left( 2R_1 + \frac{3}{4}\kappa_s k^2 \frac{h_d^2}{\mu_1} \right) \hat{p}_1 - 2R_1 \hat{p}_2 + \frac{\kappa_s k^2}{2\mu_1} D_1 - \frac{1}{R_1} C_2 \\ & - \frac{4i}{k} \left( \mu_1 \frac{\partial^2 \bar{u}_1}{\partial r^2} - \mu_2 \frac{\partial^2 \bar{u}_2}{\partial r^2} \right) \hat{h} - \frac{4\kappa_s}{R_1} \frac{\partial \bar{u}_s}{\partial z} \hat{h} = 0 \end{aligned} \quad (4.73)$$

- Normal stress

$$\begin{aligned} & \left( -1 - \frac{3k^2 R_1}{16\mu_1} \right) \hat{p}_1 + \hat{p}_2 - \frac{k^2}{8\mu_1 R_1} D_1 + \\ & -\gamma \left( \frac{1}{R_1^2} - k^2 \right) \hat{h} - \frac{\kappa_s}{R_1^2} \frac{\partial \bar{u}_s}{\partial z} \hat{h} + 2\mu_s \frac{ik}{R_1^2} \bar{u}_s \hat{h} = 0 \end{aligned} \quad (4.74)$$

We can write the boundary conditions in matrix form:  $A\phi = 0$ , where the unknown vector  $\phi = (\hat{p}_1, \hat{p}_2, D_1, C_2, D_2, E_2, \hat{h})$ , and the matrix  $A$  is:

$$A = \begin{pmatrix} 0 & R_2^2 & 0 & \log R_2 & 1 & 0 & 0 \\ 0 & \frac{R_2^3}{4} & 0 & \frac{2R_2 \log R_2 - R_2}{4} & \frac{R_2}{2} & \frac{1}{R_2} & 0 \\ R_1^2 & -\lambda R_1^2 & 1 & -\lambda \log R_1 & -\lambda & 0 & -\frac{4i\mu_1}{k} \left( \frac{\partial \bar{u}_1}{\partial r} - \frac{\partial \bar{u}_2}{\partial r} \right) \\ R_1^3 & -\lambda R_1^3 & 2R_1 & -\lambda R_1 (2 \log R_1 - 1) & -2\lambda R_1 & -\frac{4\lambda}{R_1} & 0 \\ -\frac{k^2}{16\mu_1} R_1^3 & 0 & -\frac{k^2 R_1}{8\mu_1} & 0 & 0 & 0 & i(k\bar{u}_z - \omega) \\ 2R_1 + \frac{3}{4} \frac{\kappa_s R_1^2}{\mu_1} & -2R_1 & \frac{1}{2} \frac{k^2}{\mu_1} & -\frac{1}{R_1} & 0 & 0 & -\frac{4i}{k} \left( \mu_1 \frac{\partial^2 \bar{u}_1}{\partial r^2} - \mu_2 \frac{\partial^2 \bar{u}_2}{\partial r^2} \right) - \frac{4\kappa_s}{R_1} \frac{\partial \bar{u}_s}{\partial z} \\ -1 - \frac{3}{16} \frac{k^2 R_1}{\mu_1} & 1 & -\frac{1}{8} \frac{k^2}{\mu_1 R_1} & 0 & 0 & 0 & -\gamma \left( \frac{1}{R_1^2} - k^2 \right) - \frac{\kappa_s}{R_1^2} \frac{\partial \bar{u}_s}{\partial z} \end{pmatrix}$$

### 4.3.9 Appendix 2: Dispersion relation

The system has non-trivial solution if  $\det A = 0$ , giving the dispersion relation:

$$\omega = F(k) + F_{sv}(k, \kappa_s) + i(G(k) + G_{sv}(k, \kappa_s)) \quad (4.75)$$

If we define the dimensionless wave frequency and wavenumber as

$$\tilde{\omega} = \omega\tau_v, \quad \tilde{k} = kR_2 \quad (4.76)$$

where  $\tau_v = \mu_2 R_2 / \gamma$  is the characteristic viscous timescale, the dispersion relation can be rewritten as

$$\omega = (F_u + F_f + F_p)\tilde{k} + F_{sv}(\tilde{k}, \kappa_s) + i \left( G(\tilde{k}^2 - h^2 \tilde{k}^4) + G_{sv}(\tilde{k}, \kappa_s) \right) \quad (4.77)$$



where

$$\begin{aligned}
 F_u &= \frac{\mu_2 \bar{u}_d}{\gamma} \\
 F_f &= \frac{(h_d - 1)^2 (h_d + 1)^2 h_d R_2 \lambda \mu_2}{(h_d^4 \lambda - h_d^4 - \lambda) \gamma} (\partial_r \bar{u}_1 - \partial_r \bar{u}_2) \\
 F_p &= \frac{\left( ((\lambda - 1) h_d^2 - \lambda) \log(h_d) - (h_d^2 - 1) \left( \left( -\frac{1}{2} + \lambda \right) h_d^2 - \lambda \right) \right) R_2^2 h_d^2 \mu_2^2 \left( \mu_1 \frac{\partial^2 \bar{u}_1}{\partial r^2} - \mu_2 \frac{\partial^2 \bar{u}_2}{\partial r^2} \right)}{2\gamma ((\lambda - 1) h_d^4 - \lambda)} \\
 F_{f_{sv}} &= -\frac{1}{2} \left( \left( ((\lambda - 1) h_d^4 - \lambda) \ln(h_d) + (1/4 - \lambda) h_d^4 + 2 h_d^2 \lambda - \lambda - 1/4 \right) h_d^2 \tilde{k}^3 \right. \\
 &\quad \left. \kappa_s \mu_2^2 (\partial_r \bar{u}_1 - \partial_r \bar{u}_2) R_2 \left( (2 + \lambda) h_d^4 - 2 h_d^2 \lambda + \lambda \right) \right) / \left( ((\lambda - 1) h_d^4 - \lambda) \right. \\
 &\quad \left( \tilde{k}^2 ((\lambda - 1) h_d^4 - \lambda) h_d \kappa_s \mu_2 \ln(h_d) - \tilde{k}^2 \kappa_s \mu_2 (5/4 + \lambda) h_d^5 \right. \\
 &\quad \left. - 4 R_2 (\lambda - 1) h_d^4 + 2 \tilde{k}^2 (1/2 + \lambda) \kappa_s \mu_2 h_d^3 - \tilde{k}^2 (-1/4 \lambda) \kappa_s \mu_2 h_d + 4 R_2 \lambda \right) \gamma) \\
 F_{p_{sv}} &= -1/2 \left( R_2^2 \left( ((\lambda - 1) h_d^4 - \lambda) \ln(h_d) - (h_d - 1) \left( (1/2 + \lambda) h_d^2 - \lambda \right) (h_d + 1) \right) \mu_2^3 \right. \\
 &\quad \left( ((\lambda - 1) h_d^4 - \lambda) \ln(h_d) + (1/4 - \lambda) h_d^4 + 2 h_d^2 \lambda - \lambda - 1/4 \right) (\partial_{rr} \bar{u}_1 - \partial_{rr} \bar{u}_2) h_d^3 \kappa_s \tilde{k}^3) / \\
 &\quad \left( ((\lambda - 1) h_d^4 - \lambda) \gamma \left( \tilde{k}^2 ((\lambda - 1) h_d^4 - \lambda) h_d \kappa_s \mu_2 \ln(h_d) - \tilde{k}^2 \kappa_s \mu_2 (5/4 + \lambda) h_d^5 \right) \right. \\
 &\quad \left. - 4 R_2 (\lambda - 1) h_d^4 + 2 \tilde{k}^2 (1/2 + \lambda) \kappa_s \mu_2 h_d^3 - \tilde{k}^2 (-1/4 + \lambda) \kappa_s \mu_2 h_d + 4 R_2 \lambda \right) \gamma) \\
 G_\gamma &= \frac{\mu_2^2 h_d \left( ((\lambda - 1) h_d^4 - \lambda) \ln(h_d) + \left( -\lambda + \frac{3}{4} \right) h_d^4 + (-1 + 2\lambda) h_d^2 + \frac{1}{4} - \lambda \right)}{4\lambda - 4(\lambda - 1) h_d^4} \\
 G_{\gamma_{sv}} &= \left( -1/4 \mu_2^3 \kappa_s \tilde{k}^4 \left( ((\lambda - 1) h_d^4 - \lambda) \ln(h_d) + (1/4 - \lambda) h_d^4 + 2 h_d^2 \lambda - \lambda - 1/4 \right)^2 \right. \\
 &\quad \left. h_d^2 (h_d \tilde{k} + 1) (-1 + h_d \tilde{k}) \right) / \left( \left( \tilde{k}^2 ((\lambda - 1) h_d^4 - \lambda) h_d \kappa_s \mu_2 \ln(h_d) \right. \right. \\
 &\quad \left. - \tilde{k}^2 \kappa_s \mu_2 (5/4 + \lambda) h_d^5 - 4 R_2 (\lambda - 1) h_d^4 + 2 \tilde{k}^2 (1/2 + \lambda) \kappa_s \mu_2 h_d^3 - \right. \\
 &\quad \left. \tilde{k}^2 (-1/4 + \lambda) \kappa_s \mu_2 h_d + 4 R_2 \lambda \right) ((\lambda - 1) h_d^4 - \lambda) \gamma) \\
 G_{uz_{sv}} &= \left( 1/2 h_d \left( \left( \tilde{k}^2 \kappa_s \mu_2 h_d^5 + 6 R_2 (\lambda - 1) h_d^4 - \tilde{k}^2 \kappa_s \mu_2 h_d - 6 R_2 \lambda \right) \ln(h_d) \right. \right. \\
 &\quad \left. - \left( \tilde{k}^2 \kappa_s \mu_2 h_d^3 + (-7/2 R_2 + 6 R_2 \lambda) h_d^2 - \tilde{k}^2 \kappa_s \mu_2 h_d - 6 R_2 \lambda + 1/2 R_2 \right) (h_d - 1) (h_d + 1) \right) \\
 &\quad \left. \kappa_s \mu_2^2 \partial_z \bar{u}_s \tilde{k}^2 \right) \left( \left( \tilde{k}^2 ((\lambda - 1) h_d^4 - \lambda) h_d \kappa_s \mu_2 \ln(h_d) - \tilde{k}^2 \kappa_s \mu_2 (5/4 + \lambda) h_d^5 \right. \right. \\
 &\quad \left. - 4 R_2 (\lambda - 1) h_d^4 + 2 \tilde{k}^2 (1/2 + \lambda) \kappa_s \mu_2 h_d^3 - \tilde{k}^2 (-1/4 + \lambda) \kappa_s \mu_2 h_d + 4 R_2 \lambda \right) \gamma)
 \end{aligned}$$



# Conclusion

In this thesis we studied the stability of two phase co-axial jets in progressively increasing complexity. We tackled the problem starting from a liquid thread in a quiescent surrounding, and adding ingredients, like viscous effects or a surrounding dynamically active medium, we identified key parameters that influence the stability of co-flow jets.

**Chapter 1** Our analysis started from liquid threads and jets immersed in a dynamically inert medium. The stability analysis can be performed with three different approach: (i) exact solution, express as function of Bessel functions, (ii) numerically, discretizing the equation by Chebyshev polynomials or (iii) long-wavelength description. We saw that the latter method is always in very good agreement with the exact solution, if it exists, and with the numerical results. The power of the long-wavelength description lies on his mathematical simplicity and allows to easily determine different quantities like the cut-off and the most amplified wavenumber. While a liquid thread always breaks up in droplets, if we increase the streams velocity, for a liquid jet a transition from dripping to jetting can occurs. The dripping/ jetting transition can be determined as a function of the dimensionless parameters: Weber number (for the inviscid jet), Capillary number (for the viscous thread) and Ohnesorge number (for viscous thread with inertia). Finally, in order to explain the relationship between absolute/convective instability and global instability, for a cylindrical viscous thread, bounded by an inlet and an outlet boundary condition, we saw that the global eigenvalues are dictated by the local absolute properties.

**Chapter 2** In the second chapter, we added the contribution of an external medium. We saw that a quiescent surrounding fluid has always a stabilizing effect on liquid threads, although it is not anymore possible to use the long-wavelength description. When an external medium is added to the system, we need to consider two important factors: (i) the outer flow has to move with the inner flow, and (ii) the external flow exerts a force through its shear stress. This precludes the use the long-wavelength description. The leading order expansion of the equations is not able to describe the system, and in order to take into account the viscous effect we need to include the second order correction term of the streamwise velocity. To study the stability of a jet in a surrounding medium, an accurate determination of the base flow becomes necessary. Finally, we focused on the case which is studied in the rest of the thesis: viscous jet immersed in another

## Conclusion

---

viscous radially bounded flow. The flow eventually becomes parallel after a transition (so called entry) region, and then it is possible to determine analytically the base flow. The absolute/convective transition shows that the lubrication solution of the perturbed equations and the exact solution yield very similar results.

**Chapter 3** With the aim of studying the global stability of a co-axial flow, where the flow is not anymore assumed parallel, we had to take into account the existence of a sharp interface separating the fluids and the existence of localized stress discontinuity at the free surface between these two fluids. We developed two new tools: (i) we implemented a level set function in order to obtain an accurate description of the steady state and interface, and (ii) a two-domain discretization to determine the global eigenvalues. We have determined the transition from dripping to jetting as function of three dimensionless parameters: the viscosity ratio, the degree of confinement and the Capillary number. We showed that, surprisingly, the nozzle geometry doesn't affect the stability properties of the flow. The global stability analysis of the non-parallel flow recovers almost the same results of the local analysis by Herrada *et al.* (2008), which implies that the dripping to jetting transition is a process dominated by the intrinsic properties of the developed streams.

**Chapter 4** To complete the description of the two-phase co-axial jet, we studied the influence of the surface viscosity. In first instance we derived the governing and constitutive equations to describe the continuum mechanism of the surface in the axisymmetric case. With this new set of equations we were able to outline the effects of surface viscosity on a viscous thread immersed into a dynamically inert medium: the presence of a surface dilatation viscosity stabilizes the thread, maintaining the cut-off unvaried, while the most amplified wavenumber depends on the dilatation viscosity. For the viscous thread we were able to write the dispersion relation using the long-wavelength description, and the comparison of the approximate solution with the exact one gave an excellent agreement. Then we applied the new constitutive equations to describe the steady state and stability of a co-axial jet. With the addition of surface viscosity at the interface, the base flow evolves over a lengthscale which is much larger than the entry length in the Stokes regimes and than the typical unstable wavelength. We showed that while the flow becomes eventually more convectively unstable once it reaches the fully developed profile, the surface viscosity creates an absolute region at the inlet, that is expected to promote droplet formation.

The present thesis suggests that a wide variety of flow parameters can be included in the analysis of two-phase co-axial flow, and that at the same time other mathematical tools can be explored. How can we extend the long-wavelength description to co-axial flow? Can we linearize the level set method to perform a global stability analysis? How does the inertia affect the steady state and the global stability of a coflow? Is it possible to set up experiments to validate the results obtained? These are only a few possible questions opening interesting perspectives.

## Theoretical perspectives

In the thesis we saw the **long-wavelength description** is a very powerful tool for the study both of the base flow and the stability properties. The long-wavelength approximation, as presented by Eggers & Dupont (1994), fails when the effect of a surrounding medium is included in the system. The description of the streamwise velocity through a uniform flow is not sufficient to describe the shear effects on the interface. A possible approach to extend the long-wavelength description to co-axial jet comes from Ruyer-Quil & Manneville (2000) Amaouche, Mehidi & Amatoousse (2007) and Mehidi & Amatoousse (2009). These authors use a combination of the long-wavelength description and of a weighted residual approach for determine the stability of two-layer film flow down in a inclined plane. The strategy follows four main steps: (i) with the hypothesis of slow variation in time and streamwise direction, the governing equations and boundary conditions are rewritten with the thin layer approximation. In order to reduce the number of unknowns, (ii) the pressure is eliminated from the Navier-Stokes using the normal stress interfacial condition and the boundary conditions. (iii) the velocity field is then expanded is Taylor series  $\mathbf{u}_i = a_i(z, t) + b_i(z, t)\varepsilon + c_i(z, t)\varepsilon^2 + \mathcal{O}(\varepsilon^3)$  and the equations are solved up to the second order of  $\varepsilon$ . Finally (iv) the dependency on  $r$  is eliminated with the residual approach, i.e. multiply each governing equation for a suitable weight function.

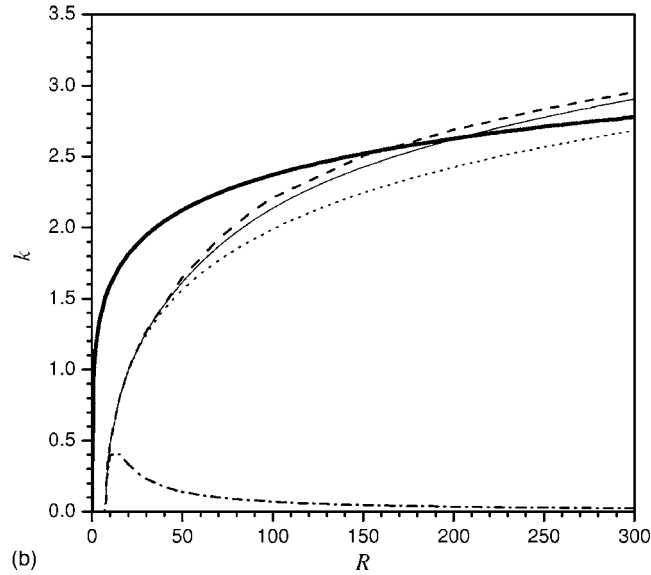


**Figure 1** – Amaouche *et al.* (2007), comparison of the neutral stability curve generate with the second order approach (solid continuous line) and numerical solution dashed line, for the air-water system in the (Reynolds, marginal wavenumber)-plane, for Capillary number  $Ca = 1/100$ , inclination of the plane  $\theta = 20^\circ$  inclination plane and height of the interface  $h = 0.3$ .

## Conclusion

The **linearization level set** allows to determine the global stability properties in one fixed domain, implementing only one Navier-Stokes equation for both phases. With the level set approach the continuity of the velocity at the interface and the stress conditions are naturally imposed, while the Capillary effects are modeled like a forcing term in the Navier-Stokes equations. All the varying quantities like viscosity, density and normal vector are expressed as function of the level set functions. The advantage of the level set method is that we can perform numerical simulation with low Capillary number without having to parametrize the surface curvature. While the expression of the equilibrium is quite straightforward, the linearization of equation is quite involved. The perturbed equations require the differentiation of each function with respect to the level-set, including the Heaviside and Dirac  $\delta$ -function.

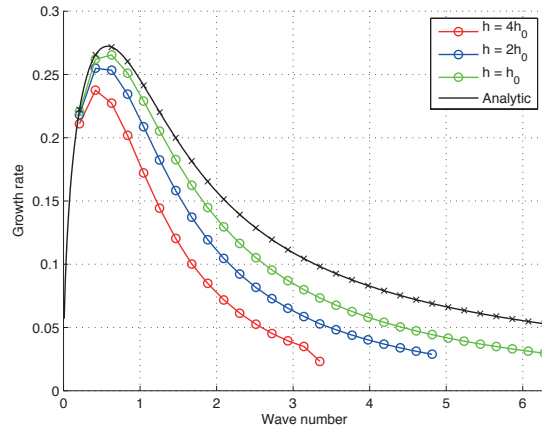


**Figure 2** – Example of Rayleigh-Taylor instability solved numerically with the level set approach. Convergence analysis with different transition thickness of the Heaviside function. Numerical simulation carried out by M.A. Habisreutinger (LFMI).

## Numerical perspectives

The **inertial** effect can be included in the analysis with similar steps done in the global stability analysis (chapter 3). As far as the **base flow** is concerned, in the level set approach it is necessary to investigate a new suitable criterium for diffusion coefficient in the advection-convection equation (Hughes & Mallet (1986)). Moreover, the bi-Poiseuille flow does not develop anymore in about a radius of the pipe, and an a priori investigation of the suitable length of computational domain is required. This is confirmed by figure 3 where we see that the entry length increases with the Reynolds number.

Regarding the second step, the **stability analysis**, Herrada *et al.* (2008) have shown for the fully developed profile, how to perform a numerical local analysis using Chebyshev spectral collocation points, and a transition from dripping to jetting is given as function of the Capillary number. We have obtained similar results using a modification of the code

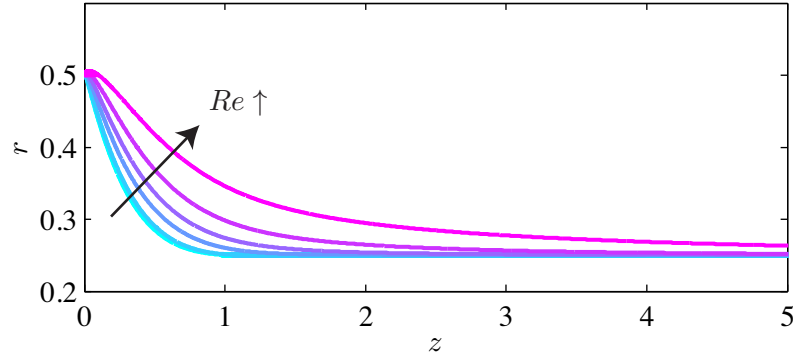


**Figure 3** – Effect of inertia on the interface location with viscosity ratio  $\lambda = 0.1$  and Reynolds number  $Re = \{0, 1, 5, 10, 20, 50\}$ .

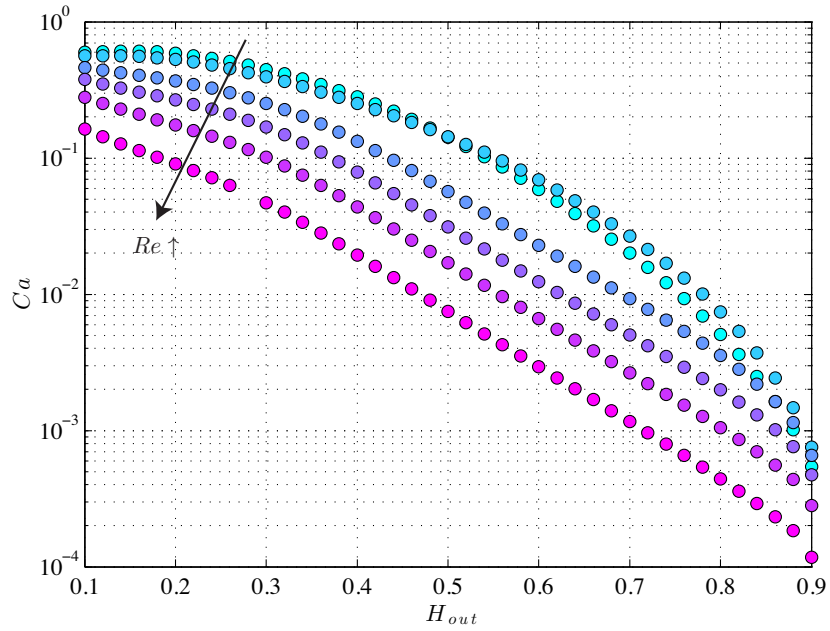


**Figure 4** – Effect of inertia on the local stability on a fully developed profile with viscosity ratio  $\lambda = 0.1$  and Reynolds number  $Re = \{0, 1, 5, 10, 20, 50\}$ .

described in appendix A and obtained the preliminary results shown in figure 4. These modified A/C marginal curves will be of great importance when detailed experimental comparisons have to be performed.

In presence of inertia, the weakly non parallel or fully global analyses remain to be conducted by combining these two steps (in the spirit of chapter 4) or by a generalization of the global analysis of chapter 3. A significant effect of the nozzle geometry can be expected when the Reynolds number increases.

## Conclusion

---

**Surface rheology solved with the level set.** Solve the steady state and the perturbed problem with the level set approach together with the constitutive equations of the surface rheology can be an interesting and challenging future project. The terms in the stress condition that depend on the surface viscosity have to be model as forcing terms and added to the classic level set description. A correct determination of the steady state allows a better understanding of the effect of surface rheology on the entry region, where the spatial invariance is broken.

A **DNS** simulation allows a deep understanding of the droplet shedding. A parametric study can be very interesting especially to study the formation of satellite droplets and the characteristic length and timescale for the breakup. As seen in figure 4.21, we have started to use an axisymmetric version of *Gerris* to conduct such an approach, with promising preliminary results.

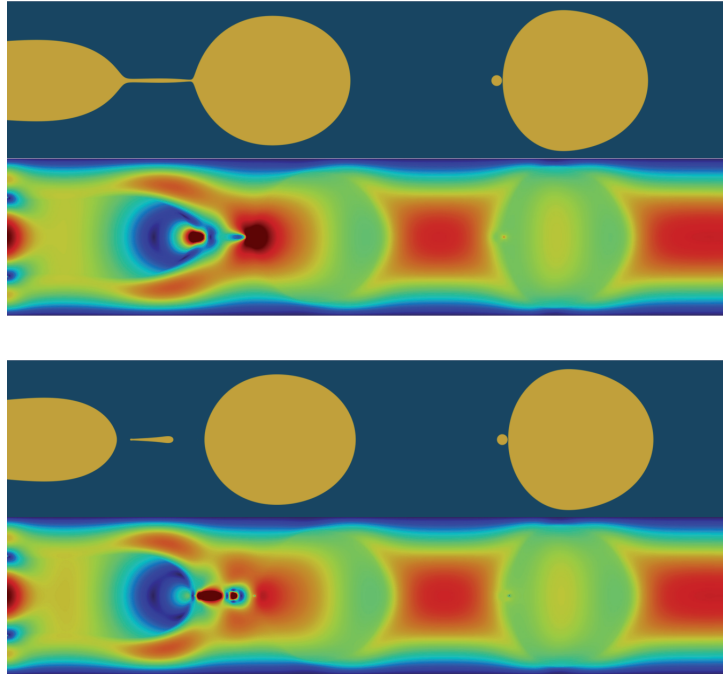


**Figure 5** – Volume of fraction and streamwise velocity for two consecutive simulation times. Simulation carried out at LFMI with the software *Gerris*.

## Experimental perspectives

In order to fully validate the results the comparison with the experiments becomes necessary. Probably the best way to proceed is benchmark the experiment with the one of Guillot *et al.* (2007), and add ingredients like surfactants and see how the dripping transition is modified by varying the capillary number (in collaboration with Benoit Sheid). In another starting collaboration with A. Colin and M.Moire (IFP), who plan to measure



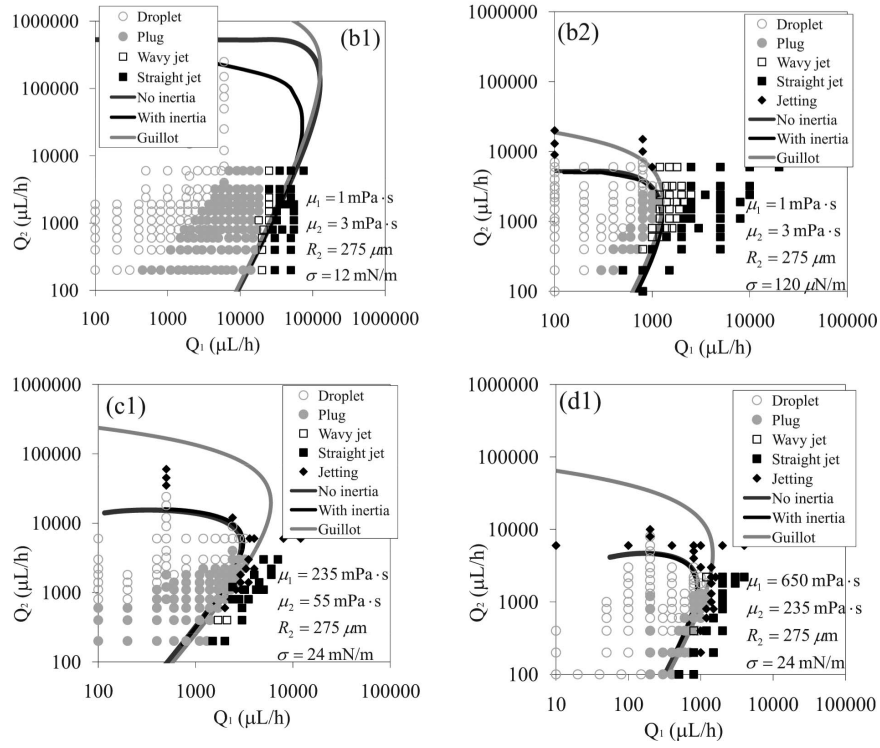


**Figure 6** – Simulation and experiment on co-axial flow carried out by Guillot *et al.* (2007), Herrada *et al.* (2008)

very small surface tension using the dripping/jetting experimental transition, we will provide an accurate dripping/jetting transition prediction based on absolute/convective transition or global stability analysis including inertia.



# A Numerical scheme for the spatio-temporal analysis of coaxial jets

Problem governs the perturbation evolution of two phase coaxial jets configuration, written in a cylindrical frame of reference. A sketch of the domain, along with an example of base flow velocity profiles is shown in Fig. 1.

It is useful to rewrite the equations in the following form

$$\mathbf{L}(k, \lambda, Ca) \mathbf{q} = -i\omega \mathbf{M} \mathbf{q} \quad (\text{A.1})$$

where  $\mathbf{L}$  depends on the complex streamwise wavenumber  $k$  and of the flow parameters such as viscosity ratio  $\lambda$  and capillary number  $Ca$ . The array

$$\mathbf{q} = [u_1(r), v_1(r), p_1(r), u_2(r), v_2(r), p_2(r), \eta] \quad (\text{A.2})$$

contains the field variables (velocity and pressure) for the two fluids and the interface perturbation  $\eta$ . The complex matrix  $\mathbf{L}$  can be written as

$$\mathbf{L} = \begin{bmatrix} \lambda D_z & 0 & -ik & 0 & 0 & 0 & 0 \\ 0 & \lambda D_r & -\partial_r & 0 & 0 & 0 & 0 \\ ik & \frac{1}{r} + \partial_r & 0 & 0 & 0 & 0 & 0 \\ 0 & 0 & 0 & D_z & 0 & -ik & 0 \\ 0 & 0 & 0 & 0 & D_r & -\partial_r & 0 \\ 0 & 0 & 0 & ik & \frac{1}{r} + \partial_r & 0 & 0 \\ 0 & 1 & 0 & 0 & 0 & 0 & -ik \end{bmatrix} \quad (\text{A.3})$$

where  $D_z = \partial_r^2 + \frac{\partial_r}{r} - k^2$  and  $D_r = D_z + \frac{1}{r^2}$  are the streamwise and radial components

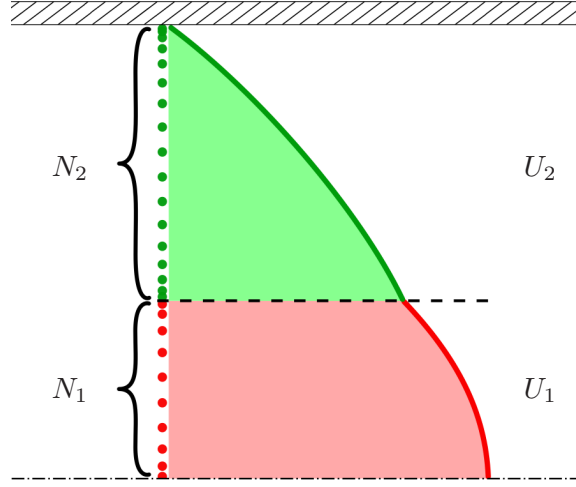


**Figure 1** – Physical domain for the spatiotemporal analysis. An example of the Chebyshev-Gauss-Lobatto collocation points is plotted as circles for the two domains.

of the laplacian operator. The mass matrix  $\mathbf{M}$  is

$$\mathbf{M} = \begin{bmatrix} 0 & 0 & 0 & 0 & 0 & 0 & 0 \\ 0 & 0 & 0 & 0 & 0 & 0 & 0 \\ 0 & 0 & 0 & 0 & 0 & 0 & 0 \\ 0 & 0 & 0 & 0 & 0 & 0 & 0 \\ 0 & 0 & 0 & 0 & 0 & 0 & 0 \\ 0 & 0 & 0 & 0 & 0 & 0 & 0 \\ 0 & 0 & 0 & 0 & 0 & 0 & 1 \end{bmatrix} \quad (\text{A.4})$$

Problem (A.1) along with the appropriate boundary conditions (see § 2.4.5 for details) is solved numerically by using a Chebyshev spectral collocation method (see Canuto *et al.* (1993) for details on the method). The linearized equations are discretized in the  $r$  direction using Chebyshev spectral collocation points ( $N_1$  points for the inner fluid and  $N_2$  points for the outer one). The interval  $0 \leq r \leq h_{int}$  is discretized and mapped into the Chebyshev-Gauss-Lobatto polynomial domain  $-1 \leq \xi \leq 1$  by means of the algebraic transformation:

$$r_j = h_{int} \frac{(1 - \xi_j)}{2} \quad (j = 1, \dots, N_1) \quad (\text{A.5})$$

while the interval  $h_{int} \leq r \leq 1$  is mapped using:

$$r_j = h_{int} + (1 - h_{int}) \frac{(1 - \xi_j)}{2} \quad (j = 1, \dots, N_2) \quad (\text{A.6})$$

The generalized eigenvalue problem is solved numerically by using the QZ algorithm (Moler & Stewart (1973)) present in MATLAB (function *eig*).

---

In a spatio-temporal analysis  $k$  and  $\omega$  are both allowed to be complex numbers and we look for the absolute frequency and wavenumber  $(\omega_0, k_0)$ . Here we compute numerically the saddle point in the  $(k_r, k_i)$  complex plane by looking for the solution of  $v_g = \partial\omega/\partial k = 0$ . The group velocity  $v_g$  is computed with the following procedure, using the proprieties of the adjoint operator (see Luchini & Bottaro (2014) for details) :

---

**Algorithm 1** Computation of  $\partial\omega/\partial k$

---

- 1: Choose  $k$
  - 2: Solve eigenvalue problem:  $\mathbf{L}(k)\mathbf{q} = -i\omega\mathbf{M}\mathbf{q}$
  - 3: Solve adjoint problem:  $\mathbf{y}^H\mathbf{L}(k) = -i\omega\mathbf{y}^H\mathbf{M}$
  - 4: Compute  $\delta\mathbf{L}$  for a choosen  $\delta k$
  - 5: Compute  $\delta\omega = \frac{\mathbf{y}^H\delta\mathbf{L}\mathbf{q}}{\mathbf{y}^H\mathbf{q}}$
  - 6:  $\frac{\partial\omega}{\partial k} = \frac{\delta\omega}{\delta k}$
- 

If the hypothesis of vanishing Reynolds number is not anymore valid, this approach can be generalized, including the inertial terms.



## B Level set

Problems involving moving boundaries and free interfaces exist in a wide range of applications, such as image processing, fluid-structure interactions, front propagations and multi-phase flows.

To capture the free surface different methods have been developed. Historically one of the first method to distinguish the two fluid is the volume of fluid (VOF) method (Hirt & Nichols (1981)). In this case the interface is given by a color function, defined as the volume fraction of one component within each cell. The propagation of the interface is made implicitly by updating the color function. This method has the advantage of being a conservative method but is often rather inaccurate (Olsson & Kreiss (2005)).

Another approach for the free surface is to track the interface boundary explicitly by markers, and then propagate these markers. The free surface is viewed as a movable object and the two fluids are solved in two different grids. The continuity of the velocity as well the jump of the stress are imposed at the interface. This method is called *front tracking* and requires mesh deformation and special care has to be taken to topological changes (Wilkes, Phillips & Basaran (1999) and Li, Renardy & Renardy (2000)).

Recently, the level set method have widely used in variety of application such as imagining segmentation (i.e. read the MRI Li, Huang, Ding, Gatenby, Metaxas & Gore (2011)), flame propagation and multi-phase flows. A general description of level set can be found in Sethian (1999) and Osher & Fedkiw (2001), a conservative version of level set can be found in Olsson & Kreiss (2005) and Olsson *et al.* (2007). Application to two phase flow can be found in Sussman, Smereka & Osher (1994)-Sussman, Fatemi, Smereka & Osher (1998).

The idea of the level set is quite simple, the interface is represented by the zero contour of a signed distance function. The displacement of the interface is governed by a differential equation for the level set function. The main advantages of this method is that it automatically deals with topological changes and it is amenable to high orders of accuracy.

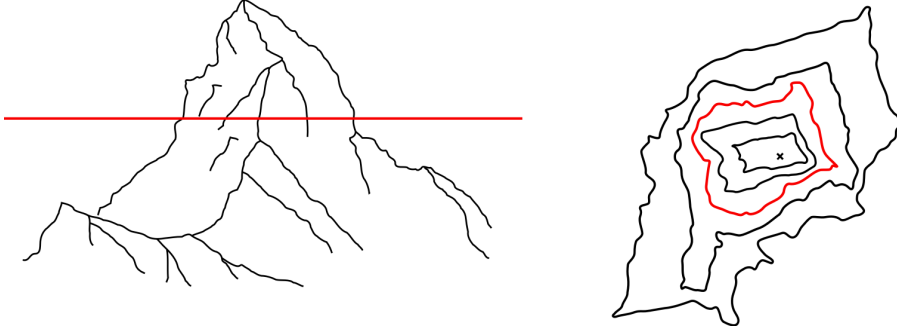


**Figure 1** – The isolines are special case of the level set value, where the shape of the mountain relates the shape of the level set function. Conventionally the zero level corresponds to the level of the sea, but in general any altitude can be chosen as reference level. Then in a geographical map the isolines identify the signed altitude from the reference level.

## Mathematical formulation

In our model an inner and a surrounding outer fluid stream with different velocity enter into a channel with the hypothesis of axisymmetry. The development of the flow field in space is completely determined by the inflow profile, densities and viscosities of the fluids, as well as the surface tension between them. The outlet boundary condition is chosen in such a way that it disrupts the flow as little as possible.

The fluid flow is governed by the stationary Navier-Stokes equation

$$\rho(\mathbf{u} \cdot \nabla) \mathbf{u} = \nabla \cdot [-p\mathbb{I} + \mu(\nabla \mathbf{u} + (\nabla \mathbf{u})^T)] + \sigma \mathcal{C} \mathbf{n} \delta \quad (\text{B.1})$$

$$\nabla \cdot \mathbf{u} = 0 \quad (\text{B.2})$$

where  $\rho$  denotes the total density,  $\mu$  the local viscosity,  $\mathbf{u}$  the velocity field,  $p$  the pressure,  $\sigma$  the surface tension coefficient,  $\mathcal{C}$  the surface curvature at the fluid interface,  $\mathbf{n}$  is the unit normal to the interface and  $\delta$  is the delta function which has unit integral and is located, or so to say infinitely peaked, on the interface.

In a finite element formulation, to avoid computing the curvature explicitly in the surface tension term, it is possible to integrate this term by parts using a surface divergence theorem. By doing so, the corresponding force can be included by adding the weak contribution

$$\sum_{i=1}^d \sigma \delta (\nabla_s \hat{u}_i)_i \quad (\text{B.3})$$



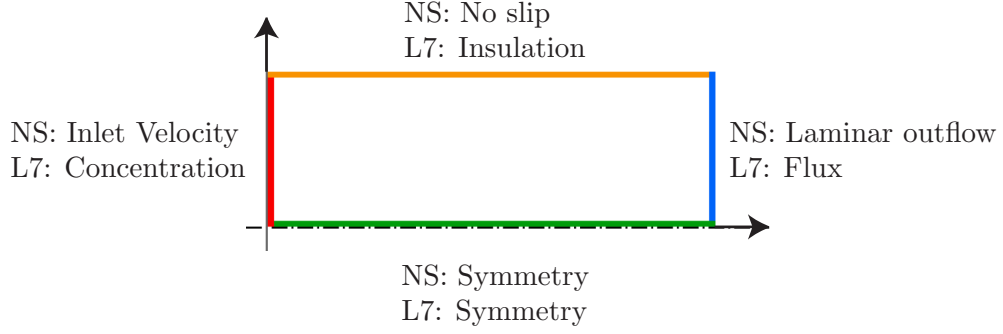


**Figure 2** – Sketch of the boundary conditions for the Navier-Stokes equation (NS) and level set equation (L7).

where  $\nabla_s = (\mathbb{I} - \mathbf{nn}) \cdot \nabla$  represents the surface gradient operator and  $\hat{u}_i$  the test function for the  $i$ -th velocity component.

The two fluids are computed in the same fixed grid by implementing the Navier-Stokes equation for a single velocity field in the full domain, and the two layers are distinguished by the presence of the level set function. This approach is very similar to the case of two miscible flow at very high Schmidt number.

The level set method models the fluid interface by tracking the isolines of a dimensionless level set function  $\phi$ . As stated previously, the idea is construct the level set as a signed distance function, therefore the zero level set at  $\phi = 0$  determines the position of the interface. While positive value of  $\phi$  denote the inner fluid and negative value of  $\phi$  the outer fluid:

$$\begin{cases} \phi > 0 & \text{inner fluid,} \\ \phi = 0 & \text{interface,} \\ \phi < 0 & \text{outer fluid.} \end{cases} \quad (\text{B.4})$$

The variable  $\phi$  is transported by the stationary advection-convection equation:

$$\nabla \cdot (-D \nabla \phi) = -\mathbf{u} \cdot \nabla \phi, \quad (\text{B.5})$$

where  $D$  is a diffusion coefficient required for numerical stability.

An important aspect in this model is the treatment of the varying viscosity as a function of the level set function. Denoting with  $\mu_1$  the viscosity of inner layer and  $\mu_2$  the viscosity of outer layer, it is possible express a local viscosity function as

$$\mu = \mu_2 + \mathcal{H}_e(\phi) \cdot (\mu_1 - \mu_2). \quad (\text{B.6})$$

where  $\mathcal{H}_e(\phi)$  is a Heaviside function with continuous second derivative and  $e$  is the

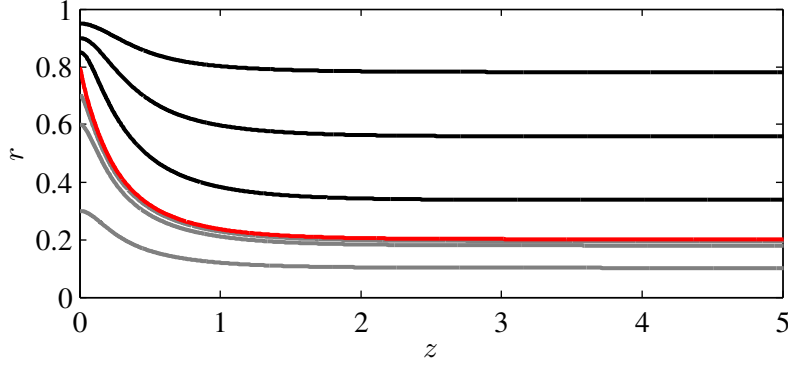


**Figure 3** – Isolines of the level set function. The black lines correspond to the outer flow ( $\phi < 0$ ), red line to the interface location ( $\phi = 0$ ), while the grey lines to the inner flow ( $\phi > 0$ ).

transition thickness of the Heaviside function which depends on the mesh size. The geometric properties of the interface are easily determined from the level set function. The surface curvature at the fluid interface  $\mathcal{C}$ , and the unit normal to the interface  $\mathbf{n}$ , are defined as:

$$\mathcal{C} = \nabla \cdot \frac{\nabla \phi}{|\nabla \phi|} \Big|_{\phi=0} \quad (\text{B.7})$$

$$\mathbf{n} = \frac{\nabla \phi}{|\nabla \phi|} \Big|_{\phi=0} \quad (\text{B.8})$$

The capillary force is then localized at the interface by the Dirac function.

An important aspect of the level-set method is the treatment of the artificial diffusion  $D$  required for numerical stability. The diffusion coefficient is defined as

$$D = \delta_{sd} h ||\mathbf{u}|| \quad (\text{B.9})$$

where  $h$  is the mesh size. In our model we used a streamline diffusion (Streamline Upwind Petrov-Galerkin method with tuning parameter  $\delta_{sd} = 0.25$  Hughes & Mallet (1986)). This consists of non isotropic diffusion coefficient which only acts along the streamlines and the cross-stream distortions.

The base flow simulations were carried out with COMSOL *Multiphysics 4.2* a with P2-P1 discretization for the fluid and a cubic discretization for  $\phi$ . The non linear base state is obtained with a Newton method where the linear systems are solved with the direct solver PARDISO (Schenk *et al.* (2008)).

# Bibliography

- AMAOUCHE, M., MEHIDI, N. & AMATOUSSE, N. 2007 Linear stability of a two-layer film flow down an inclined channel: A second-order weighted residual approach. *Physics of Fluids (1994-present)* **19** (8).
- ANNA, S. L., BONToux, N. & STONE, H. A. 2003 Formation of dispersions using "flow focusing" in microchannels. *Appl. Phys. Lett.* **82** (3), 364–366.
- ANNA, S. L. & MAYER, H. C. 2006 Microscale tipstreaming in a microfluidic flow focusing device. *Physics of Fluids (1994-present)* **18** (12), 121512.
- BAROUD, CHARLES N, GALLAIRE, FRANÇOIS & DANGLA, RÉMI 2010 Dynamics of microfluidic droplets. *Lab on a chip* **10** (16), 2032–45.
- BAYVEL, L. P & ORZECOWSKI, Z 1993 *Liquid atomization*. Washington, DC : Taylor & Francis.
- BECHTEL, S. E., BOLINGER, K. D., CAO, J. Z. & FOREST, M. G. 1995 Torsional effects in high-order viscoelastic thin-filament models. *SIAM Journal on Applied Mathematics* **55** (1), 58–99.
- BERS, A. 1983 *Handbook of Plasma Physics I*. North-Holland, Amsterdam.
- BOUSSINESQ, J. 1913 Existence of a superficial viscosity in the thin transition layer separating one liquid from another contiguous fluid. *C. R. Acad. Sci.* **156**, 983–89.
- BRENNER, MICHAEL P., SHI, X. D. & NAGEL, SIDNEY R. 1994 Iterated instabilities during droplet fission. *Phys. Rev. Lett.* **73**, 3391–3394.
- BREZZI, FRANCO & FALK, RICHARD S. 1991 Stability of higher-order hood-taylor methods. *SIAM Journal on Numerical Analysis* **28** (3), pp. 581–590.
- BRIGGS 1964 Electron-stream interaction with plasmas. *MIT press* **21**.
- BRUN, P.T., DAMIANO, ADAM, RIEU, PIERRE, BALESTRA, GIOELE & GALLAIRE, FRANÇOIS 2015 Rayleigh-Taylor instability under an inclined plane. *to be submitted* .

## Bibliography

---

- CANUTO, C., HUSSAINI, M. Y., QUARTERONI, A. & ZANG, T. A. 1993 *Spectral Methods in Fluid Dynamics*. New York: Springer-Verlag.
- CASTRO-HERNÁNDEZ, E., CAMPO-CORTÉS, F. & GORDILLO, JOSÉ MANUEL 2012 Slender-body theory for the generation of micrometre-sized emulsions through tip streaming. *Journal of Fluid Mechanics* **698**, 423–445.
- CHANDRASEKHAR, S. 1961 *Hydrodynamic and Hydromagnetic Stability*. Dover.
- CHOMAZ, J.M. 2005 Global instabilities in spatially developing flows: non-normality and nonlinearity. *Annual Review of Fluid Mechanics* **37**, 357–392.
- CLANET, C & LASHERAS, J. C. 1999 Transition from dripping to jetting. *Journal of Fluid Mechanics* **383**, 307–326.
- CORDERO, M. L., GALLAIRE, F. & BAROUD, C. N. 2011 Quantitative analysis of the dripping and jetting regimes in co-flowing capillary jets. *Physics of Fluids* **23** (9), 094111.
- CRAMER, CARSTEN, FISCHER, PETER & WINDHAB, ERICH J. 2004 Drop formation in a co-flowing ambient fluid. *Chemical Engineering Science* **59** (15), 3045–3058.
- DERBY, BRIAN 2010 Inkjet printing of functional and structural materials: Fluid property requirements, feature stability, and resolution. *Annual Review of Materials Research* **40** (1), 395–414.
- DOLLET, BENJAMIN, VAN HOEVE, WIM, RAVEN, JAN-PAUL, MARMOTTANT, PHILIPPE & VERSLUIS, MICHEL 2008 Role of the channel geometry on the bubble pinch-off in flow-focusing devices. *Phys. Rev. Lett.* **100**, 034504.
- DRENCKHAN, W. & SAINT-JALMES, A. 2015 The science of foaming. *Adv. Colloid Interface Sci.* p. 034504, in press.
- DUCLAUX, V., CLANET, C & QUÉRÉ, D. 2006 The effects of gravity on the capillary instability in tubes. *Journal of Fluid Mechanics* **556**, 217–226.
- DUPRAT, C., RUYER-QUIL, C. & GIORGIUTTI-DAUPHINÉ, F. 2009 Spatial evolution of a film flowing down a fiber. *Physics of Fluids (1994-present)* **21** (4).
- EDWARDS, D. A., BRENNER, H. & WASAN, D. T. 1991 *Interfacial Transport Processes and Rheology*. Butterworth–Heinemann.
- EGGERS, JENS 1997 Nonlinear dynamics and breakup of free-surface flows. *Rev. Mod. Phys.* **69**, 865–930.
- EGGERS, JENS & DUPONT, TODD F. 1994 Drop formation in a one-dimensional approximation of the navier-stokes equation. *Journal of Fluid Mechanics* **262**, 205–221.

- EGGERS, JENS & VILLERMAUX, EMMANUEL 2008 Physics of liquid jets. *Reports on Progress in Physics* **71** (3), 036601.
- FULLER, GERALD G. & VERMANT, JAN 2012 Complex fluid-fluid interfaces: Rheology and structure. *Annual Review of Chemical and Biomolecular Engineering* **3** (1), 519–543.
- GIBBS, W.J. 1878 On the equilibrium of heterogeneous substances. *Trans. Conn. Acad.* **3**, 108–248.
- GORDILLO, J. M., GAÑÁN-CALVO, A. M. & PÉREZ-SABORID, M. 2001 Monodisperse microbubbling: Absolute instabilities in coflowing gas-liquid jets. *Physics of Fluids (1994-present)* **13** (12), 3839–3842.
- GORDILLO, J. M., SEVILLA, A. & CAMPO-CORTÉS, F. 2013 Global stability of stretched jets: conditions for the generation of monodisperse micro-emulsions using coflows. *Journal of Fluid Mechanics* **738**, 335–357.
- GUILLOT, PIERRE & COLIN, ANNIE 2008 Stability of a jet in confined pressure-driven biphasic flows at low Reynolds number in various geometries. *Physical Review E* **78** (1), 016307.
- GUILLOT, PIERRE, COLIN, ANNIE, UTADA, ANDREW & AJDARI, ARMAND 2007 Stability of a Jet in Confined Pressure-Driven Biphasic Flows at Low Reynolds Numbers. *Physical Review Letters* **99** (10), 104502.
- HANSEN, S., PETERS, G. W. M. & MEIJER, H. E. H. 1999 The effect of surfactant on the stability of a fluid filament embedded in a viscous fluid. *Journal of Fluid Mechanics* **382**, 331–349.
- HEATON, C. J., NICHOLS, J. W. & SCHMID, P. J. 2009 Global linear stability of the non-parallel Batchelor vortex. *Journal of Fluid Mechanics* **629**, 139–160.
- HECHT, F. 2012 New development in freefem++. *J. Numer. Math.* **20** (3-4), 251–265.
- HERNANDEZ, VICENTE, ROMAN, JOSE E. & VIDAL, VICENTE 2005 SLEPc: A scalable and flexible toolkit for the solution of eigenvalue problems. *ACM Trans. Math. Software* **31** (3), 351–362.
- HERRADA, M., GAÑÁN CALVO, A. & GUILLOT, P. 2008 Spatiotemporal instability of a confined capillary jet. *Physical Review E* **78** (4), 046312.
- HETTIARACHCHI, K., TALU, E., LONGO, M. L., DAYTON, P. A. & LEE, A. P. 2007 On-chip generation of microbubbles as a practical technology for manufacturing contrast agents for ultrasonic imaging. *Lab Chip* **7** (4), 463–468.
- HIRT, C.W. & NICHOLS, B.D. 1981 Volume of fluid (vof) method for the dynamics of free boundaries. *Journal of Computational Physics* **39**, 201–225.

## Bibliography

---

- VAN HOEVE, WIM, GEKLE, STEPHAN, SNOEIJER, JACCO H., VERSLUIS, MICHEL, BRENNER, MICHAEL P. & LOHSE, DETLEF 2010 Breakup of diminutive Rayleigh jets. *Physics of Fluids* **22** (12), 122003.
- HUERRE, P & MONKEWITZ, P A 1990 Local and global instabilities in spatially developing flows. *Annual Review of Fluid Mechanics* **22** (1), 473–537.
- HUERRE, P & ROSSI, M 1998 Hydrodynamic instabilities in open flows. *COLLECTION ALEA SACLAY MONOGRAPHS AND TEXTS IN STATISTICAL PHYSICS* pp. 81–294.
- HUGHES, THOMAS J.R. & MALLET, MICHEL 1986 A new finite element formulation for computational fluid dynamics: Iii. the generalized streamline operator for multidimensional advective-diffusive systems. *Computer Methods in Applied Mechanics and Engineering* **58** (3), 305 – 328.
- JAVADI, A., EGGERS, J., BONN, D., HABIBI, M. & RIBE, N. M. 2013 Delayed capillary breakup of falling viscous jets. *Phys. Rev. Lett.* **110**, 144501.
- JIN, FANG, GUPTA, NIVEDITA R. & STEBE, KATHLEEN J. 2006 The detachment of a viscous drop in a viscous solution in the presence of a soluble surfactant. *Physics of Fluids (1994-present)* **18** (2).
- JOSEPH, D. D., BAI, R., CHEN, K. P. & RENARDY, Y. Y. 1997 Core-annular flows. *Annual Review of Fluid Mechanics* **29** (1), 65–90.
- JUNIPER, MP & CANDEL, SM 2003 The stability of ducted compound flows and consequences for the geometry of coaxial injectors. *Journal of Fluid Mechanics* **482**, 257–269.
- LASHERAS, J. C. & HOPFINGER, E. J. 2000 Liquid jet instability and atomization in a coaxial gas stream. *Annual Review of Fluid Mechanics* **32** (1), 275–308.
- LE DIZÈS, S. 1997 Global modes in falling capillary jets. *Eur. J. Mech. B* **16** (6), 761–778.
- LEFEBVRE, A. H. 1989 *Atomization and Sprays*. CRC Press.
- LEIB, S. J. & GOLDSTEIN, M. E. 1986 The generation of capillary instabilities on a liquid jet. *Journal of Fluid Mechanics* **168**, 479–500.
- LESSHAFFT, LUTZ & HUERRE, PATRICK 2007 Linear impulse response in hot round jets. *Physics of Fluids (1994-present)* **19** (2).
- LESSHAFFT, LUTZ, HUERRE, PATRICK & SAGAUT, PIERRE 2007 Frequency selection in globally unstable round jets. *Physics of Fluids (1994-present)* **19** (5).
- LEVICH, V. G., ed. 1962 *Physicochemical Hydrodynamics*. Prentice–Hall.

- LI, CHUNMING, HUANG, RUI, DING, ZHAOHUA, GATENBY, J.C., METAXAS, D.N. & GORE, J.C. 2011 A level set method for image segmentation in the presence of intensity inhomogeneities with application to mri. *Image Processing, IEEE Transactions on* **20** (7), 2007–2016.
- LI, JIE, RENARDY, YURIKO Y. & RENARDY, MICHAEL 2000 Numerical simulation of breakup of a viscous drop in simple shear flow through a volume-of-fluid method. *Physics of Fluids (1994-present)* **12** (2), 269–282.
- LUCASSEN, J. & VAN DEN TEMPEL, M. 1972 Dynamic measurements of dilational properties of a liquid interface. *Chem. Eng. Sci.* **27** (6), 1283–1291.
- LUCHINI, PAOLO & BOTTARO, ALESSANDRO 2014 Adjoint equations in stability analysis. *Annual Review of fluid mechanics* **46** (1), 493.
- MARANGONI, C. 1872 The principle of the surface viscosity of liquids established by mr. j. plateau. *Nuovo Cimento* **2**, 239–273.
- MARMOTTANT, P. & VILLERMAUX, E. 2004 On spray formation. *Journal of Fluid Mechanics* **498**, 73–111.
- MEHIDI, N. & AMATOUSSE, N. 2009 Modélisation d'un écoulement coaxial en conduite circulaire de deux fluides visqueux. *Comptes Rendus Mécanique* **337**, 112–118.
- MELIGA, P., SIPP, D. & CHOMAZ, J.-M. 2008 Absolute instability in axisymmetric wakes: compressible and density variation effects. *Journal of Fluid Mechanics* **600**, 373–401.
- MOLER, CLEVE B & STEWART, GILBERT W 1973 An algorithm for generalized matrix eigenvalue problems. *SIAM Journal on Numerical Analysis* **10** (2), 241–256.
- MONKEWITZ, P.A. & SOHN, K. D. 1988 Absolute instability in hot jets. *AIAA JOURNAL* **26** (8), 911–916.
- OHNESORGE, WOLFGANG V. 1936 Die bildung von tropfen an düsen und die auflösung flüssiger strahlen. *ZAMM - Journal of Applied Mathematics and Mechanics /Z. Angew. Math. Mech.* **16** (6), 355–358.
- OLSSON, ELIN & KREISS, GUNILLA 2005 A conservative level set method for two phase flow. *Journal of Computational Physics* **210** (1), 225–246.
- OLSSON, ELIN, KREISS, GUNILLA & ZAHEDI, SARA 2007 A conservative level set method for two phase flow II. *Journal of Computational Physics* **225** (1), 785–807.
- OSHER, S. & FEDKIW, R. P. 2001 Level set methods: An overview and some recent results. *Journal of Computational Physics* **169** (2), 463 – 502.

## Bibliography

---

- PALIERNE, J.F. & LEQUEUX, F. 1991 Sausage instability of a thread in a matrix; linear theory for viscoelastic fluids and interface. *Journal of Non-Newtonian Fluid Mechanics* **40**, 289–306.
- PLATEAU, J.A.F. 1873 Statique expérimentale et théorique des liquides soumis aux seules forces moléculaires. *Paris: Gauthier-Villars* .
- POPINET, STÉPHANE 2003 Gerris: A tree-based adaptive solver for the incompressible euler equations in complex geometries. *J. Comp. Phys* **190**, 572–600.
- POWERS, THOMAS R. & GOLDSTEIN, RAYMOND E. 1997 Pearling and pinching: Propagation of rayleigh instabilities. *Phys. Rev. Lett.* **78**, 2555–2558.
- POWERS, THOMAS R., ZHANG, DENG FU, GOLDSTEIN, RAYMOND E. & STONE, HOWARD A. 1998 Propagation of a topological transition: The rayleigh instability. *Physics of Fluids (1994-present)* **10** (5), 1052–1057.
- POZRIKIDIS, C. 1992 *Boundary Integral and Singularity Methods for Linearized Viscous Flow*. Cambridge University Press, cambridge Books Online.
- PROSPERETTI, ANDREA & TRYGGVASON, GRÉTAR 2007 *Computational methods for multiphase flow*. Cambridge university press.
- QUAIA, E., ed. 2005 *Contrast Media in Ultrasonography*. Springer.
- RAYLEIGH, LORD 1879 On the instability of jets. *Proc. Lond. Math. Soc.* **10**, 4–13.
- RAYLEIGH, L. 1890 On the superficial viscosity of water. *Proc. R. Soc. Lond.* **48**, 127–140.
- RAYLEIGH, LORD 1892 On the stability of a cylinder of viscous liquid under capillary force. *Phil. Mag.* **34**, 145–54.
- RUYER-QUIL, C. & MANNEVILLE, P. 2000 Improved modeling of flows down inclined planes. *Eur. Phys. J. B* **15** (2), 357–369.
- VAN SAARLOOS, WIM 1988 Front propagation into unstable states: Marginal stability as a dynamical mechanism for velocity selection. *Phys. Rev. A* **37**, 211–229.
- SAGIS, LEONARD M. C. 2011 Dynamic properties of interfaces in soft matter: Experiments and theory. *Rev. Mod. Phys.* **83**, 1367–1403.
- SCHEID, B., DELACOTTE, J., DOLLET, B., RIO, E., RESTAGNO, F., VAN NIEROP, E. A., CANTAT, I., LANGEVIN, D. & STONE, H. A. 2010 The role of surface rheology in liquid film formation. *EPL (Europhysics Letters)* **90** (2), 24002.
- SCHENK, OLAF, BOLLHÖFER, MATTHIAS & RÖMER, RUDOLF A. 2008 On large-scale diagonalization techniques for the anderson model of localization. *SIAM Rev.* **50** (1), 91–112.



- SCRIVEN, L.E. 1960 Dynamics of a fluid interface equation of motion for newtonian surface fluids. *Chemical Engineering Science* **12** (2), 98 – 108.
- SELVAM, B., TALON, L., LESSHAFFT, L. & MEIBURG, E. 2009 Convective/absolute instability in miscible core-annular flow. part 2. numerical simulations and nonlinear global modes. *Journal of Fluid Mechanics* **618**, 323–348.
- SETHIAN, J. 1999 *Level Set Methods and Fast Marching Methods*. Cambridge: Cambridge University Press.
- SLATTERY, JOHN C., SAGIS, LEONARD & OH, EUN-SUOK 2007 *Interfacial Transport Phenomena*. Springer.
- STONE, H A 1994 Dynamics of Drop Deformation and Breakup in Viscous Fluids. *Annual Review of Fluid Mechanics* **26** (1), 65–102.
- STONE, H. A. & BRENNER, M. P. 1996 Note on the capillary thread instability for fluids of equal viscosities. *Journal of Fluid Mechanics* **318**, 373–374.
- SUSSMAN, MARK, FATEMI, EMAD, SMEREKA, PETER & OSHER, STANLEY 1998 An improved level set method for incompressible two-phase flows. *Computers & Fluids* **27** (5), 663–680.
- SUSSMAN, MARK, SMEREKA, PETER & OSHER, STANLEY 1994 A level set approach for computing solutions to incompressible two-phase flow. *Journal of Computational physics* **114** (1), 146–159.
- TAMMISOLA, OUTI, LUNDELL, FREDRIK & SÖDERBERG, L. DANIEL 2012 Surface tension-induced global instability of planar jets and wakes. *Journal of Fluid Mechanics* **713**, 632–658.
- THEOFILIS, V 2003 Advances in global linear instability analysis of nonparallel and three-dimensional flows. *Progress in aerospace sciences* **39** (4), 249–315.
- THEOFILIS, VASSILIOS 2011 Global linear instability. *Annual Review of Fluid Mechanics* **43**, 319–352.
- TIMMERMANS, M. L. E. & LISTER, J. R. 2002 The effect of surfactant on the stability of a liquid thread. *Journal of Fluid Mechanics* **459**, 289–306.
- TOMOTIKA, S. 1935 On the Instability of a Cylindrical Thread of a Viscous Liquid Surrounded by Another Viscous Fluid. *Proceedings of the Royal Society A: Mathematical, Physical and Engineering Sciences* **150**, 322–337.
- TROUTON, FRED. T. 1906 On the coefficient of viscous traction and its relation to that of viscosity. *Proceedings of the Royal Society of London A: Mathematical, Physical and Engineering Sciences* **77** (519), 426–440.

## Bibliography

---

- UTADA, ANDREW S., FERNANDEZ-NIEVES, ALBERTO, GORDILLO, JOSE M. & WEITZ, DAVID A. 2008 Absolute instability of a liquid jet in a coflowing stream. *Phys. Rev. Lett.* **100**, 014502.
- UTADA, ANDREW S., FERNANDEZ-NIEVES, ALBERTO, STONE, HOWARD A. & WEITZ, DAVID A. 2007 Dripping to jetting transitions in coflowing liquid streams. *Phys. Rev. Lett.* **99**, 094502.
- VAN DEN TEMPEL, M. 1977 Surface rheology. *J. Non-Newtonian Fluid Mech.* **2**, 205–219.
- VAN NIEROP, E. A., SCHEID, B. & STONE, H. A. 2008 On the thickness of soap films: an alternative to Frankel’s law. *J. Fluid Mech.* **602**, 119–127.
- VAN SAARLOOS, WIM 1989 Front propagation into unstable states. ii. linear versus nonlinear marginal stability and rate of convergence. *Phys. Rev. A* **39**, 6367–6390.
- WIJSHOFF, H. 2010 The dynamics of the piezo inkjet printhead operation. *Phys. Rep.* **491**, 77–177.
- WILKES, EDWARD D., PHILLIPS, SCOTT D. & BASARAN, OSMAN A. 1999 Computational and experimental analysis of dynamics of drop formation. *Physics of Fluids (1994-present)* **11** (12), 3577–3598.
- YOUNG, T. 1805 An essay on the cohesion of fluids. *Philos. Trans.* **95**, 65–87.

# Laura Augello

## Curriculum Vitae

Av. de Mon-Loisir 16  
1006 Lausanne, Suisse  
✉ laura.augello@gmail.com



### Personal data

Nationality: **Italian**  
Date of birth: **April 6<sup>th</sup> 1985**  
Place of Birth: **Torino, Italy**

### Education

2015 **Ph.D. in mechanical engineering,**  
*EPFL, Lausanne (Switzerland),*  
Thesis: Instability of two-phase co-axial jets at small Reynolds number,  
Supervisor: Prof. F. Gallaire.

March 2010 **Master Degree in Mathematical Engineering,**  
*Politecnico di Torino (Italy),*  
Thesis: Multiobjective optimization of bridge edge barriers: aerodynamic and crash analysis,  
Supervisors: L. Bruno, C. Tribuzi.  
Final marks: 107/110

Feb 2008 - **Erasmus - École Polytechnique Fédéral de Lausanne (EPFL).**  
July 2008

December 2007 **Bachelor Degree in Mathematics for Engineering Sciences,**  
*Politecnico di Torino (Italy),*  
Thesis: Cycle-pedestrian bridge made with Bailey's panels,  
Supervisor: Prof. F. Algostino.  
Final marks: 94/110

June 2004 **High School Diploma,**  
*Liceo Scientifico "E. Majorana" (Italy),*  
attend the projet P.N.I. - National Plane of Informatics.  
Final marks: 100/100

### Language

Italian **Mothertongue**  
English **Good**  
French **Basic**

*IELTS with 5.5*

---

## Work Experience

- September 2010 - April 2011 **Stage**, *Acus s.r.l. - consulting company for Energy engineering.*  
Enterprise Incubator of the Politecnico di Torino, Italy
- April 2009 - February 2010 **Stage**, *Novanalysis - consulting company for advanced engineering,*  
Activities concerning the thesis.  
Rivoli, Torino, Italy
- 2005 - 2009 **Tutor of Mathematics**,  
Individual lessons for secondary school students.

## Voluntary

- 2001-2007 **Tourist guide at the Royal Palace**, *Committed regularly as a voluntary guide in the Museums of Royal Palace*, project Ambasciatorino - Ragazzi del 2006, introduced by City of Turin.
- February 2006 **Tourist guide at the Royal Palace**, *Torino, Italy*, Torino 2006, Winter Olympic Games and Winter Paralympic Games.

---

## Teaching

- 2013-2015 **Teaching assistant at EPFL**, *in Hydrodynamics.*
- 2011-2014 **Teaching assistant at EPFL**, *in Numerical Flow Simulation.*